STUDY OF CRYSTAL STRUCTURE AND MAGNETIC PROPERTIES OF DOUBLE PEROVSKITE OXIDES

By

ROHAN PHATAK

Enrolment No. PHYS01201104003

Bhabha Atomic Research Centre, Mumbai, India.

A thesis submitted to the

Board of Studies in Physical Sciences

In partial fulfillment of requirements

for the Degree of

DOCTOR OF PHILOSOPHY

of

HOMI BHABHA NATIONAL INSTITUTE

June, 2017

Homi Bhabha National Institute

Recommendations of the Viva Voce Committee

As members of the Viva Voce committee, we certify that we have read the dissertation prepared by **Mr. ROHAN PHATAK** entitled **"STUDY OF CRYSTAL STRUCTURE AND MAGNETIC PROPERTIES OF DOUBLE PEROVSKITE OXIDES"** and recommend that it may be accepted as fulfilling the thesis requirement for award of Degree of Doctor of Philosophy.

Chairman – Prof. S. Kannan Date: 23/02/2018

Guide / Convener – Prof. Amitabh Das Date: 23/02/2018

Co-Guide – Prof. S. K. Sali Date: 23/02/2018

Examiner – Prof. P. N. Santhosh Date: 23/02/2018

Member – Prof. Ravi Kumar G. Date: 23/02/2018

Member – Prof. A. K. Nigam Date: 23/02/2018

AKNigam

Final approval and acceptance of this thesis is contingent upon the candidate's submission of the final copies of the thesis to HBNI.

I hereby certify that I have read this thesis prepared under my direction and recommend that it may be accepted as fulfilling the thesis requirement.

Date: February 23, 2018
Place: Mumbai

Prof. Amitabh Das

STATEMENT BY AUTHOR

This dissertation has been submitted in partial fulfillment of requirements for an advanced degree at Homi Bhabha National Institute (HBNI) and is deposited in the Library to be made available to borrowers under rules of the HBNI.

Brief quotations from this dissertation are allowable without special permission, provided that accurate acknowledgement of source is made. Requests for permission for extended quotation from or reproduction of this manuscript in whole or in part may be granted by the Competent Authority of HBNI when in his or her judgment the proposed use of the material is in the interests of scholarship. In all other instances, however, permission must be obtained from the author.

Phatak

(Rohan Phatak)

DECLARATION

I, hereby declare that the investigation presented in the thesis has been carried out by me. The work is original and has not been submitted earlier as a whole or in part for a degree / diploma at this or any other Institution / University.

Phatak

(Rohan Phatak)

List of Publications arising from the thesis

Journal

1. “Structure and magnetic properties of Sr_2CoRuO_6”, R. Phatak, K. Krishnan, S.K. Sali, A. Das, A.K. Nigam, *Journal of Magnetism and Magnetic Materials*, **2013**, *344*, 129-133.

2. “Crystallographic site swapping of La^{3+} ion in $BaA'LaTeO_6$ (A' = Na, K, Rb) double perovskite type compounds: diffraction and photoluminescence evidence for the site swapping”, R. Phatak, S.K. Gupta, K. Krishnan, S.K. Sali, S.V. Godbole, A. Das, *Dalton Transactions*, **2014**, *43*, 3306-3312.

3. “Crystal structure of $Ba_2(La_{0.727}Ba_{0.182}M_{0.091})MO_6$ (M = Nb, Sb, Bi): symmetry nuance identified in photoluminescence and IR spectroscopy studies”, R. Phatak, S.K. Gupta, P. Maheshwari, A. Das, S.K. Sali, *Dalton Transactions*, **2017**, *46*, 1694-1703.

4. “Pentavalent uranium complex oxides: A case study on double perovskites $Ba_2REU^{5+}O_6$ (RE = La, Nd, Sm)”, Rohan Phatak, A.K. Yadav, Nimai Pathak, C.L. Prajapat, U.M. Kasar, M.R. Singh, S.N. Jha, Dibyendu Bhattacharyya, Amitabh Das, S.K. Sali, *Journal of Alloys and Compounds*, **2017**, *708*, 1168-1177.

Conferences & Symposiums

1. Crystallographic site swapping of Eu^{3+} ion in $BaLaMTeO_6$ (M=Na, Rb) perovskite and its effect on Photoluminescence, R. Phatak, S.K.Gupta, S.K.Sali, K. Krishnan, V.Natarajan, S.V.Godbole, A.Das, Proceedings of the DAE-BRNS Fourth Interdisciplinary Symposium on Materials Chemistry (ISMC-2012), Mumbai, held during 11-15 Dec 2012, p. 224.

2. Relaxor behavior in Spin Glass Perovskite Sr_2CoRuO_6, R. Phatak, S.K. Mishra, S.K. Sali, A. Das, DAE-BRNS Fifth Interdisciplinary Symposium on Materials Chemistry (ISMC 2014), Mumbai, held during 9-13 Dec 2014, p. 373.

3. Structural studies of novel perovskites : $BaLa_{2/3}U^{5+}O_{5.5}$ using EXAFS, XANES, SEM-EDX and XRD techniques, R. Phatak, A. Yadav, N. Pathak, R. Gupta, S. N. Jha, D. Bhattacharyya, A. Das, S. K. Sali, European Conference on X-Ray Spectrometry (EXRS2016), Gothenburg, Sweden, held during 19-24 June 2016, Poster No. 150, p. 254.

(Rohan Phatak)

DEDICATED

TO

My Late Grandfather

Shri. Narhar G. Phatak

ACKNOWLEDGEMENTS

I would like to take this opportunity to acknowledge all those who have directly or indirectly provided support, encouragement, and guidance thus far during the period of my Ph.D. Firstly, I would like to especially thank my Guide, Dr. Amitabh Das and co-guide Dr. S. K. Sali for their continuous support, guidance, and constructive criticism. Both have given their valuable time for scientific discussion, critically checking the data analysis, manuscripts and thesis. Dr. Amitabh Das introduced me to the perovskite materials and related topics on which I further carried out my research work. Being from the physics background and having less knowledge about the chemical synthesis, Dr. Sali has always shared his expertise experience related to chemical synthesis, troubleshoot and fine-tune the synthesis procedures.

I would like to thank our current Head of the Division, Fuel Chemistry Division, BARC, Dr. S. Kannan for his support and understanding during the course of my Ph.D. Similar thanks goes to our former Head of the Division, Dr. S. K. Aggarwal. I would like to acknowledge Dr. S. Kannan for introducing Rietveld refinement, which was a major part of the data analysis. Being chairman of my Ph.D. review committee, he kept a constant check on the progress of my work. I also thank Dr. G. Ravi Kumar and Prof. A. K. Nigam whose useful suggestions as doctoral committee members have been very helpful. Thanks to my present and retired section members (Dr. N. D. Dahale, Dr. N. K. Kulkarni, Dr. K. Krishnan, Dr. Meera Keskar, Mr. Bal Govind Vats, Mrs. Geeta Shelke and Mr. Shafeeq Mohammad) for their countless help in laboratory work and experiments. I wish to thank Dr. S. N. Achary who was always there to guide me in tricky crystal structure analysis situations. Many thanks to all my collaborators and co-authors for all their support to carry out planned work in this thesis. I also thank my office colleagues and FCD office staff for their help. I thank my friends Krishna Kumar, Rajib Kar, Manish Chopra, Saurav Guin, Neetika Sharma, Pulkit, and many others for their help, advices and encouragements.

Very special thanks to my loving wife Manasi. I acknowledge her for giving up all those holidays and weekends when I was busy writing my thesis. I thank my parents, in-laws, and relatives for their constant encouragement.

Surely I may have missed out few people and would like to thank them for helping me to complete my Ph.D.

Contents

Homi Bhabha National Institute

SYNOPSIS OF Ph. D. THESIS

1. **Name of the Student:** Rohan Anil Phatak
2. **Name of the Constituent Institution:** Bhabha Atomic Research Centre
3. **Enrolment No. :** PHYS01201104003
4. **Title of the Thesis:** Study of Crystal Structure and Magnetic Properties of Double Perovskite Oxides
5. **Board of Studies:** Physical Sciences

SYNOPSIS

Perovskites are the most widely studied compounds in inorganic materials because of their rich diversity in physico-chemical properties and crystal structures. Materials with perovskite type structure exhibit varied functional properties like ferromagnetism, ferroelectricity, multiferroics, piezoelectric, superconductivity, semiconductor, magneto-resistance, half-metals, ionic conductivity, photo-catalysis, photoluminescence etc and hence used for variety of applications in material science.

Double Perovskites (DP) derived from single perovskites (ABX_3) have general formula $A_2BB'X_6$ or $AA'BB'X_6$, where different type of chemical ordering exists between B-cations or in few cases between A-cations [1]. The most common type of ordering observed in DP is the rock salt ordering between B and B' cations. A change in the crystal structure is found to have pronounced effect on symmetry, bond overlap, band energy and its electronic structure. DP class of compounds provides ample opportunity to study their crystal structure and its correlation with physical properties [2]. Following are the factors in DP, that can be tuned to alter their crystal structure and subsequently their physical properties. Firstly, the most important feature in DP is the degree of chemical ordering between B and B’ cations. Anderson et al. have shown that charge and size differences between B and B’ cations are important factors for deciding the degree of ordering in double perovskites [3]. The degree of B-cation ordering is shown to have a large effect on its physical properties like electrical conductivity and magnetism. With only one magnetic B-cation and rock-salt ordering, it forms a Face-centered cubic (Fcc) type network of magnetic cations. This Fcc type network forms the simplest 3D network which can create geometrical magnetic frustration within the system. Thus a slight change in the degree of B-cation ordering and/or lowering of crystal symmetry can cause huge difference in the nearest-neighbor (nn) and next-nearest-neighbor (nnn) interactions, resulting in either long range magnetic ordering or frustrated system. When both the B-cations are magnetic; in addition to the above nn and nnn interactions, super-exchange or direct-exchange plays a vital role in deciding the magnetic and conductivity properties. Secondly, the chemical substitution at A-site can also change the structure and physical properties. Without disturbing the combination of B-cations, different dopants can be substituted at A-site, either to vary the chemical pressure which indirectly influence the pressure on B-cation octahedra (influencing the overlap of the orbitals between B-cation and X-anion and thus altering the electronic structure) and/or cause tilting of the B-cation octahedral (influencing the super-exchange interaction between B-cations) and/or to change the oxidation states in B-cation. Chemical doping influences A-cation size variance which also indirectly influences the physical properties.

The work described in this thesis emphasizes on the structural studies and related physical properties of few variants in oxide based double perovskites. Four different systems were studied in this thesis work. In the first system, we study the influence of B-cation ordering with 3d-4d couple (Co-Ru system) on its magnetism and show how the random ordering imparts dominance of spin glass behavior in $Sr_2Co_{2-x}Ru_xO_6$ system compared to narrow window of ferromagnetism near the end compounds $SrCoO_3$ and $SrRuO_3$. The second system is on the study of $BaLaMM'O_6$ compounds (M=alkali earth metal or alkaline earth metal; M'=Te, Nb, Sb) where the influence of ionic size of M-cation on its crystal structure. Photoluminescence studies of these compounds were performed by doping Eu at La position and it confirms the interchange of crystallographic site of La atom between A or B-site with change in ionic size of M-cation. In the third system, lowering of La content in Ba_2LaMO_6 to form the compounds with stoichiometry $Ba_2La_{2/3}MO_{5.5}$ (M^{5+}=Nb, Sb, Bi, U) and its influence on octahedral distortion was investigated. The photoluminescence properties in Eu doped compounds and IR spectroscopy were used to probe the octahedral distortion in these compounds. In the last system, the double perovskites with pentavalent uranium Ba_2REUO_6 (RE=La, Nd, Sm) compounds were studied for crystal structure and magnetic properties. The B-cation ordering causes absence of U-U interaction leading to paramagnetism with novel EPR observations.

In all the above work, powder X-ray (XRD) and Neutron diffraction (ND) data were used for studying the bulk crystal structure, while techniques like Extended X-ray Absorption Fine Structure (EXAFS), Photoluminescence (PL) and Fourier Transform Infrared Spectroscopy (FTIR) were used for probing the local crystal structure around the specific atoms. Other physical properties like magnetization, conductivity, dielectric measurements were also carried out in relevant cases. Due to the diversity in the double perovskite systems studied in this thesis, separate chapters are dedicated for each type of systems. The thesis is divided into six chapters. A brief description of the chapters is as follows:

Chapter 1, gives the general introduction to perovskites and their crystal structures. In a simple perovskite ABX_3 structure, BX_6 octahedra are connected at the corners and the intermediate space is occupied by a larger size A-cation having 12 co-ordination. X can be halogens, nitrogen or oxygen. Ideally, the basic perovskite ABX_3 has cubic symmetry with space group Pm-3m and lattice parameter a ~ 4Å, with the ratio $(r_A - r_X)/\sqrt{2}(r_B - r_X)$ equals to unity, where r is respective ionic radii of A, B, and X atoms with co-ordination number 12, 6 and 6 respectively. When the ionic radii of A and B-cation deviates from the ideal condition, the structure is stabilized by tilting of the BX_6 octahedra (or in few cases movement of A-cation from their equilibrium position) which reduces the symmetry leading to non-cubic structure. Tolerance factor for perovskite structure is defined as $\tau = (r_A - r_X)/\sqrt{2}(r_B - r_X)$. It is observed that when τ is close to unity, perovskites has cubic symmetry. As the τ reduces, lower symmetry structures like tetragonal, rhombohedral, orthorhombic or monoclinic are observed, whereas for $\tau > 1$, hexagonal polytypes are observed. When $\tau < 1$, the A-cation is under bonded and this is stabilized by collective tilting of the B-cation octahedra, subsequently reducing the crystal structure symmetry but still holding the corner connectivity among the B-cation octahedra. Crystal structure derived from perovskites with cation or anion vacancies gives an additional freedom for tailoring their properties. With this underlying network, multiple substitutions at A or B-site with a periodic arrangement of cations or in some cases periodic arrangement of defects (cation or anion vacancies) can lead to the formation of complex perovskite related structures. We discuss the factors influencing the crystal structure and physical properties of double perovskites and the motivation for the present work.

Chapter 2 describes the syntheses methods used for the preparation of the compounds and experimental techniques used during the course of the work viz., powder X-ray diffraction, powder neutron diffraction, neutron depolarization study, x-ray absorption spectroscopy, dc and ac magnetization measurements, electron paramagnetic resonance spectroscopy, four probe resistivity measurements, dielectric measurements, thermogravimetry, photoluminescence and Fourier transform infrared spectroscopy.

All compounds were synthesized by the conventional high temperature solid state reaction method. Gel-combustion method was also used in some cases where, chemical homogeneity is important as in doped compounds. Powder X-ray diffraction was used for monitoring the reaction and confirming the formation of the phase. Crystal structure analysis was done using powder x-ray and neutron diffraction data. The neutron diffraction patterns were recorded on the PD2 powder diffractometer ($\lambda = 1.2443Å$) at the Dhruva reactor, Bhabha Atomic Research Centre, Mumbai, India, between 6K and 300K in the angular range $5° \leq 2\theta \leq 140°$. Rietveld method was used for refining the crystal structure using powder diffraction data. FULLPROF program was used for the Rietveld refinement analysis. High temperature x-ray diffraction data was collected in the range 300K to 1273K using STOE diffractometer with Edmund Bühler High-Temperature Chamber HDK 2.4 attachment. X-ray Absorption Near Edge Structure (XANES) and Extended X-Ray Absorption Fine Structure (EXAFS) measurements were carried out on the Energy-Scanning EXAFS beamline (BL-9) at the INDUS-2 Synchrotron Source (2.5 GeV, 200 mA) at Raja Ramanna Centre for Advanced Technology (RRCAT), Indore, India. DC magnetization was measured in ZFC and FC mode using the SQUID magnetometer (Quantum Design) between 5 and 300 K. AC magnetic susceptibility measurement was measured using SQUID-VSM (Quantum Design) between 2 and 300 K in ac field of 1 Oe. To study the magnetic inhomogeneity in samples, neutron depolarization measurements ($\lambda = 1.205Å$) were carried out on the polarized neutron spectrometer at Dhruva reactor, Bhabha Atomic Research Centre, Mumbai, India, with Cu_2MnAl (1 1 1) as polarizer and $Co_{0.92}Fe_{0.08}$ (2 0 0) as analyzer. Electron paramagnetic resonance spectra were recorded using Bruker EMM-1843 spectrometer with an operating X-band frequency 9.4153 GHz, equipped with 100 kHz field modulation. Photoluminescence experiments were carried out on an Edinburgh CD-920 unit equipped with a Xe flash lamp with 10–100 Hz frequency as the excitation source. The data acquisition and analysis were done by F-900 software provided by Edinburgh Analytical Instruments, UK. Infrared spectroscopy was carried out using a Bruker alpha FTIR instrument. Thermogravimetric studies were carried out using Mettler thermoanalyzer (model: TGA/SDTA 851^e/MT5/LF1600). Low temperature conductivity measurement was carried out using four probe method. The low-temperature dielectric measurements were carried out using a frequency-response analyzer (Novocontrol TB-Analyzer).

Chapter 3, gives a brief introduction to perovskites with 3d and 4d transition metals at B-site, containing cobalt and ruthenium, respectively. Cobaltates and ruthenates show a variety of magnetic and transport properties which are attributed due to the multiple oxidation states in cobalt like $Co^{2+/3+/4+}$ along with the low/intermediate/high spin states and $Ru^{3+/4+/5+}$ oxidation states for ruthenium. Thus, study of cobalt and ruthenium perovskites for their magnetic and transport properties has gained lot of interest in recent years. In the present study, the intermediate perovskite phases in Sr–Co–Ru–O system were investigated. Compounds $SrCoO_3$ and $SrRuO_3$ show ferromagnetic and metallic properties, indicating that Co^{4+}–O–Co^{4+} and Ru^{4+}–O–Ru^{4+} super-exchange interactions are ferromagnetic in nature. However, intermediate phases $Sr_2Co_{2-x}Ru_xO_6$ (x=0.5, 1, 1.5) show significantly different structural, magnetic and resistivity properties as compared to the end compounds $SrCoO_3$ and $SrRuO_3$. In $Sr_2Co_{1.5}Ru_{0.5}O_6$, Sr_2CoRuO_6 and $Sr_2Co_{0.5}Ru_{1.5}O_6$ compounds, valence state of cobalt and ruthenium are ($0.5Co^{3+}/1Co^{4+}/0.5Ru^{5+}$), ($Co^{3+}/Ru^{5+}$) and ($0.5Co^{3+}/1Ru^{4+}/0.5Ru^{5+}$) with orthorhombic (Imma), monoclinic (I2/c) and orthorhombic (Pnma) crystal structures, respectively. The intermediate compounds in this series, has random ordering at B-site and show spin glass behavior as compared to long range magnetic ordering observed in the end members. Sr_2CoRuO_6 shows spin glass transition at 95K and it has been established using magnetization, neutron diffraction, AC magnetization and neutron depolarization techniques [4]. The spin glass nature of these compounds is attributed to multiple valences and mixed competing nearest neighbor and next nearest neighbor magnetic interactions between randomly distributed Co and Ru cations. Temperature dependence resistivity of Sr_2CoRuO_6 compound exhibits semi conductor like resistivity and is described using the variable range hopping model. The Sr_2CoRuO_6 compound also shows relaxor type dielectric property with the real part of dielectric constant occurring at around 95K [5]. The spin glass and dielectric relaxor properties occurring at same transition temperature of 95K for the Sr_2CoRuO_6 is novel and has common underlying origin.

In chapter 4, two series of compounds, $BaLaMM'^{6+}O_6$ (M=Na, K, Rb and M'=Te) [6] and $BaLaMM'^{5+}O_6$ (M=Mg, Ca, Ba and M'=Nb, Sb) were studied. All these compounds show cationic ordering at B-site but no sign of A-site ordering was observed. Depending upon the size of alkali metal and alkaline earth metal, these compounds show different crystal structures with position of La atom shifting from A-site to B-site. To study the variation in the symmetry around the La atom, the photoluminescence technique with Eu doped samples were also investigated. The emission spectra of Eu^{3+} doped samples show strong dependence on its local site symmetry in the host material and is used as a spectroscopic probe for detecting the difference in symmetries [7]. The orange luminescence (590–600 nm) of Eu^{3+} due to the magnetic dipole transition (MDT) $^5D_0 \rightarrow {}^7F_1$ is independent of the local site symmetry, while the red luminescence (~610–630 nm) due to the electric dipole transition (EDT) $^5D_0 \rightarrow {}^7F_2$, being hypersensitive, is affected by the site symmetry of Eu^{3+} ion. The intensity ratio of these two lines gives information about the site symmetry. Comparison of local symmetry around La^{3+} cation was studied using Photoluminescence (PL) by doping Eu^{3+} at La site. IR spectroscopy is also used for characterizing these compounds. Octahedral vibrations are found to dominate the IR spectra and leads to broad characteristic absorption peak at around $600cm^{-1}$. The centre of this peak has been correlated to electronegativity of B-cations and reduced mass of the B-O bond. The IR data analysis is in concordance with the crystal structure models refined using x-ray diffraction.

Chapter 5, includes the synthesis and crystal structures of the perovskite phases with the formula $Ba_2La_{2/3}M^{5+}O_{5.5}$ (M=U, Nb, Sb, Bi) [8]. All these compounds were prepared by gel combustion or solid state methods. Purity of the phases was monitored by the x-ray diffraction analysis. The x-ray and the neutron diffraction studies were not sufficient to conclude on the crystal structure hence, positron annihilation spectroscopy was used. Positron annihilation lifetime spectroscopy is a sensitive technique for detecting the cation vacancy and was used for investigating of these compounds. In perovskites, it has been shown that the positron life-time increases because of the vacancies at A- or B-site. In these studied compounds, no appreciable change in the positron life-time was observed indicating the absence of any cation vacancies. Hence, the purity of the phase and absence of cation vacancies hints that there is formation of perovskite phase with starting stoichiometry but with the normalized formula as $Ba_{2.182}La_{0.727}M_{1.091}O_6$ i.e. [$Ba_2(La_{0.727}Ba_{0.182}M_{0.091})(M)O_6$] where, La deficiency is filled by 0.18 Ba and 0.09 M cations. This model is found to be consistent with x-ray and neutron diffraction analysis. Additionally, these phases were investigated by photoluminescence and infrared spectroscopy, which revealed that the local structure around deficient La site is more distorted due to occupancy by Ba and M atoms. Thus, these findings are in complete concordance with above crystal structure model.

In Chapter 6, the crystal structure and the magnetic properties of pentavalent uranium double perovskites are described. Uranium is the preferred choice for studying 5f electron system due to the problem of availability and handling high radioactivity in trans-uranium elements. Pentavalent uranium compounds are rare because of low stability of U^{5+} oxidation state. These compounds having $5f^1$ electron configuration are important as they are the simplest possible system because of the absence of spin-spin interaction. Optimized synthesis method with reducing atmosphere (Ar v/v92% /H_2 v/v8% gas) was used for synthesis of these phases. Compounds of the series Ba_2REUO_6 (RE=La, Nd, Sm) were synthesized using solid state method and their crystal structure was characterized using powder x-ray and neutron diffraction analysis [9]. Local structure around the uranium atom was characterized using EXAFS measurement on U-L_{III} edge. Magnetic properties corresponding to $5f^1$ electron configuration of U^{5+} was studied using DC magnetization and Electron Paramagnetic Resonance (EPR) techniques. All the compounds are paramagnetic down to 5K. The observed magnetic moment of 0.4 μ_B per U^{5+} ion is very small compared to the theoretical value, but is comparable to the previously reported values. This low moment is attributed to the crystal field effect and the covalent nature in U-O bond. For complex uranium oxides, Y. Hinatsu et al. empirically showed that long range magnetic ordering does not occur if U-U distance is more than the critical distance of 4.6Å [10]. In Ba_2REUO_6 compounds, due to rock salt ordering the U-U distance is greater than 6Å and thus leading to absence of long range magnetic ordering in these compounds. EPR signal with $g>2$ was observed in these samples and the split in the signal was correlated to octahedral distortion around uranium ion in respective compounds.

Chapter 7 describes the summary and conclusions of the present studies.

References:

[1] Cation ordering in perovskites, G. King, P.M. Woodward, Journal of Materials Chemistry **20** (2010) 5785-5796.

[2] $A_2B'B''O_6$ perovskites: A review, S. Vasala, M. Karppinen, Progress in Solid State Chemistry **43** (2015) 1-36.

[3] B-cation arrangements in double perovskites, M.T. Anderson, K.B. Greenwood, G.A. Taylor, K.R. Poeppelmeier, Progress in Solid State Chemistry **22** (1993) 197-233.

[4] Structure and magnetic properties of Sr_2CoRuO_6, **R. Phatak**, K. Krishnan, S.K. Sali, A. Das, A.K. Nigam, Journal of Magnetism and Magnetic Materials **344** (2013) 129-133.

[5] Relaxor behavior in Spin Glass Perovskite Sr_2CoRuO_6, **R. Phatak**, S.K. Mishra, S.K. Sali, A. Das, Fifth Interdisciplinary Symposium on Materials Chemistry (ISMC-2014), Mumbai, 2014, 373.

[6] Crystallographic site swapping of La^{3+} ion in $BaA'LaTeO_6$ (A' = Na, K, Rb) double perovskite type compounds: diffraction and photoluminescence evidence for the site swapping, **R. Phatak**, S.K. Gupta, K. Krishnan, S.K. Sali, S.V. Godbole, A. Das, Dalton Transactions **43** (2014) 3306-3312.

[7] Interpretation of europium(III) spectra, K. Binnemans, Coordination Chemistry Reviews **295** (2015) 1-45.

[8] Crystal structure of $Ba_2(La_{0.727}Ba_{0.182}M_{0.091})MO_6$ (M = Nb, Sb, Bi): symmetry nuance identified in photoluminescence and IR spectroscopy studies, **R. Phatak**, S.K. Gupta, P. Maheshwari, A. Das, S.K. Sali, Dalton Transactions **46** (2017) 1694-1703.

[9] Pentavalent uranium complex oxides: a case study on double perovskites $Ba_2REU^{5+}O_6$ (RE=La, Nd, Sm), **R. Phatak**, A.K. Yadav, N. Pathak, C.L. Prajapat, U.M. Kasar, M.R. Singh, S.N. Jha, D. Bhattacharyya, A. Das, S.K. Sali, Journal of Alloys and Compounds **708** (2017) 1168-1177.

[10] Magnetic studies on alkali metal uranates(V) MUO_3 with the perovskite structure, Y. Hinatsu, Journal of Alloys and Compounds **203** (1994) 251-257.

List of figures

List of Tables

Chapter 1.

General Introduction

1.1 Introduction

The word ‘perovskite’ comes from the mineral $CaTiO_3$. This mineral was discovered in the Ural Mountains of Russia by Gustav Rose in 1839 and named after Russian mineralogist Lev Perovski [1, 2]. In general, the family of compounds which has a crystal structure framework similar to this mineral are called perovskite. They are the earth's most abundant minerals and are even found in meteorites. These materials have long been of interest to geologists for the clues they hold to the planet's history. In history and till date, perovskite class of compounds has been the most widely studied material and this fact is clearly evident in many of the inorganic compounds databases like Inorganic Crystal Structure Database (ICSD), Cambridge Crystallographic Data Centre (CCDC) and Pearson’s crystal data (PCD) where perovskite class have maximum number of entries. The popularity gained by perovskite compounds rest on its great diversity in crystal structure and chemical composition. It thus provides ample opportunity to the researchers to tailor make the material having required functional properties and indeed it shows a wide range of properties viz. ferromagnetism, ferroelectricity, half-metal, colossal magneto-resistance, superconductivity, piezoelectricity, ionic conductivity, catalyst etc. A large number of books and review articles have been published which describe the varied crystal structure, physical properties and applications of perovskite compounds [3-15].

1.2 Crystal structure

The general formula for perovskite is ABX_3 (where in general, A= Di or trivalent cation, B= 3d, 4d, 5d metal ion, X= O, F etc.). The smaller ionic size cation B is co-ordinated to six X anion forming octahedra. Such BX_6 octahedra are connected to each other by corner sharing X anions. The space formed between such corner shared octahedra is occupied by larger ionic size A cation and it is co-ordinated to twelve X anions. The primitive perovskite has cubic symmetry with representative space group $Pm\bar{3}m$ and is shown in the Fig. 1.1. $SrTiO_3$ and $RbCaF_3$ are the typical examples of such basic cubic perovskite. Using simple geometrical arguments it can be shown that in the ideal cubic perovskite, the ratio $\frac{<A-X>}{\sqrt{2}<B-X>}$ is equal to unity. This shows that in order to have basic cubic perovskite structure the bond lengths <A-X> and <B-X> should satisfy the above ratio to be unity. Clearly, not all combination of A and B with particular X satisfy this unity ratio and the deviation from unity gives rise to lower symmetry perovskite structures. Much of the early work on synthetic perovskites was done by V. M. Goldschmidt, who is well known for the ratio called tolerance factor $t = \frac{(r_A+r_X)}{\sqrt{2}(r_B+r_X)}$ (where r_i are the ionic radii respectively) and its correlation with the symmetry of the perovskites [16]. Tolerance factor acts as a thumb rule to predict the crystal symmetry of perovskites. If the tolerance factor is close to unity then as specified earlier the crystal adopts cubic structure and as it lowers from unity the symmetry reduces to tetragonal or rhombohedral to orthorhombic to monoclinic. It is observed that perovskite structure is stabilized in the range $0.75< t <1$ [13]. If the tolerance factor is greater than unity then crystal adopts hexagonal symmetry.

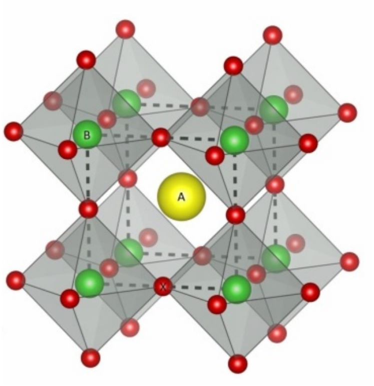

Figure 1.1 *Crystal structure of primitive cubic perovskite* ABX_3

1.2.1 Factors affecting the crystal structure

Along with the ionic size of the cations as mentioned above additional factors like nature of bonding, electronic structure, pressure, temperature and vacancy (defects) can cause deviation from the ideal cubic structure. The deviation from cubic structure occurs due to three different mechanisms viz. 1) co-operative tilting of the octahedral; 2) distortion of the octahedra; and 3) displacement of A or B cation from their ideal positions. Of these mechanisms co-operative tilting is the most common.

1) **Co-operative tilting of the octahedra:** If the tolerance factor is less than one which suggests that size of A cation is smaller than the space formed by the BX_6 octahedra and in this case cation A is under-bonded. This is stabilized by tilting of the BX_6 octahedra while maintaining their corner sharing connectivity and reduces the volume of the space occupied by the A cation. When seen along particular direction the tilting of the octahedral can be either in-phase (rotation in same manner) or out-of phase (rotation in opposite manner). Many notations have been developed to cover all such tilt mechanisms viz. Glazer notation and Aleksandrov notation [17, 18]. Most commonly used is the Glazer notation, which was developed by A. M. Glazer. Glazer notation are given by '$a^{\#}b^{\#}c^{\#}$' where alphabets indicates the tilting along that particular axis (same alphabets indicate same magnitude of tilting, for

example ‘abb’ would have equal magnitude of rotation about the b and c axes, but not about the a axis) and superscript # is 0, + or - indicating zero, in-phase or out-of phase tilting, respectively.

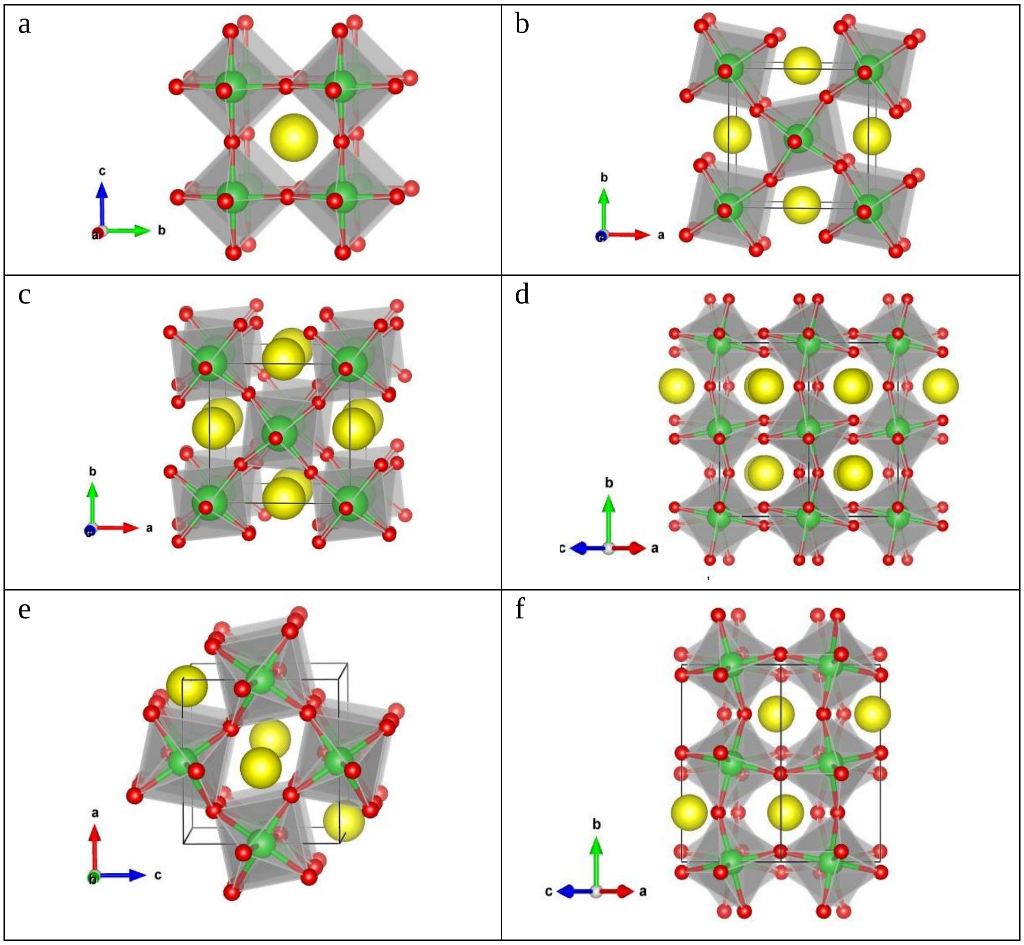

Figure 1.2 *Common types of octahedral tilts: a) for cubic Pm*$\bar{3}$*m space group with no tilt; b) for tetragonal P4/mbm space group with* $a^0a^0c^+$ *(in-phase tilt along c axis); c) for tetragonal I4/mcm space group with* $a^0a^0c^-$*(out-of phase tilt along c axis); d) for orthorhombic Imma space group with* $a^0b^-b^-$ *(out-of phase tilt along b and c axis*); e & f) for monoclinic space group with* $a^-b^+a^-$ *space group (out-of phase tilt along a and c axis and in-phase tilt along b axis*). [* The lattice vectors corresponds to (011), (200) and (01-1) in terms of the lattice vectors of cubic Pm*$\bar{3}$*m].*

Consider example with Glazer notation $a^0a^0c^-$, here 0 indicates no tilting and out-of phase tilt along c axis. The ideal cubic without any distortion has Glazer notation $a^0a^0a^0$. Fig. 1.2 shows few common octahedral tilts.

Later Howard & Stokes reviewed Glazer's work using group-theoretical analysis and showed 15 distinct tilt systems for the single perovskite ABX_3 [19] and 12 distinct tilt systems for double perovskite $A_2BB'X_6$ [20]. The tilt systems vary with very slight differences and identifying the tilt system adopted by the compound is a nontrivial exercise. The h, k and l values from set of reflections in powder X-ray and neutron diffraction data can be used to identify the tilt system adopted by the compounds. If the peaks in the diffraction pattern are indexed using a double-edge primitive cubic cell (for oxides, a~8 Å), the Miller indices can be categorised into four types: (i) fundamental perovskite reflections where h, k and l are all even numbers. (ii) R-point reflections where h, k and l are all odd numbers. These reflections can arise from either octahedral-site cation ordering or out-of-phase octahedral tilting. (iii) M-point reflections where two of the Miller indices are odd numbers and one is an even number. These reflections are an unambiguous sign of in-phase octahedral tilting. (iv) X-point reflections where two of the Miller indices are even numbers and one is an odd number. These reflections arise from coupling of the R-type modes corresponding to out-of-phase octahedral tilting and M-type modes corresponding to in-phase octahedral tilting.

2) **Distortion of the octahedra:** This mechanism is solely due to electronic structure of cations like Jahn-Teller (JT) effect (distortion). JT effect is commonly seen in cations with unsymmetrical distribution of d-electrons with octahedral geometry like high-spin Mn^{3+} $3d^4$ ($t^3_{2g}e^1_g$), Cu^{2+} $3d^9$ ($t^6_{2g}e^3_g$), low spin Ni^{3+} $3d^7$ ($t^6_{2g}e^1_g$), intermediate spin Co^{3+} $3d^6$ ($t^5_{2g}e^1_g$) [21]. For JT active ion in octaherda causes elongation of octahedral along c axis. In perovskites there are two types 1) d-type where there is in-phase tilting along elongated axis

and 2) a-type with out-of phase tilting along elongated axis. Generally this type of distortion can be quantified using octahedral distortion parameter given as $\Delta d=1/6\sum(d_i-d_{avg})^2/(d_{avg})^2$, where di is the bond distance between B and X atom and d_{avg} is average bond distance [22] and by quadratic elongation parameter given as $\lambda= 1/6\sum(d_i/d_0)^2$, where d_0 is the centre-to-vertex distance of a regular polyhedron of the same volume [23].

3) **Displacement of A or B cation from their ideal positions:** Third mechanism is where there is displacement of the A or B cation from their centroid position. Such mechanism can be caused by many reasons. Common examples are found in compounds having Pb^{2+}, Sn^{2+} or Bi^{3+} where lone pairs from ns^2 orbital causes displacement of cation from its centroid position. Many perovskites with these cations are explored for their ferroelectric and multiferroic properties. $BaTiO_3$, $SrTiO_3$ and many other variants in them has been vastly studied for their ferroelectric properties. It took many decades to understand true nature of the ferroelectric property in $BaTiO_3$. The mechanism was explained by displacive instability due to soft phonon mode concept and order- disorder transition [24-26]. Additionally this third kind of deviation from ideal cubic perovskite is also seen in some cases of tilting systems, where tilting indirectly causes A site cation to displace from its centroid or in other cases where A-site cation ordering takes place.

1.2.2 Cation ordering in perovskites

In complex higher order perovskites ordering of the cations is usually observed. Here there are particular patterns in which the cations are periodically arranged to form unit cell which is in multiples of primitive perovskite cell. Cation ordering can occur at A and/or B site (see Fig. 1.3) but most of the interesting properties arise from B site cations having 3d, 4d, 5d elements and thus B site ordering is the most widely studied.

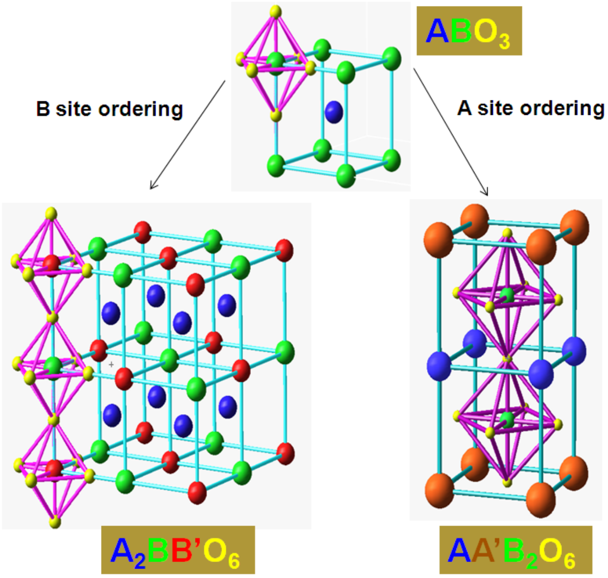

Figure 1.3 *B-site and A-site ordering in perovskites.*

B-site cation ordering in $A_2BB'O_6$ perovskites are of three types viz. rock salt type, columnar type or layer type of which rock salt type ordering is the most commonly observed. These three types of ordering are shown in the Fig. 1.4. Review articles by Anderson et.al. and Graham King et.al. covers these type of ordering in depth with examples [27, 28]. As a general thumb rule when oxidation states of cations at B-site differ by less than two mostly there is no ordering and we get random arrangement at B-site, whereas if the difference is greater than two almost always produces ordered cation arrangement. The other factor is the ionic size difference between the B-cations and it becomes the important guiding factor when the charge difference is exactly two. The greater the difference in the ionic size, the easier the B-cation orders. Additionally, depending on synthesis conditions like sintering temperature and quenching method, there is always some amount of anti-site disorder causing intermediate ordering. The level of order can be quantified by the order parameter $\eta = 2\theta\text{-}1$, where θ being the occupancy of the dominant atom in the site being considered, thus $\eta = 0$ describes complete disorder and $\eta = 1$ describes complete ordering.

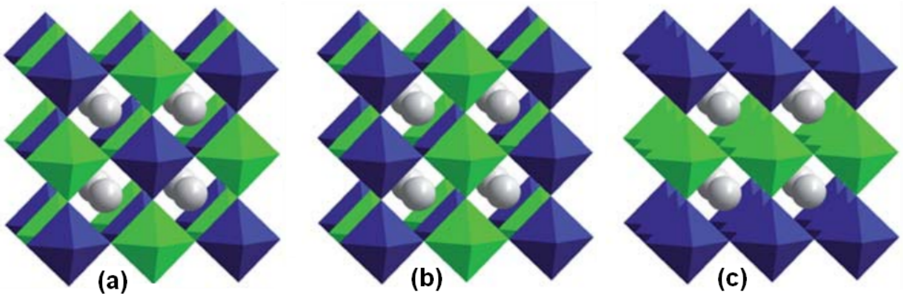

Figure 1.4 *B-site ordered perovskites showing (a) rock salt ordering (b) columnar ordering and (c) layered ordering of B and B' cation octahedra [28].*

1.2.3 Double perovskite

As discussed above ordering can be at A or B site, but most common of all ordering, type $A_2BB'O_6$ with rock salt type ordering is the most common and widely studied. Here unless until specifically mentioned, double perovskite (DP) means $A_2BB'O_6$ type compound with rock-salt type ordering between B-cations. The unit cell of the ideal cubic DP is doubled in size ($2a_p$ x $2a_p$ x $2a_p$, where a_p is the lattice parameter for primitive cubic perovskite) due to the B-cation ordering and its lattice parameters are approximately equal to ~8Å with resulting space group $Fm\bar{3}m$. As the tolerance factor decreases, lower symmetry crystal structures are preferred due to the tilting of octahedra as discussed before. Twelve distinct tilt systems are identified for DP [20] and the resulting space groups are given in the chart shown in the Fig. 1.5. For lower symmetry DP, primitive unit cell are indexed using different set of cell parameters with lattice parameters $\sqrt{2}a_p$ x $\sqrt{2}a_p$ x $2a_p$. With single A cation the most commonly observed space groups are $a^0a^0a^0$ ($Fm\bar{3}m$), $a^-a^-a^-$ ($R\bar{3}$), $a^0a^0c^-$ ($I4/m$), $a^0b^-b^-$ ($I2/m$) and $a^+b^-b^-$ ($P2_1/n$).

Apart from the fundamental interest in ordering phenomenon of B-cations in DP, it also affects many physical properties [29]. The very important feature in DP is 180° B-O-B' interaction and this can be exploited to study various interactions viz. electronic, magnetic between different d-metal cations. In general to achieve B-cation ordering in $A_2BB'O_6$, ionic charge difference $\Delta q_B \geq 2$ and ionic size difference $\Delta r_B \geq 0.17$Å must be satisfied. This can be realized with combination of B-cations as, B=3d and B'=4d/5d/4f/5f elements. Often intriguing electric and magnetic properties emerge in this scenario. For instance, the most famous and extensively studied example is half-metallic and magnetoresistance properties of Sr_2FeMoO_6. These properties are strongly affected by the degree of ordering between Fe and Mo cations [15, 30]. Similarly, the strength of several magnetic interactions like 180° nearest-neighbor (NN) B-O-B', 90° NN B/B'-O-O-B/B' and 180° B-O-B'-O-B next-nearest-neighbor (NNN) interactions are important for deciding the magnetic ordering in the ground state. Anti-site disordering at B-site and distortion of octahedral can have very strong effect on magnetic ground state [29].

In $A_2BB'O_6$ compound disorder in the DP can be of two ways- 1) anti-site disorder, where B and B' cations exchange their positions, 2) anti-phase boundary, where two ordered domains are separated by reverse B-ordering. Fig. 1.6 shows these disordering defects. At microscopic dimension the order/disorder phenomenon can be very complex and as mentioned above has profound effect on physical properties. These disorder types were classified by Woodward into five types: 1) disordered (possibly with or without short-range order), 2) weakly ordered, 3) partially ordered, 4) highly ordered with anti-phase boundary, 5) highly ordered without anti-phase boundary [31].

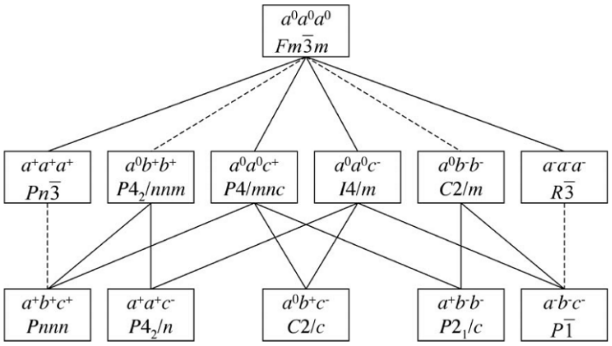

Figure 1.5 *Twelve different tilt systems for double perovskite with rock-salt B-cation ordering.*

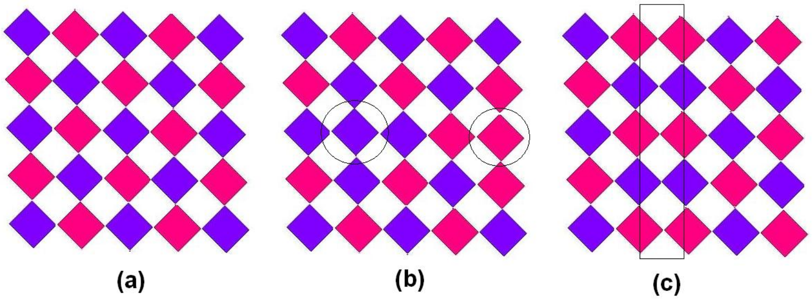

Figure 1.6 *B-cation disorder types in $A_2BB'O_6$, a) complete ordering, b) anti-site disorder, c) anti-phase disorder.*

C. Meneghini et.al. has studied Sr_2FeMoO_6 compound, where EXAFS and XRD results have been carefully analysed and shown to have fourth kind of disorder i.e. highly ordered with anti-phase boundary [30]. The XRD analysis show gradual decrease in intensity and increase in FWHM of the super-lattice reflection arising due to the Fe and Mo ordering as the samples were made disordered. But EXAFS results show very similar features despite the large differences in the long range order. These two observations indicate that a high degree of local order is present along with the anti-phase boundary Anti-phase boundary increases with increasing disorder in samples. The above result clearly explains variation of magnetic measurements done on Sr_2FeMoO_6 compound with varying amount of disorder.

1.3 Magnetic interactions

Pure dipole-dipole interaction between the magnetic moments of the ions is too weak to exhibit a long range magnetic ordering observed in the materials. There are different types of exchange interaction which play an important role in magnetic ordering of these materials. Considering the oxide materials super exchange and double exchange are important and are discussed below:

1.3.1 Super-exchange (SE) interaction

The mechanism of SE was first introduced by Kramers in 1934 [32]. As the name suggests it in not the direct interaction between the magnetic ions but are mediated through connecting non-magnetic ligand. SE interaction takes place by virtual exchange of electrons between orbitals of magnetic ions and the 2p orbital of the O^{-2} ion (considering only the oxide materials). SE can be either AF or FM depending on the interacting orbitals of two magnetic ions taking part in the interaction. This model was further developed by Anderson and in the same year Goodenough [33] and Kanamori [34] proposed some rules which described the main features of the super-exchange interactions. These rules are called Goodenough-Kanamori-Anderson (GKA) rules [35] and are stated below:

1) If there is an overlap and hopping between active (half-filled) orbitals at two centres via 180◦ B-O-B' bond, the exchange is anti-ferromagnetic and strong.
2) If the occupied orbitals are orthogonal, and the electrons can only hop from occupied to empty orbitals via 180◦ B-O-B' bond, the exchange is ferromagnetic and weak.
3) There are situations, occurring especially in the case of 90◦ B-O-B' bond, in which the occupied orbitals overlap with different, orthogonal p-orbitals of a ligand. In this case the exchange is also weak ferromagnetic.

These are the general rules and one has to consider the detailed lattice geometry, specific electronic configuration and orbital occupation, relative importance of different interactions, there may be many different situations, therefore exact classification is difficult. Fig. 1.7 shows the few examples of the SE interaction. SE interactions between various other different B-O-B' bonds are tabulated in reference [36].

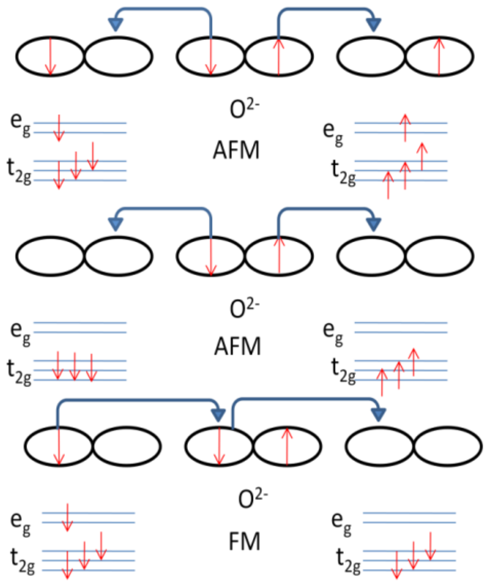

Figure 1.7 *Typical examples of super-exchange interaction in 180◦ B-O-B' bonds.*

1.3.2 Double-exchange (DE) interaction

The DE mechanism was first introduced by Zener [37]. This mechanism was further reformulated in detail and is described in two classic papers by Anderson and Hasegawa [38] and by de Gennes [39]. The DE interaction was first used to explain the concomitant presence of ferromagnetism and metallic conduction in doped manganites $La_{1-x}Ca_xMnO_3$ [40]. In this mechanism, both ferromagnetism and conduction are linked to the mobility of the manganese conduction electrons. The interaction between pairs of Mn^{3+} and Mn^{4+} ions in mixed-valent perovskites through an oxygen atom where the concurrent transfer of an electron from Mn^{3+} (3d e_g) orbital to an O (2p) orbital and then to Mn^{4+} (3d e_g) orbital on an adjacent ion takes place. According to Hund's rule ferromagnetic alignment is energetically favourable. An important aspect is that double exchange is spin polarized conduction and occurs only when the spins of the adjacent Mn ions are aligned parallel or are ferromagnetically ordered. Fig. 1.8 shows represents this double exchange in mixed valence manganites.

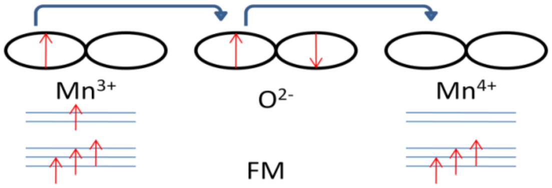

Figure 1.8 *Illustration of double-exchange mechanism for Mn ions with different valence states.*

1.3.3 Magnetic interactions in perovskites

In perovskite structure due to corner sharing octahedral, 180° and 90° magnetic interactions can be studied. The most dramatic magnetic and electronic properties are achieved with two different B and B'-cations. Here depending on the electronic configuration of magnetic B-site cations, 180° B-O-B′ super-exchange pathway is dominant in deciding the magnetic ordering of the compounds [35, 36]. On the other hand when one of the B-cation is non-magnetic, the magnetic ordering of B cations occurs at low temperatures through long super-exchange pathways of 90° and 180° B-O-B′-O-B, or a bending pathway B-O-O-B. In general for d-block cations, this magnetic interaction is much weaker than that in ordered perovskites with magnetic B and B′ cations. Additionally, a complex magnetism can be studied like geometrical frustrated magnetic systems having only one magnetic B-cation or competing magnetic systems with disordered double perovskite compounds. In ordered rock-salt ordered perovskite, B-cations are arranged in FCC type lattice and such arrangement of magnetic ions in FCC lattice are known to have geometric frustration among anti-ferromagnetically coupled species. These double perovskite show high frustration factor $f=|\theta|/T_N$ [41, 42]. Whereas in the case of disordered double perovskite compounds, random distribution of B and B'cations give rise to random distribution of magnetic interactions, which again cause the system to show spin glass type magnetism [43, 44]. The ordered perovskites containing the B-cation as f-block and B’-cation as d-block magnetic ions, then magnetic interaction between d and f electrons may be important. Considering the order of the strength for the magnetic interactions, d-d > d-f > f-f, the magnetic interaction between d-d electrons via long super-exchange pathways, B-O-B’-O-B and B-O-O-B, also may contribute to the magnetic properties. Thus such compounds show more complex and interesting magnetic properties by these two kinds of magnetic interactions.

1.4 Scope of the work

The work carried out in this thesis emphasizes on the structural studies and related physical properties of few variants in oxide based double perovskites. Four different classes of perovskite systems are studied in this work, with the view to study the role of size and disorder on the structure and physical properties in these compounds.

Compounds $SrCoO_3$ and $SrRuO_3$ have been well studied and shown to have ferromagnetic and metallic properties [45, 46]. Surprisingly in the literature, it has been observed that the intermediate compounds in the series $Sr_2Co_{2-x}Ru_xO_6$ does not show long range ordering with spin glass type behaviour in magnetic susceptibility [47, 48]. In the series $Sr_2Co_{2-x}Ru_xO_6$, 3d-4d interactions are involved which changes the physical properties. With the known fact that the end members of the series i.e. $SrCoO_3$ and $SrRuO_3$ compounds being ferromagnetic in nature, the true nature of the magnetism in intermediate compounds is not clear and has not been characterized thoroughly. Therefore in this study, three intermediate compounds in the series $Sr_2Co_{2-x}Ru_xO_6$ (x=0.5, 1, 1.5) are investigated. Along with the dc magnetic susceptibility measurements, neutron diffraction studies have been used to investigate the magnetic ordering in these intermediate compounds. Additionally detailed investigation has been done on Sr_2CoRuO_6 compound using various techniques like ac magnetic susceptibility, neutron depolarization and time dependent magnetizations studies. We observe all the intermediate compounds in the series exhibit spin glass behaviour ($T_{SG} \approx$

95K), irrespective of the Co/Ru ratio. Thus it is concluded that spin glass nature of these compounds is attributed to multiple valences and mixed competing nearest neighbour and next nearest neighbour magnetic interactions between randomly distributed Co and Ru cations. The Sr_2CoRuO_6 compound also shows relaxor type dielectric property with the real part of dielectric constant occurring at around 95K. The spin glass and dielectric relaxor properties occurring at same transition temperature of 95K for the Sr_2CoRuO_6 is novel and need a further investigation. Due to the disorder in these compounds, local structural probe like EXAFS can be used for analyzing the relation between spin glass and relaxor behaviour.

Many double perovskite compounds $A_2BB'O_6$ has been reported with highly charged B' cation (like Nb, Sb, Te, W, U) where almost always there is complete B-cation ordering [29]. But there was no study which reports $AA'BB'O_6$ compounds where the effect of size of A' cation is reported on the crystal structure. Also crystal structure of the compounds in the above series are either not reported previously or incorrectly reported. Compounds $BaLaBB'O_6$ where B'= 4d (Nb, Sb, Te) and B = alkali metal or alkaline earth metals were investigated. The crystal structure was refined using x-ray and neutron diffraction. The local structure around the La cation was probed using photoluminescence (PL) study and shown to be consistent with the crystal structure resolved using diffraction technique. This study also emphasizes the use of PL as local structural probe. The general conclusion drawn from this study shows that, for smaller alkali metal or alkaline earth metals, La ion prefers A-site with 12-cordination, whereas its position is exchange when larger alkali metal or alkaline earth metals. Along with the modification in the crystal structure, the exchange of the La position also affects the photoluminescence property. This methodology can be used in tuning the color of the photoluminescence material which is of great importance in solid state lighting technology.

The perovskite structure has a peculiar property of being impervious to cation or anoin deficiency leading to wide range of non-stoichiometric compounds. These non-stoichiometric perovskite materials have great technological importance in solid oxide fuel cells, ionic conductors, catalyst etc [13, 49, 50]. In this respect, non-stoichiometric DP compounds are supposed to be promising materials with good ionic-electronic conductivity. The 3d transition elements at B-site can provide good catalytic property while 4d/5d transition elements at B'-site can give better electrical conductivity. In the third system, the perovskite phases with the formula $Ba_2La_{2/3}M^{5+}O_{5.5}$ (M=U, Nb, Sb, Bi) has been studied. Here the possibility of simultaneous cation and anion deficiency has been attempted and investigated. Positron annihilation lifetime spectroscopy (PALS) is a sensitive technique for detecting the cation vacancy and was used for investigation of these compounds. PALS analysis shows absence of vacancy. The crystal structure was modeled and refined using x-ray diffraction. From this study it is shown that the compound with formula $Ba_2La_{2/3}M^{5+}O_{5.5}$ does not form non-stoichiometric compounds but have the normalized formula of $Ba_{2.182}La_{0.727}M_{1.091}O_6$ i.e. $[Ba_2(La_{0.727}Ba_{0.182}M_{0.091})(M)O_6]$ where, La deficiency is filled by 0.18 Ba and 0.09 M cations. Distortion caused by the occupancy of Ba and M ion at La position cause octahedral distortion which is probed using photoluminescence and Infrared spectroscopy. It is also shown from therogravimetric and XRD analysis that $Ba_2La_{2/3}UO_6$ perovskite phase does not exists and cannot be prepared from slow oxidation of $Ba_2La_{2/3}UO_{5.5}$.

It is of interest to study pentavalent uranium compounds as they have simplest 5f electron configuration i.e., $[Rn]5f^1$. In addition, uranium is an easy choice because of the problems with availability and high radioactivity in trans-uranium elements. Electronic and magnetic properties of 5f actinide compounds are not well understood as compared to transition metal compounds because of crystal field, spin-orbit coupling and electron-electron repulsion effects are of comparable magnitudes. A single electron in the f shell simplifies the theoretical treatment as electron-electron repulsion is excluded. But at the same time synthesizing pure pentavalent uranium compounds are experimentally challenging and thus there is a paucity of such pentavalent uranium compounds. In this related work, we have studied pentavalent uranium double perovskites, Ba_2REUO_6 (RE= La, Nd, Sm). Though these compounds were reported, a detailed investigation of their crystal structure and confirmation of oxidation state of uranium has been missing. We have investigated the crystal structure using x-ray and neutron diffraction study. Pentavalent oxidation state of uranium was confirmed using XANES, chemical analysis and thermogravimetric methods. The local structure around the uranium was probed using EXAFS measurements on U L_3 edge. The magnetic susceptibility shows weak moment of 0.4 μ_B for U^{5+} ion. In the literature, the electron paramagnetic resonance (EPR) measurement show inconsistency and there is a debate over the origin of signals observed in the EPR spectra. Here for the first time EPR studies on such pentavalent uranium compounds is reported where distance between uranium ions is greater than 6Å. The split in the EPR signal is also correlated to octahedral distortion around uranium.

1.5 References

[1] Perovskite mineral. http://webmineral.com/data/Perovskite.shtml.

[2] A.R. Chakhmouradian, P.M. Woodward, Celebrating 175 years of perovskite research: a tribute to Roger H. Mitchell, Physics and Chemistry of Minerals, **41,** (2014), p. 387.

[3] D.W. Bruce, D. O'Hare, R.I. Walton, Functional Oxides, Wiley (2011).

[4] L.G. Tejuca, J.L.G. Fierro, Properties and Applications of Perovskite-Type Oxides, Taylor & Francis (2000).

[5] R.H. Mitchell, Perovskites: Modern and Ancient, Almaz Press (2002).

[6] F.S. Galasso, Perovskites and High Tc Superconductors, Gordon and Breach Science Publishers (1990).

[7] T. Ishihara, Perovskite Oxide for Solid Oxide Fuel Cells, Springer US (2009).

[8] O.N. Meetei, O. Erten, A. Mukherjee, M. Randeria, N. Trivedi, P. Woodward, Theory of half-metallic double perovskites. I. Double exchange mechanism, Physical Review B, **87,** (2013), p. 165104.

[9] O. Erten, O.N. Meetei, A. Mukherjee, M. Randeria, N. Trivedi, P. Woodward, Theory of half-metallic double perovskites. II. Effective spin Hamiltonian and disorder effects, Physical Review B, **87,** (2013), p. 165105.

[10] D. Serrate, J.M.D. Teresa, M.R. Ibarra, Double perovskites with ferromagnetism above room temperature, Journal of Physics: Condensed Matter, **19,** (2007), p. 023201.

[11] J.B. Goodenough, Electronic and ionic transport properties and other physical aspects of perovskites, Reports on Progress in Physics, **67,** (2004), p. 1915.

[12] D.I. Khomskii, Multiferroics: Different ways to combine magnetism and ferroelectricity, Journal of Magnetism and Magnetic Materials, **306,** (2006), p. 1.

[13] M.A. Peña, J.L.G. Fierro, Chemical Structures and Performance of Perovskite Oxides, Chemical Reviews, **101,** (2001), p. 1981.

[14] A.S. Bhalla, R. Guo, R. Roy, The perovskite structure – a review of its role in ceramic science and technology, Material Research Innovations, **4,** (2000), p. 3.

[15] A.V. Narlikar, Frontiers in Magnetic Materials, Springer, Berlin, **2005**.

[16] V.M. Goldschmidt, Die Gesetze der Krystallochemie, Naturwissenschaften, **14,** p. 477.

[17] A. Glazer, The classification of tilted octahedra in perovskites, Acta Crystallographica Section B, **28,** (1972), p. 3384.

[18] K.S. Aleksandrov, The sequences of structural phase transitions in perovskites, Ferroelectrics, **14,** (1976), p. 801.

[19] C.J. Howard, H.T. Stokes, Group-Theoretical Analysis of Octahedral Tilting in Perovskites, Acta Crystallographica Section B, **54,** (1998), p. 782.

[20] C.J. Howard, B.J. Kennedy, P.M. Woodward, Ordered double perovskites **-** a group-theoretical analysis, Acta Crystallographica Section B, **59,** (2003), p. 463.

[21] J.B. Goodenough, Jahn-Teller phenomena in solids, Annual Review of Materials Science, **28,** (1998), p. 1.

[22] W. Baur, The geometry of polyhedral distortions. Predictive relationships for the phosphate group, Acta Crystallographica Section B, **30,** (1974), p. 1195.

[23] K. Robinson, G.V. Gibbs, P.H. Ribbe, Quadratic elongation: A quantitative measure of distortion in coordination polyhedra, Science, **172,** (1971), p. 567.

[24] R. Comes, M. Lambert, A. Guinier, The chain structure of $BaTiO_3$ and $KNbO_3$, Solid State Communications, **6,** (1968), p. 715.

[25] D. Heiman, S. Ushioda, Dispersion of the soft E-mode polariton in $BaTiO_3$, Physical Review B, **9,** (1974), p. 2122.

[26] J. Harada, J.D. Axe, G. Shirane, Neutron-Scattering Study of Soft Modes in Cubic $BaTiO_3$, Physical Review B, **4,** (1971), p. 155.

[27] M.T. Anderson, K.B. Greenwood, G.A. Taylor, K.R. Poeppelmeier, B-cation arrangements in double perovskites, Progress in Solid State Chemistry, **22,** (1993), p. 197.

[28] G. King, P.M. Woodward, Cation ordering in perovskites, Journal of Materials Chemistry, **20,** (2010), p. 5785.

[29] S. Vasala, M. Karppinen, $A2B'B''O_6$ perovskites: A review, Progress in Solid State Chemistry, **43,** (2015), p. 1.

[30] C. Meneghini, S. Ray, F. Liscio, F. Bardelli, S. Mobilio, D.D. Sarma, Nature of "Disorder" in the Ordered Double Perovskite Sr2FeMoO6, Physical Review Letters, **103,** (2009), p. 046403.

[31] P.M. Woodward, Structural distortions, phase transitions, and cation ordering in the perovskite and tungsten trioxide structures, Chemistry, Oregon State University, Corvallis, **1996**.

[32] H.A. Kramers, L'interaction Entre les Atomes Magnétogènes dans un Cristal Paramagnétique, Physica, **1,** (1934), p. 182.

[33] J.B. Goodenough, Theory of the Role of Covalence in the Perovskite-Type Manganites [La, M(II)]MnO_3, Physical Review, **100,** (1955), p. 564.

[34] J. Kanamori, Superexchange interaction and symmetry properties of electron orbitals, Journal of Physics and Chemistry of Solids, **10,** (1959), p. 87.

[35] D.I. Khomskii, Transition Metal Compounds, Cambridge University Press, Cambridge, (2014).

[36] J.B. Goodenough, Magnetism and the chemical bond, Interscience Publishers (1963).

[37] C. Zener, Interaction between the d-Shells in the Transition Metals. II. Ferromagnetic Compounds of Manganese with Perovskite Structure, Physical Review, **82,** (1951), p. 403.

[38] P.W. Anderson, H. Hasegawa, Considerations on Double Exchange, Physical Review, **100,** (1955), p. 675.

[39] P.G. de Gennes, Effects of Double Exchange in Magnetic Crystals, Physical Review, **118,** (1960), p. 141.

[40] P. Schiffer, A.P. Ramirez, W. Bao, S.W. Cheong, Low Temperature Magnetoresistance and the Magnetic Phase Diagram of $La_{1-x}Ca_xMnO_3$, Physical Review Letters, **75,** (1995), p. 3336.

[41] J.-W.G. Bos, J.P. Attfield, Magnetic frustration in $(LaA)CoNbO_6$ (A=Ca,Sr and Ba) double perovskites, Physical Review B, **70,** (2004), p. 174434.

[42] J.E. Greedan, Geometrically frustrated magnetic materials, Journal of Materials Chemistry, **11,** (2001), p. 37.

[43] K. Yoshii, Structural and magnetic properties of the perovskites $Sr_{n+1}(Co_{0.5}Nb_{0.5})_nO_{3n+1}$ ($n=\infty$, 2 and 1), Journal of Alloys and Compounds, **307,** (2000), p. 119.

[44] K. Yoshii, Magnetic Transition in the Perovskite Ba_2CoNbO_6, Journal of Solid State Chemistry, **151,** (2000), p. 294.

[45] L. Youwen, K. Yoshio, I. Shintaro, T. Yasujiro, T. Yoshinori, Synthesis of cubic $SrCoO_3$ single crystal and its anisotropic magnetic and transport properties, Journal of Physics: Condensed Matter, **23,** (2011), p. 245601.

[46] J.M. Longo, P.M. Raccah, J.B. Goodenough, Magnetic Properties of $SrRuO_3$ and $CaRuO_3$, Journal of Applied Physics, **39,** (1968), p. 1327.

[47] A.D. Lozano-Gorrín, J.E. Greedan, P. Núñez, C. González-Silgo, G.A. Botton, G. Radtke, Structural characterization, magnetic behavior and high-resolution EELS study of new perovskites $Sr_2Ru_{2-x}Co_xO_{6-\delta}$ ($0.5<x<1.5$), Journal of Solid State Chemistry, **180,** (2007), p. 1209.

[48] T. Motohashi, V. Caignaert, V. Pralong, M. Hervieu, A. Maignan, B. Raveau, Competition between ferromagnetism and spin glass: The key for large magnetoresistance in oxygen-deficient perovskites $SrCo_{1-x}M_xO_{3-\delta}$ (M = Nb, Ru), Physical Review B, **71,** (2005), p. 214424.

[49] K.R. Kendall, C. Navas, J.K. Thomas, H.-C.z. Loye, Recent developments in perovskite-based oxide ion conductors, Solid State Ionics, **82,** (1995), p. 215.

[50] M. Backhaus-Ricoult, SOFC – A playground for solid state chemistry, Solid State Sciences, **10,** (2008), p. 670.

Chapter 2.

Experimental Techniques

This chapter describes the synthesis methods and experimental techniques used while carrying out thesis work. Only a brief summary of methods and techniques will be discussed here as most of the topics are fundamental and widely available in standard text and references. Sample preparation was mostly done by solid state reaction. In the few cases where there are many reactants or small amount of doping and homogeneity is required, solution synthesis method is employed. Powder x-ray diffraction (XRD) is used for confirming the pure phase formation. Crystal structure analysis was done using XRD and powder neutron diffraction (PND). FULLPROF program was used for the Rietveld refinement of the XRD and PND data. In some cases extended x-ray absorption fine structure (EXAFS) technique is used for determining local structure and as supplementary method for determining the crystal structure. Many other techniques used for characterizing the physical properties of the compounds like DC/AC magnetization, electron paramagnetic resonance (EPR), neutron depolarization, thermogravimetry (TG), conductivity measurement, dielectric measurement, Photoluminescence (PL), X-ray absorption near edge spectroscopy (XANES), IR absorption spectroscopy, positron annihilation lifetime spectroscopy etc. are briefly discussed.

2.1 Sample preparation methods

In the solid state reaction method, solid reactants are mixed in stoichiometric amount and uniformly ground using pestle-mortar. It is then heated to required temperature profile for long hours with intermittent grinding. Long duration of heat treatment and intermittent grinding is very important in this method for two reasons – firstly solid-solid reactions take place at the boundary of reactants and are diffusion controlled, thus sluggish. So to kinetically assist these reactions high temperature and long heating is necessary. Secondly grinding helps in homogeneity and assisting the reaction. Reactants ground using a pestle - mortar is about the size of microns and does not have the atomic level homogeneity. Thus, intermittent grinding helps the product phase formed to distribute as new seeds for further reaction and to achieve atomic level homogeneity. The more detailed discussion and mechanism related to this method can be found in book by A. R. West [1].

There are different solution methods which differ slightly, but have a common step of dissolving reactants in diluted acids. Atomic level mixing of reactants gives a solution method an advantage over the solid state method. Most common of all, is the combustion method. In this method combustible fuel is added to the dissolved reactants in diluted nitric acid solution like citric acid or glycerol. Proper fuel: oxidant ratio and Ph of the solution is maintained before it is dried and fired at 300-350°C to start self ignition reaction. After ignition puffy material with some amount of residue carbon is left behind, this is then heated at high temperature in furnace to form the product. This method cannot be used when reactants are not soluble in nitric acid.

In some of the compounds, the oxidation state of the particular ions has to be maintained and requires special gas atmosphere while heat treatment. In such cases tubular furnace with the provision of flowing inert or reactive gas is used. For inert atmosphere argon or helium is used with less than 6ppm of oxygen impurity. Argon with 8% hydrogen is used as reducing gas.

2.2 Diffraction theory

Diffraction is the first technique which opened the avenue to explore the regular arrangement of atoms in the solids. Since then it has become the most powerful and widely used technique for characterizing and solving the crystal structure of the materials. Any type of radiation (electromagnetic or particle) which has wavelength of the dimension of inter atomic distances in solids can be used for caring out diffraction. Typically X-rays, thermal neutrons and high energy electron beams are used for doing diffraction experiments. Each of these methods has their own advantages and disadvantages. The basic principle underling this technique is covered in many standard references.

2.2.1 X-ray diffraction (XRD)

X-rays are electromagnetic rays which can interact with an electron cloud within the material. The wavelengths of x-ray radiation used in diffraction are in the range 0.1 to 10Å, similar to inter-atomic distances in the crystalline materials. Such wavelengths can be achieved by using characteristic x-ray lines of different elements (Table 2.1) or synchrotron x-ray source. Out of these, Cu Kα is the most widely used in lab source XRD instruments. Synchrotron x-ray source has added advantage of tuning the required wavelength for carrying out the diffraction experiment.

Table. 2.1 Characteristic x-ray of different elements.

Some commonly used X-ray K wavelengths (Å)				
Element	Kα (av.)	$K\alpha_1$	$K\alpha_2$	$K\beta_1$
Cr	2.29100	2.28970	2.29361	2.08487
Fe	1.93736	1.93604	1.93998	1.75661
Co	1.79026	1.78897	1.79285	1.62079
Cu	1.54184	1.54056	1.54439	1.39222
Mo	0.71073	0.70930	0.71359	0.63229

After the discovery of x-rays by German physicist Wilhelm Röntgen in 1895, von Laue in 1912 showed that crystalline material can act as a diffraction grating and diffract them in systematic dots like pattern. Following year Sir William Henry Bragg and his son, William Lawrence Bragg, analysed this phenomenon in the manner in which x-rays constructively or destructively reflected by planes of atoms in the solids and later used it to solve crystal structure of NaCl, ZnS and diamond. Formula given by Bragg known as Bragg's law can be explained using the Fig. 2.1.

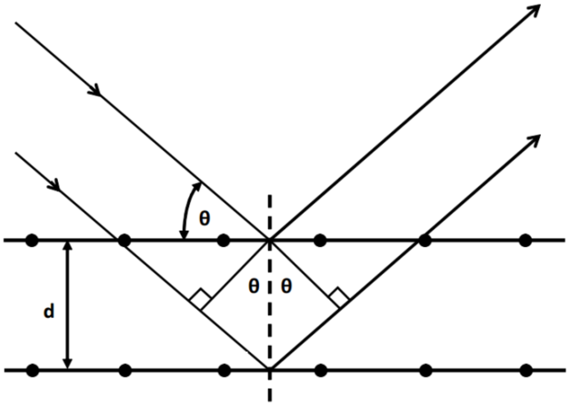

Figure 2.1 *Diffraction from a set of lattice planes, separated by a distance, 'd' [2].*

Let, 'd' be the inter-planar distance and parallel monochromatic x-ray beam of wavelength λ incident with angle 'θ' with the plane. In order to have constructive interference, the path difference 2dsinθ between reflected x-ray beams should be integral multiple of wavelength. Thus giving famous Bragg's law $2\,d\sin\theta = n\,\lambda$. Bragg reflections will occur for $\lambda \leq 2d$ depending upon the satisfaction of Bragg's law. In order to satisfy Bragg's law, either wavelength λ or diffraction angle θ can be varied leading to different methods in which one can collect the diffraction data. For each method different instrumentation is required. Typical Bragg- Brentano powder XRD method and instrumentation is shown in the Fig. 2.2.

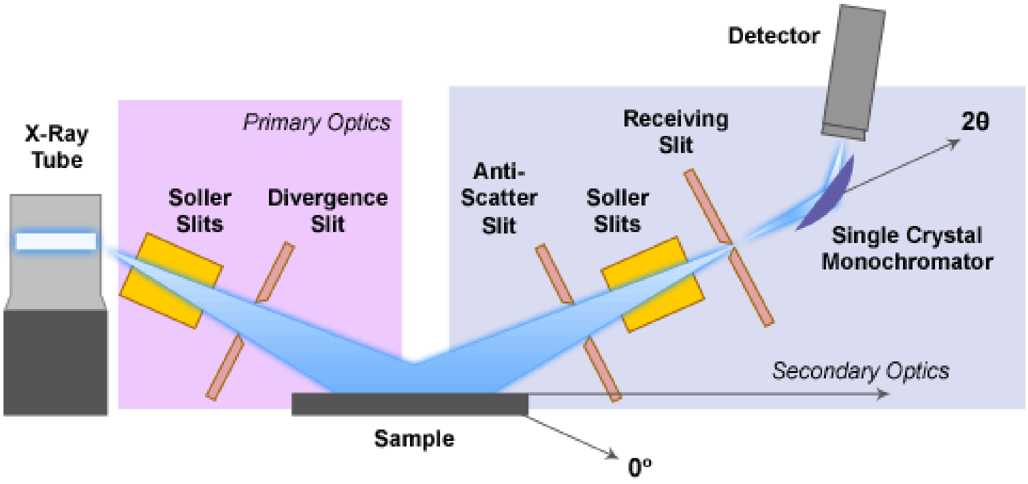

Figure 2.2 *Schematics showing typical Bragg- Brentano powder XRD method.*

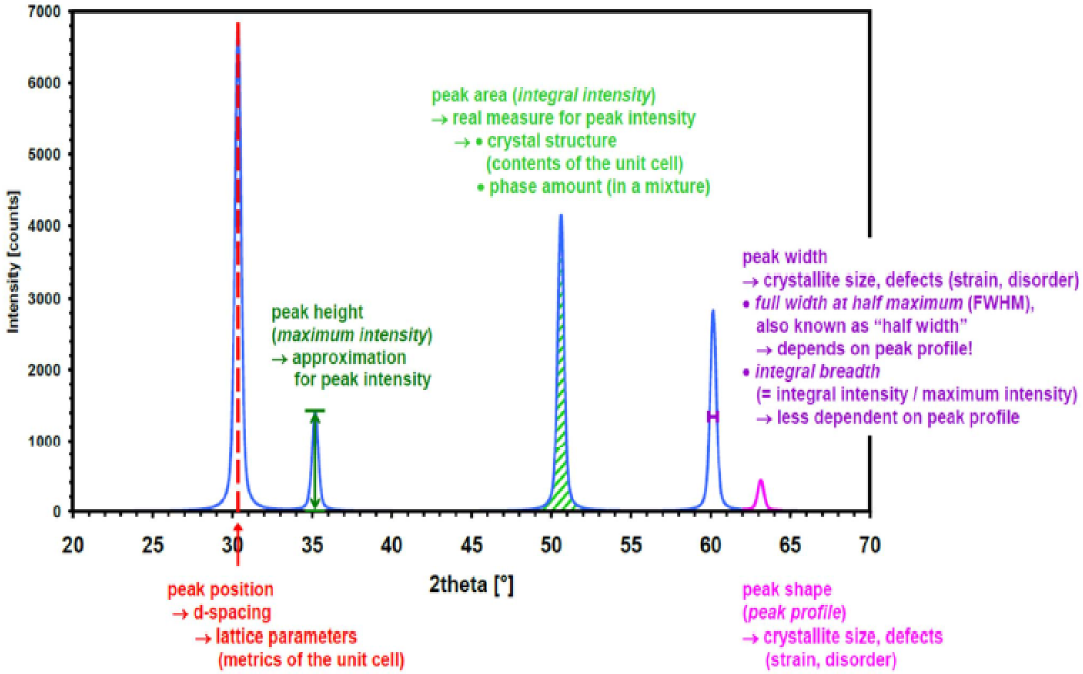

Figure 2.3 *Anatomy of XRD pattern: information obtained from XRD pattern.*

The Fig. 2.3, describes the typical powder diffraction data and the different information inferred from it. The size and symmetry of the lattice can be obtained from analyzing the position of Bragg peaks, while the intensity of the peak is dependent on the position of atoms within the unit cell. The intensity of a diffracted beam is directly related to the amplitude of the structure factor | *Fhkl* |. The intensity of a diffracted beam is given by, $I_{hkl} \propto | F_{hkl} |^2$, where $| F_{hkl} |$ is given as,

$$F_{hkl} = \left[\sum_i f_i \, e^{2\pi i (hx_i + ky_i + lz_i)} \right] e^{-B\left(\frac{sin\theta}{\lambda}\right)^2}$$

Here the summation runs over all atoms in the unit cell, fi is atomic form factor for particular atom, (hkl) are the miller indices for particular plane under consideration and (x_i y_i z_i) are fractional co-ordinates of ith atom inside unit cell. The second exponential factor is due to thermal Debye-Waller factor where, $B = 8\pi^2 U$. In this expression *U* is the isotropic temperature factor, which is equal to the square of the mean displacement of the atom from its equilibrium position. Therefore, the intensity of a diffracted beam decreases as the temperature is raised. At a given temperature, thermal vibration causes exponential decrease in the intensity as the reflected angle increases.

RIGAKU Miniflex 600, STOE and RIGAKU TTRAX XRD instruments has been used in the current study. STOE instrument has an additional attachment for recording XRD data at high temperature up to 1000°C.

XRD technique can be used for various purposes as given below:

1. Phase identification which is the most primary and important purpose of XRD technique.
2. Finding the crystal symmetry and lattice parameters.
3. Crystal structure parameters like atomic positions, temperature Debye-Waller factors, occupancy.
4. It is used for quantifying the phase percentage in mixture of phases.
5. Determination of particle size and strain in the materials.

6. Determining the texture of the material.

Limiting factors of XRD technique are:

1. Intensity of the reflected lines decreases at higher diffracted angle because of decrease in the form factor of the elements.
2. Scattering of the X-rays from the atom is proportional to the number of electron present in it i.e atomic number Z of that element. Due to this nature of the X-ray scattering, it is difficult to identify the low Z elements in presence of heavy elements and it is difficult to identify nearby Z elements in the crystal structure determination.

There are many good texts available which discuss about the theory and instrumentation used in powder XRD method in details [2-4].

2.2.2 Powder neutron diffraction (PND):

Neutrons are produced in nuclear reaction in reactors or by bombarding heavy nuclei with high energy accelerated particles in spallation sources. The basic principle of neutron diffraction remains the same as XRD except there are few fundamental differences in both as given below [5]:

- The neutron has no electric charge; therefore, it interacts with the nucleus and not the electron cloud. As they are neutral particles, they have high penetrating power unlike X-rays. Unlike X-rays wherein the atomic scattering factor f increases with increasing Z as the number of electrons increases, for neutrons the scattering length bi is not strongly dependent on the atomic number of an atom. The scattering of the neutron from the nucleus depends on the energy of the neutron and nuclear properties on the nucleus under consideration. Thus there no particular trend of scattering factor on atomic number is observed.

- In addition to study the crystal structure of solids, the energy of thermal neutrons is comparable to the energy of elementary excitations in matter like phonons and magnons, making it suitable for the study of dynamic processes.
- An important property of neutrons is that they carry a magnetic moment of $-\gamma\mu N$, where $\gamma = 1.913$ and $\mu N = eh/2mp$ is the nuclear magneton. This interacts with unpaired electrons of magnetic atoms leading to additional scattering from magnetic solids. The resulting scattering from magnetic solids is used for magnetic structure determination and spin excitations.

These properties of neutrons have advantages and dis-advantages as follows:

Advantages:-

1. The scattering cross section varies randomly and does not depend on atomic number Z of the element. Due to this nature it is advantageous to find low Z elements in presence of heavy element and to find nearby Z elements in the crystal structure determination.
2. The most important use of neutron diffraction is for determining the magnetic structure of the compounds. Neutrons carry magnetic moment and are scattered from the magnetic moments in the sample. The long range magnetic ordering like ferromagnetic, ferrimagnetic, anti-ferromagnetic gives enhancement of intensity in few reflections or creating new supper-lattice reflection. These magnetic diffracted reflections are use for determining the magnetic structure of the materials.
3. The energy of the thermal neutrons which are equal to the thermal vibration energy in the crystals. This property of the neutrons is used for studying the dynamics in the materials like determining the phonon dispersion of the crystals and magnon dispersion in magnetic materials.

Disadvantages:-

1. Neutron sources like nuclear reactor, spallation sources are very expensive and thus few facilities are available.
2. Generally the intensity of neutron beam is weak compared to the X-ray source, due to this; large quantity of sample is needed. It is also necessary to record the diffraction pattern for longer duration to get good quality data. Moreover, depending upon the initial flux of the neutrons and the experimental setup the optimal setting is made to achieve good resolution and intensity of the PND.

Powder neutron diffraction (ND) data was recorded on the PD2 diffractometer (λ=1.2443Å), Dhruva Reactor, Bhabha Atomic Research Centre, Mumbai [6]. This beam line has facility for recording the diffraction data at different temperatures from 6K to 300K. The Fig. 2.4 shows the setup of above mentioned powder neutron diffractometer.

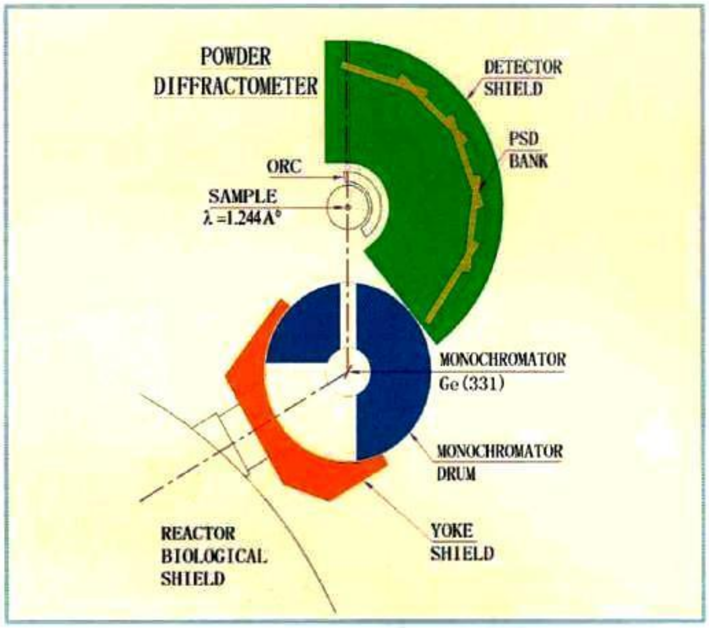

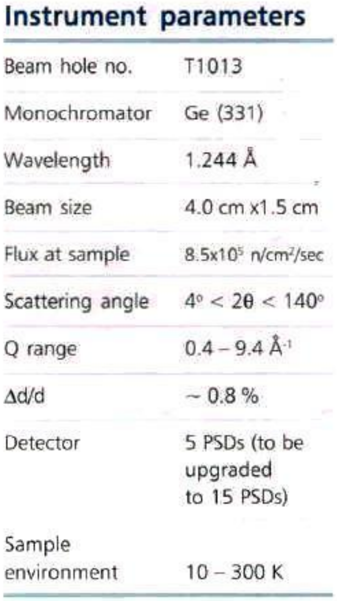

Instrument parameters

Beam hole no.	T1013
Monochromator	Ge (331)
Wavelength	1.244 Å
Beam size	4.0 cm x1.5 cm
Flux at sample	8.5×10^5 n/cm^2/sec
Scattering angle	$4^\circ < 2\theta < 140^\circ$
Q range	0.4 – 9.4 Å^{-1}
Δd/d	~ 0.8 %
Detector	5 PSDs (to be upgraded to 15 PSDs)
Sample environment	10 – 300 K

Figure 2.4 *Layout of powder neutron diffractometer at Dhruva reactor, BARC, India.*

2.3 Rietveld refinement

Rietveld refinement method was devised by scientist Hugo Rietveld [7]. It is least square fit method to match the observed x-ray or neutron diffraction pattern with the theoretically calculated diffraction pattern. The initial model for the crystal structure is necessary in this method and the theoretical diffraction pattern is calculated using this model crystal structure. Over the refinement cycles parameters related to crystal structure (magnetic structure in ordered magnetic materials) are refined to obtain the best fit.

Mathematically, difference function $\Delta Y = \sum_i w_i \left(y_i^{obs} - y_i^{cal}\right)^2$ where wi is statistical weighing factor and yobs and ycal are observed and calculated intensity, respectively. The calculated intensity ycal is given as

$$y_i^{cal} = s \sum_k L_k |F_k|^2 \phi(2\theta_i - 2\theta_k) P_k A \quad + \quad y_i^{bkg}$$

where, s is scaling factor, Lk is Lorentz-polarization factor, Fk is structure factor, φ is peak function, P_k is preferred orientation factors, A is absorption factor and y^{bkg} is background intensity.

The quality of the refinement can be evaluated from residue function given as:

Profile factor $R_p = 100 \frac{\sum_i \left|y_i^{obs} - y_i^{cal}\right|}{\sum_i y_i^{obs}}$

Weighted profile factor $R_{wp}^2 = 100 \frac{\sum_i w_i \left|y_i^{obs} - y_i^{cal}\right|^2}{\sum_i w_i \, {y_i^{obs}}^2}$, where wi is statistical weighing factor

Bragg factor $R_B = 100 \frac{\sum_k \left|I_k^{obs} - I_k^{cal}\right|}{\sum_i I_k^{obs}}$, Ik is intensity of kth Bragg reflection

Crystallographic residue factor $R_F = 100\frac{\sum_k \left|F_k^{obs}-F_k^{cal}\right|}{\sum_i F_k^{obs}}$, Fk is structure factor of kth Bragg reflection

Reduced chi-squared $\chi^2 = \left[\frac{R_{wp}}{R_{exp}}\right]^2$, where $R_{exp} = 100\left[\frac{n-p}{\sum_i w_i \, {y_i^{obs}}^2}\right]^{1/2}$, n and p are observed data points and refined parameters, respectively.

These residue factors are used as a guideline for progress of refinement and how good the model and refinement is. The Rietveld refinement is carried out using FULLPROF program [8].

2.4 Polarized neutron spectroscopy for depolarization study

Neutron beam is said to be polarized when the average spin component of the beam is non-zero. The polarization direction is defined to be the direction in which average spin component has maximum. There are crystals which are used for polarizing the neutron beam like Cu2MnAl, Co0.92Fe0.08 called polarisers. The efficiency of such crystals is defined as

P=(I↑ - I↓)/(I↑ + I↓), where I↑ and I↓ corresponds to intensity of up and down spin, respectively.

Neutron depolarization technique is used for detecting the magnetic inhomogeneities of mesoscopic length scale in micron and sub-micron range. When the polarized neutron beam passes through the sample, its mean polarization vector interacts with the magnetic inhomogenetics causing rotation of the polarization vector around the internal B field of that region. Thus the rotation of the polarization vector in the random local inhomogeneities results in the shortening of the net polarization vector called as the depolarization. In our studies we measure the quantity called Flipping Ratio given as FR $= \frac{1-P_iDP_A}{1+(2f-1)P_iDP_A}$, where *Pi* is the incident beam polarization, P_A is the efficiency of the analyzer crystal, f is the dc-flipper efficiency and D is the depolarization coefficient. PiD is thus the transmitted beam polarization. In the absence of any depolarization D=1. In this method the sample is not subjected to high magnetic field as against the field dependent magnetization M(H) measurement study. Thus it can provide information about the building magnetic correlations without perturbing the magnetic ground state. Thus it is an important technique to study ferromagnetic behaviour in the sample with coexisting ferromagnetic or anti-ferromagnetic phases.

Neutron depolarization measurements were carried out on the polarized neutron spectrometer at DHRUVA reactor, Bhabha Atomic Research Centre, Mumbai, India [6]. Fig. 2.5 shows the spectrometer setup. The single crystal monochromator cum polarizer Cu_2MnAl Heusler alloy, with (111) polarizing plane (λ =1.205Å) is employed. The Cu_2MnAl crystal is mounted between the pole pieces of a $SmCo_5$ permanent magnet assembly, which provides a vertical uniform field of 2.8kOe. Similarly, polarization sensitive analyzer, either Cu_2MnAl or $Co_{0.92}Fe_{0.08}$, can be placed in the pole gap of the $SmCo_5$ magnet assembly mounted on the third axis. BF_3 gas counters are used in both the monitor and signal channel. To carry out neutron depolarization measurements at low temperatures (2-300K) using a closed cycle refrigerator in low field environment, an electromagnet is installed to provide either a horizontal or vertical field up to 3kOe. To reverse the direction of polarization before and / or after scattering two dc flippers are used. Powdered samples studied here were packed in an aluminium can of 5mm diameter. Data acquisition and control of the spectrometer are accomplished through a computer.

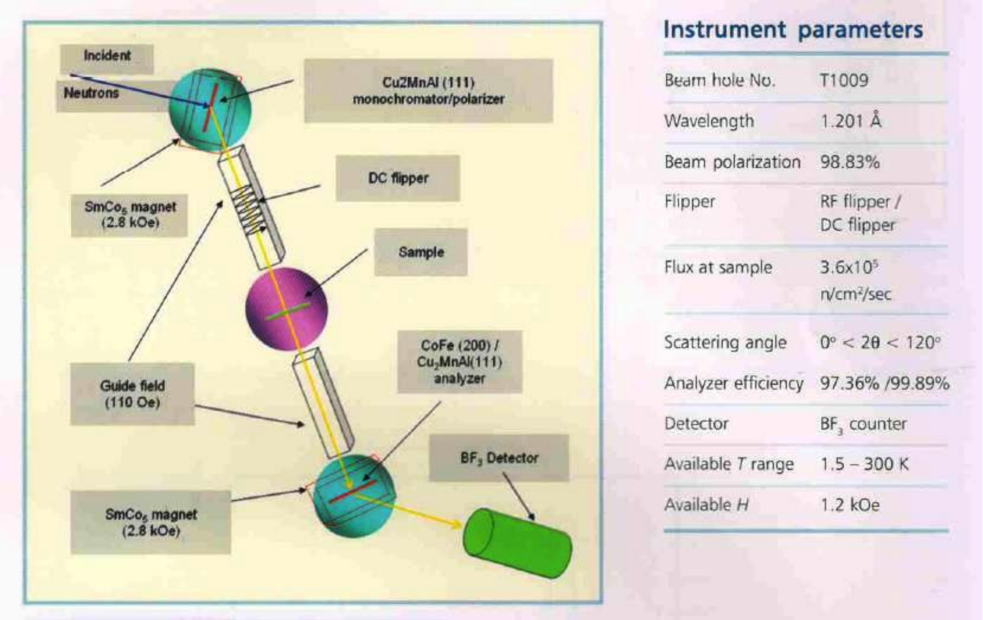

Instrument parameters

Beam hole No.	T1009
Wavelength	1.201 Å
Beam polarization	98.83%
Flipper	RF flipper / DC flipper
Flux at sample	3.6×10^5 n/cm^2/sec
Scattering angle	$0° < 2\theta < 120°$
Analyzer efficiency	97.36% /99.89%
Detector	BF_3 counter
Available *T* range	1.5 – 300 K
Available *H*	1.2 kOe

Figure 2.5 *Neutron depolarization beam-line setup at Dhruva reactor, BARC, India.*

2.5 X-ray absorption spectroscopy

X-ray absorption spectroscopy (XAS) is widely used technique to study local geometrical structure and electronic structure of the materials. This technique uses synchrotron x-ray source where there is possibility of tuning to required wavelength using monochromator and high brilliance. In this technique the wavelength of x-rays is tuned to absorption edge of particular element of interest. The measurement is performed by observing the absorption co-efficient of the material around the particular absorption edge of the element under consideration. When the energy of the incoming x-ray exceeds binding energy of core shell electron the electron absorbs the energy either to land in the higher energy empty shells to give pre-edge features in the absorption or in case of larger energy the electron is emitted as free electron called photoelectron giving huge change in the absorption co-efficient called absorption edge. The emitted photoelectron can interact with the surrounding atoms to give post edge features in the absorption coefficient. A typical x-ray absorption spectrum for FeO at Fe K-edge is shown in Fig. 2.6.

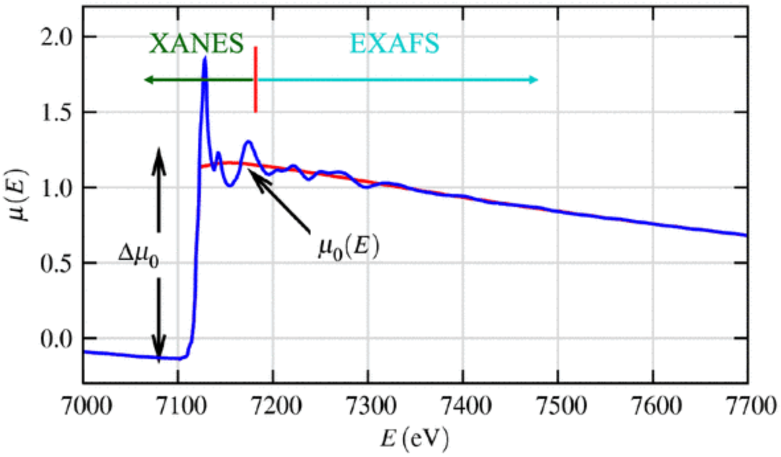

Figure 2.6 *A typical x-ray absorption spectrum for FeO at Fe K-edge.*

Depending upon the energy window scanned around the absorption edge X-ray absorption spectroscopy is named as X-ray Absorption Near Edge Structure (XANES) and Extended X-ray absorption Fine Structure (EXAFS) giving different and complementary information about the absorbing atom. XANES is 5 to 150 eV above the absorption edge and EXAFS starts from 150eV up to 2000eV above the absorption edge. XANES is the characteristic of valence and chemical environment of element under probe. Valence state of the element can be found even for minute quantity present inside the bulk by recording the XAS data in fluorescence mode. XANES spectra of standard materials where oxidation state is known can be used to determine the proportion of oxidation states in the given sample where there are mixed oxidation states. Local geometry like tetrahedral or octahedral can be distinguished comparing with the known standards. In Extended X-ray absorption Fine Structure (EXAFS) the main process is the photoelectron emitted from the core shell of the element can be considered as the outgoing spherical wave and it is scattered from the surrounding atoms. The scattered electrons can constructively or destructively interfere with the outgoing photoelectron wave to give modulations in the absorption coefficient. Modelling and refining the chemical surrounding around the probe element one can fit the modulations in the absorption coefficient. Thus one can get information like bond lengths, co-ordination number, thermal Debye-Waller factors etc from EXAFS data analysis.

The absorption coefficient μ, which gives the probability that x-rays will be absorbed according to Beer's Law: $I = I_0 e^{-\mu t}$ where μ is the absorption coefficient, I_0 is the x-ray intensity incident on a sample, t is the sample thickness, and I is the intensity transmitted through the sample. For the EXAFS, we are interested in the oscillations well above the absorption edge, and define the EXAFS fine-structure function χ(E) as

$$\chi(E) = \frac{\mu(E) - \mu_0(E)}{\Delta\mu_0(E)}$$

where, μ(E) is the measured absorption coefficient, $\mu_0(E)$ is a smooth background function representing the absorption of an isolated atom, and $\Delta\mu_0(E)$ is the measured jump in the absorption μ(E) at the threshold energy E_0. XAFS is best understood in terms of the wave behaviour of the photo-electron created in the absorption process. Because of this, it is common to convert the x-ray energy to k, the wave number of the photo-electron, which has dimensions of 1/distance and is defined as $k = \sqrt{2m(E - E_0)/\hbar^2}$ where, E_0 is the absorption edge energy and m is the electron mass. The primary quantity for EXAFS is then χ(k), the oscillations as a function of photo-electron wave number. The different frequencies apparent in the oscillations in χ(k) correspond to different near-neighbour coordination shells which can be described and modelled according to the EXAFS equation,

$$\chi(k) = \sum_j \frac{N_j f_j(k) e^{-2k^2\sigma_j^2}}{kR_j^2} \sin[2kR_j + \delta_j(k)]$$

where, f(k) and δ(k) are scattering properties of the atoms neighbouring the excited atom, N is the number of neighbouring atoms, R is the distance to the neighbouring atom, and σ^2 is the disorder in the neighbour distance. Though somewhat complicated, the EXAFS equation allows us to determine N, R, and σ^2 knowing the scattering amplitude f(k) and phase-shift δ(k). Furthermore, since these scattering factors depend on the Z of the neighbouring atom, EXAFS is also sensitive to the atomic species of the neighbouring atom.

In the present study, the measurements were carried out on the Energy-Scanning EXAFS beamline (BL-9) at the INDUS-2 Synchrotron Source (2.5 GeV, 200 mA) at Raja Ramanna Centre for Advanced Technology (RRCAT), Indore, India. Details of the optics and instrumentation are given elsewhere [9]. The absorption coefficient μ is obtained using the relation: $I_T = I_0 e^{-\mu x}$ where, x is the thickness of the absorber. Powder sample of appropriate weight, estimated to obtain a reasonable edge jump was taken in powder form and mixed thoroughly with cellulose powder to obtain total weight of 100 mg and homogenous pellets of 15 mm diameter was prepared using an electric operated hydraulic press. The set of EXAFS data analysis available within IFEFFIT software package has been used for EXAFS data analysis [10]. This includes background reduction and Fourier transform to derive the $\chi(R)$ versus R spectra from the absorption spectra (using ATHENA software), generation of the theoretical EXAFS spectra starting from an assumed crystallographic structure and finally fitting of experimental data with the theoretical spectra using ARTEMIS software [11].

2.6 Magnetic measurements

2.6.1 DC Magnetization measurements

In magnetization measurements, magnetization is measure as a function of temperature with constant magnetic field applied to the sample called as MT curve. One can also measure magnetization vs. applied magnetic field at constant temperature called as MH curve. In MT measurement one measures the magnetization depending upon the sequence of applied constant field and heating or cooling called as zero field cooled (ZFC) and field cooled (FC). In ZFC - In first step sample must be cooled without any applied magnetic field to the desired temperature, in second step data should be collected while heating with application of constant magnetic field. For FC curves, sample must be cooled with any applied magnetic field to the desired temperature. The data can be collected in two ways FCC and FCW. In FCC - Field cooled cooling, data is collected during cooling and in FCW - Field cooled warming, data is collected during heating. We can obtain the signature of spin-glass behaviour, super-paramagnetism, presence of exchange bias, and superconducting properties from ZFC-FC measurements. Also from FCC and FCW, we can get information about first order (martensitic transformations) and second order transformations.

2.6.1.1 Vibrating sample magnetometer (VSM)

Vibrating sample magnetometer is based on the Faraday's law which states that emf is generated in coil by changing the magnetic flux through the coil. The sample having magnetization is vibrated in sinusoidal motion between pick-up coils causing induced emf in it. In the coil has n turns with cross section area A then, emf V generated in coil is given by $V = -NA\frac{dB}{dt}$. For sample with magnetization M placed in field H, $B = \mu_0(H + M)$. During vibration magnetization varied as $M=M_0\sin(\omega t)$. The emf signal is amplified using lock-in amplifier and analysed. Thus electric output signal Vis proportional to magnetization of the sample and frequency of vibration.

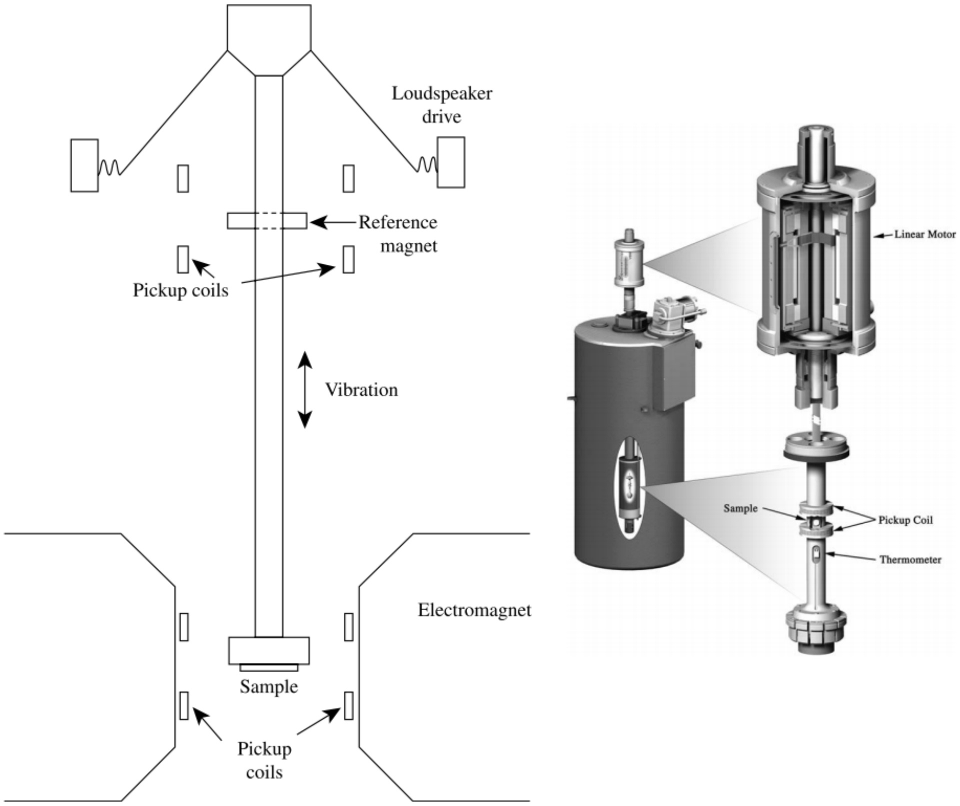

Figure 2.7 *Schematics of the vibrating sample magnetometer (VSM) and commercial VSM instrument where loudspeaker is replaced by linear motor.*

2.6.1.2 Superconducting Quantum Interference Device (SQUID)

SQUID magnetometer uses a ring of superconductor with insulating layer in between to form parallel Josephson junction to calculate the flux passing through it. SQUID is highly sensitive because ideally this device can measure single magnetic flux quanta passing through it. In particular, it is the only method which allows to directly determining the overall magnetic moment of a sample in absolute units. Sample is linearly moved through the centre of superconducting wire loops (pickup coils) producing induced current in it which is then passed through transducer coil connected to SQUID probe. SQUID probe then converts the flux to voltage signal which is amplified and analysed by magnetometer electronics. In the current work, DC magnetization measurements were done in ZFC and FC mode using the SQUID magnetometer (Quantum Design).

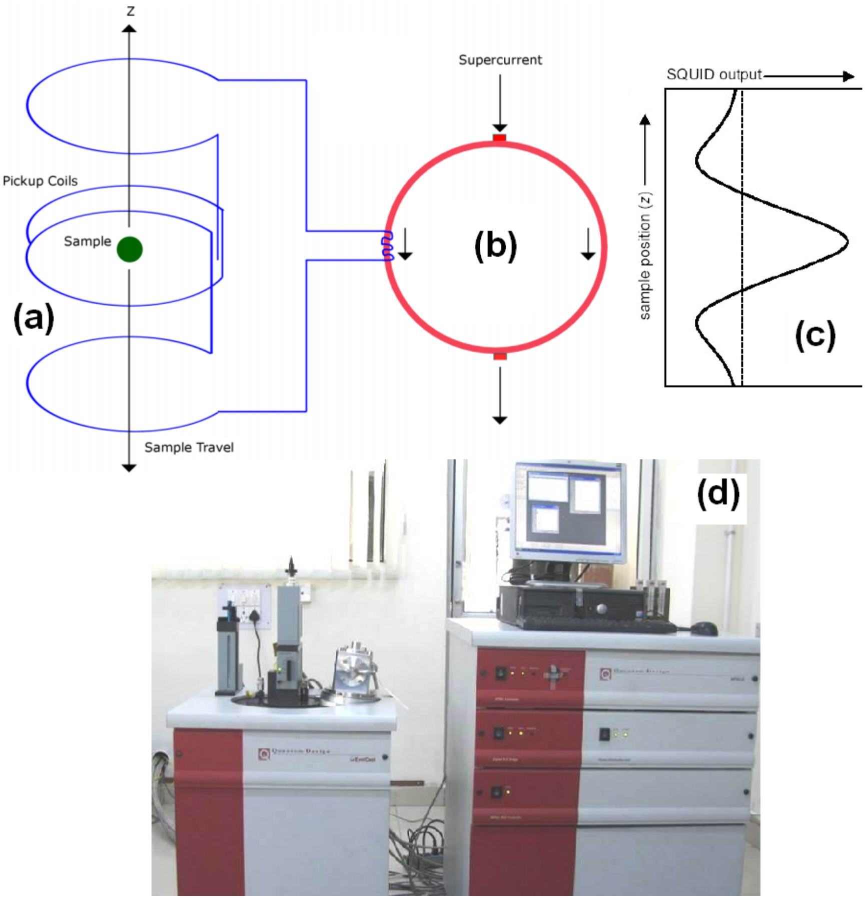

Figure 2.8 *a) The sample is linearly moved across the superconducting pick-up coil and b) the flux is linked with SQUID probe. c) The output voltage signal is fed to electronics for data processing. d) Quantum design commercial SQUID magnetometer.*

2.6.2 AC Susceptibility measurement

In AC magnetic measurements, AC field is applied to a sample and the resulting AC moment is measured which is important tool for characterizing many materials. The induced sample moment is time-dependent and the AC measurements yield information about magnetization dynamics which are not obtained in DC measurements, where the sample moment is constant and not dependent on time.

In this method a small AC magnetic field is applied to the sample in addition to the presence of static magnetic field to induce time dependent magnetic moment in the sample. The pickup coil measures this time varying magnetic moment in the sample to measure the AC magnetic susceptibility induced in the sample. In the lower frequency limit, the measured AC moment resembles the DC measurements. With small AC field, the measured AC moment M_{AC} = (dM/dH) . H_{AC} sin(ωt), where H_{AC} is the amplitude of the driving field, ω is the driving frequency, and χ = dM/dH is the slope of the M(H) curve, called the susceptibility. One clear advantage of the AC measurement is that the measurement is very sensitive to small changes in M(H). Since the AC measurement is sensitive to the slope of M(H) and not to the absolute value, small magnetic shifts can be detected even when the absolute moment is large. At higher frequencies, the AC moment of the sample does not follow the DC magnetization curve due to the dynamics effects in the sample. The observed susceptibility is the complex quantity given as $\chi = \chi' + i\chi''$, where χ' is real (in phase with drive signal) component and χ'' is imaginary (out of phase with drive signal) component of magnetic susceptibility. The imaginary component χ'' gives the dissipative processes in the sample. AC magnetic susceptibility can be measured as a function of temperature, driving frequency, DC field bias, AC field amplitude, and harmonic measurements. AC measurements are helpful for identifying weak magnetic phase transitions and identification of slow spin dynamics in the materials like spin glasses and super-paramagnetism. An AC susceptibility measurement is one of the most important measurements for characterizing spin glass materials. In spin glass the freezing temperature is determined by measuring χ' vs. temperature, a curve which reveals a cusp at the freezing temperature and the cusp temperature shift to higher side with increase in the frequency. Additionally, the relaxation and irreversibility in spin glasses leads to a non zero χ'' below the spin glass freezing temperate.

In the current work, AC magnetic susceptibility measurement was measured using SQUID-VSM (Quantum Design) between 2 and 300 K in ac field of 1 Oe in the frequency range 13–1000 Hz.

2.7 Electron Paramagnetic Resonance (EPR) spectroscopy

Electron paramagnetic resonance (EPR) spectroscopy is used for studying paramagnetic materials which contains unpaired electrons. It is also often called ESR, Electron Spin Resonance. A wide variety of materials can be studied using EPR like free radicals, many transition metal ions, and defects in materials.

EPR is a magnetic resonance technique very similar to NMR, Nuclear Magnetic Resonance. However, instead of measuring the nuclear transitions in our sample, we are detecting the transitions of unpaired electrons in an applied magnetic field. Let the ion containing unpaired electron i.e paramagnetic ion have total angular momentum equal to $'J'$ then the corresponding magnitude of magnetic moment is given by $\mu = g_J \mu_B \sqrt{J(J+1)}$ where gJ and μB is Lande g-factor and Bhor magneton. When this ion is placed in the magnetic field with strength B_0, the energy levels is split into m_J given by $E_J = m_J g_J \mu_B B_0$, where m_J is magnetic quantum number which can take on any of 2j + 1 values from -J, -J+1,…0...J, J+1. The energy difference between two energy levels is $\Delta E = g_J \mu_B B_0$ and the system can move from one state to another by absorbing ΔE quantity of energy in the form of photon with energy hυ. Generally the photon energy lies in the energy range of microwave and is kept constant for technical reasons. Table 2.2 shows typical microwave energies available in the commercial instruments. The magnetic field strength is varied to achieve the resonance absorption $\Delta E = g_J \mu_B B_0 = h\upsilon$. For the simple case with L=0, J=S=1/2, this process is shown in the Fig. 2.9

Table 2.2 Microwave frequencies commonly available in EPR spectrometers.

Designation	ν /GHz
L	1.1
S	3.0
X	9.5
K	23
Q	35
W	95

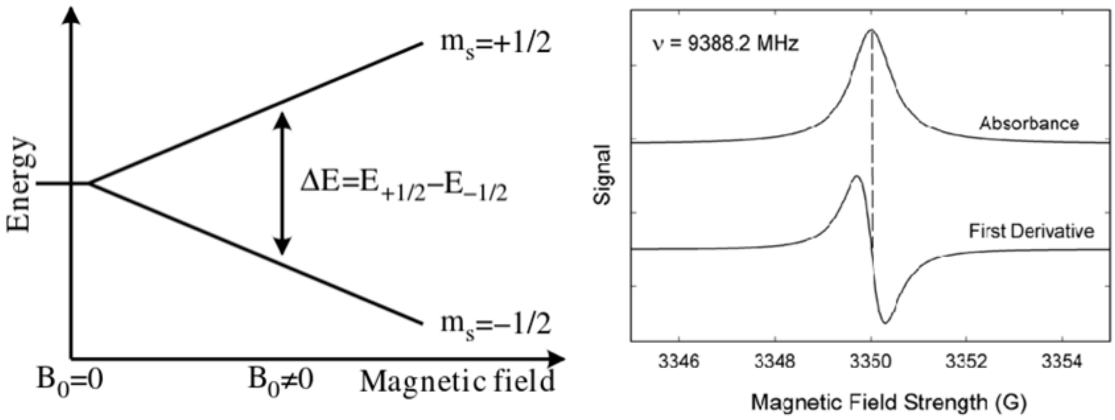

Figure 2.9 *Energy separation between the lower and the upper state for S=1/2 and EPR absorption spectra.*

The EPR experiment basically gives the observable value of gyromagnetic ratio g_J. In principle the g value can be anisotropic quantity i.e. its value depends on the direction of observation (orientation dependent). The basic components of EPR spectrometer are: a source of electromagnetic radiation (EMR), a sample cavity, and a detector. To acquire a spectrum, we can vary the frequency of the EMR and measure the amount of radiation which passes through the sample with a detector to observe the spectroscopic absorptions. In an EPR spectrometer, the source of the microwave radiation is a Klystron or a Gunn-diode. The source provides a limited range of variable frequency. The microwave source and the detector are in a box called the microwave bridge. To measure the EPR spectrum of a paramagnetic sample, the sample is placed in a magnetic field of a resonator cavity in which microwave power is concentrated. The sample is so positioned inside the resonator cavity that the electrical component of the EMR is at its minimum and the magnetic component is at its maximum.

At the sample, the static magnetic field (H) is applied perpendicular to the microwave magnetic field. The interaction of magnetic spins with the oscillating magnetic field of the electromagnetic radiation leads to the EPR transitions. An electromagnet having sweep width ranging from 5000 G to 15000 G can be used. The microwave energy is modulated and the microwave power absorbed by the sample at the resonance is measured by the phase sensitive detector, the signal is amplified and fed to a computer for data processing. A semiconductor silicon-tungsten diode is used as a detector. Earlier, the EPR spectrum used to be recorded as a function of absorption intensity against magnetic field. Such a curve often produces broad absorption bands. In modern instrument, the first derivative of the absorption intensity (dA/dH, i.e. slope) is plotted against H. This type of plot gives more accurate g values. It may be noted that the resonance field H is not a unique fingerprint for identification of the paramagnetic species because spectra can be acquired at different frequencies. Fig. 2.10 shows the block diagram of typical EPR spectrometers. Fig. 2.11 shows the photographs of EPR spectrometer used in current studies. The most widely used EPR spectrometer is the X-band spectrometer operating in the frequency range 9-10 GHz. The sensitivity of an EPR spectrometer is directly proportional to the square of the frequency, and a high frequency is preferred for a better resolution of the EPR signal. The sensitivity of the Q band spectrometer is fifteen times than that of X band spectrometers.

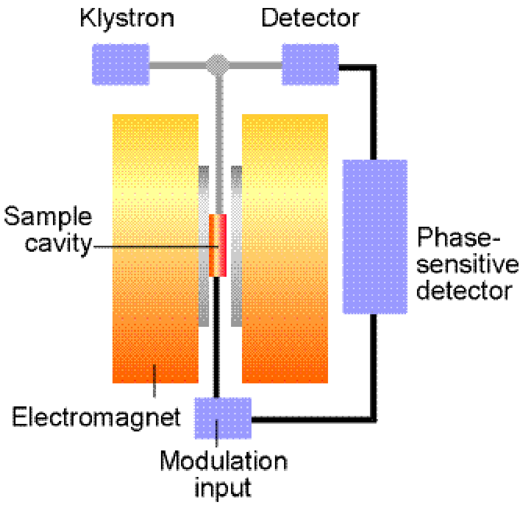

Figure 2.10 *Block diagram of typical EPR spectrometers.*

Figure 2.11 *Photograph of Bruker ESP-300 EPR spectrometer.*

2.8 Conductivity measurement: Four probe resistivity measurement

Transport properties like resistivity measurements can be done using four probe measurement technique. Sintered rectangular piece of sample is used where collinear equidistant four wire contacts are made using silver paste. The current I is passed through the outer two probes and voltage V is measured between inner two probes. The measured resistance $R = \frac{V}{I}$ is converted into resistivity ρ values by $\rho = \frac{RA}{l}$ where, A is the cross-sectional area of the rectangular sample through which the current flows and l is the distance between the current contacts. This technique minimizes the effect of contact resistance while measuring small resistance of samples and thus increases the accuracy of measurement as compared to common two contact measurement.

The temperature dependence of resistivity is measured by cooling the sample using closed cycle refrigerator. The entire measurement system comprises of a 2182 Keithley nanovoltmeter, a current source and the oxford instrument temperature controller, which were interfaced with a computer for automatic data acquisition.

2.9 Dielectric measurement

There are many methods to measure the dielectric constant of the materials but the simplest of them is measurement of the capacitance value of the sample where dielectric permittivity can be obtained as a function of temperature and frequency. The relative permittivity or dielectric constant is a complex quantity given as $\varepsilon(\omega) = \varepsilon'(\omega) - i\varepsilon''(\omega)$, where ε' is real part (in phase with input signal) and ε'' is complex part (out of phase with input signal).

In the present study, an impedance analyzer (Novocontrol) is used to carry out dielectric studies over a wide temperature and frequency range. The dielectric measurements are performed in the frequency range of 100Hz to 5MHz with rms ac voltage of 1V at temperatures from 123 to 293K using a Novocontrol Quatro liquid nitrogen cooling system and a Novocontrol BDS1200 sample holder. Samples in the form of pellets were sandwiched between the electrodes of the sample cell and the contacts were made by applying silver paste on both surfaces of the pellet. The system is fully computer-controlled, and includes software for data analysis.

2.10 Thermogravimetry (TG) and differential thermal analysis (DTA)

In this measurement a weight of the sample is measured while heating or cooling cycle using electronic weight balance. Generally TG instrumental setup is also accompanied with additional technique called as differential thermal analysis (DTA). In DTA, temperature difference between sample and the standard reference material is noted as a function of temperature. This both techniques can be supplementary to each other and gives lot of information about the thermal behaviour of the samples. In TG/DTA method small amount of sample ranging from few milligrams to few grams can be loaded in the small cups made of alumina or platinum. A similar cup with almost same quantity of reference material generally alumina powder is place right next to the sample cup but without any physical contact between them. This whole assembly is mounted over the electronic weighing balance. The cups assembly is surrounded by furnace which can be heated with required heating ramp and required temperature. Additionally, the sample chamber can be flushed with required gas which can be inert or reactive. The temperature of the sample and reference material is recorded separately and continuously using thermocouple over the whole heating and cooling cycle as required. The weight changes in the sample (TG signal) and the difference between sample and reference (DTA signal) are recorded with respect to sample temperature and these signals are further amplified, analysed electronically and fed to computer. Fig. 2.12 shows the basic block diagram of TG/DTA instrument. As TG/DTA instruments needs to be calibrated for temperature and weighing balance using standard references. Decomposition of compounds like calcium oxalate and copper sulphate are used for weight calibration while melting point of standard metals is used for calibration of temperature.

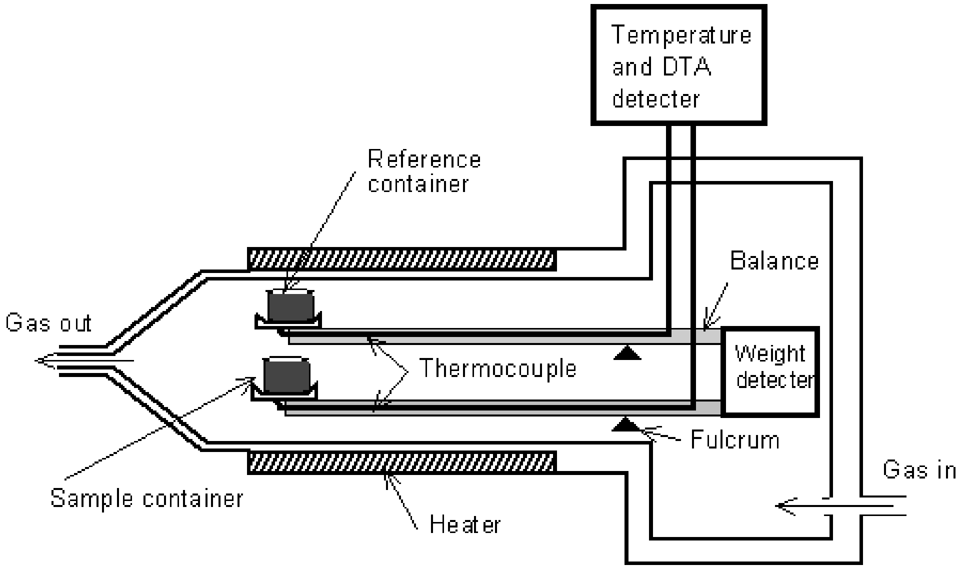

Figure 2.12 *Block diagram of TG/DTA instrument.*

Simultaneous use of TG and DTA can be used for studying various thermal behaviours of the samples as given in the table below:

Thermal behaviour	**Thermal analysis**	**Differential thermal analysis**
Thermal Decomposition with weight changes	Change in weight	Positive peak for exothermic reaction and negative for endothermic reaction
Thermal Decomposition without weight changes	No change in weight	Positive peak for exothermic reaction and negative for endothermic reaction
Melting	No change in weight	Positive peak for exothermic reaction and negative for endothermic reaction
Oxidation	Weight gain	Exothermic peak
Reduction	Weight loss	Endothermic peak
Ferromagnetic phase change (using magnet below sample cup)	Pseudo weight change	No change

2.11 Photoluminescence (PL)

Photoluminescence spectroscopy is analytical technique that can determine quantities such as emission and excitation spectra and luminescence lifetimes. By this technique, a sample is excited by photons (generally in UV range) and the excess energy released by the sample through the emission of light can be detected and recorded for different modes, i.e. excitation, emission and luminescence decay lifetime. An emission spectrum is the wavelength distribution of an emission measured at a single constant excitation wavelength. An excitation spectrum is the dependence of emission intensity, measured at a single emission wavelength, upon scanning the excitation wavelength. With a pulsed excitation source and a fast detector the spectrofluorometer can record the luminescence lifetime decay curve. A fluorescence decay time is a measurement, at fixed wavelength, of fluorescence signals as a function of time. A decay curve is a spectrum measured within a narrow time-window during the decay of the fluorescence of interest. Two requirements for lifetime measurements are a pulsed excitation source (pulse duration short in comparison with the excited-state lifetime of the molecule) and a fast detector.

In photoluminescence spectroscopy, the species is first excited (by absorbing a photon) from its ground electronic state to one of the various vibrational states in the excited electronic state. Collisions with other molecules cause the excited molecule to lose vibrational energy until it reaches the lowest vibrational state of the excited electronic state. The molecule then drops down to one of the vibrational levels of the ground electronic state, emitting a photon in the process. As molecules may drop down into any of several vibrational levels in the ground state, the emitted photons will have different energies. These processes are often visualised with the Jablonski diagram shown in Fig. 2.13.

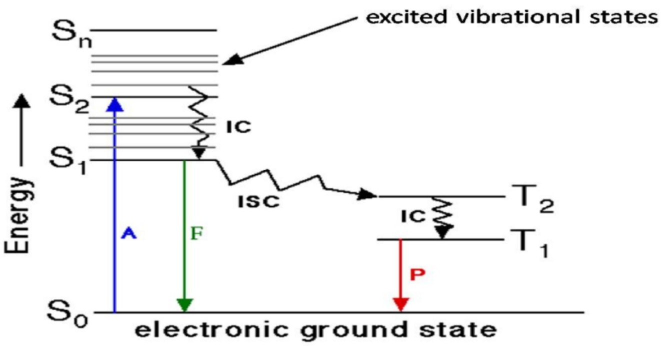

Figure 2.13 *A Jablonski diagram shows the possible relaxation processes in a molecule after the molecule has absorbed a photon (A): IC = internal conversion, ISC= intersystem conversion, F= fluorescence, P= phosphorescence.*

The source produces light photons. Various light sources may be used as excitation sources, including lasers, photodiodes, and lamps. Photons impinge on the excitation monochromator, which selectively transmits light in a narrow range around the specified excitation wavelength. The transmitted light passes through adjustable slits that control intensity and resolution by further limiting the range of transmitted light. The filtered light passes into the sample. Emitted light goes through a filter to prevent the excitation light entering the detector and causing second order peaks. The filtered light then enters the emission monochromator, which is often positioned at a 90° angle from the excitation light path to eliminate background signal and minimize noise due to stray light. Again, emitted light is transmitted in a narrow range centered on the specified emission wavelength and exits through adjustable slits, finally entering the photomultiplier tube (PMT). Schematic diagram of a general purpose spectrofluorometer are illustrated in Fig. 2.14.

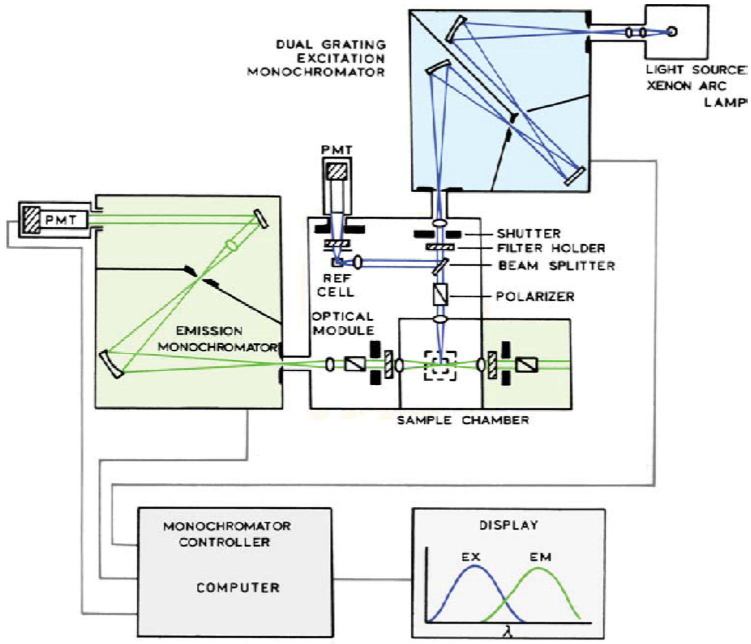

Figure 2.14 *Block diagram of spectrofluorometer.*

The trivalent europium ion (Eu^{3+}) is well known for its strong luminescence in the red spectral region, but this ion is also interesting from as study on Eu^{3+} doped samples gives qualitative idea of local environment around the Eu^{3+} ion in the host structure. Among all the rare earth ions, trivalent europium ion is most extensively explored spectroscopic probe [12], because of its relatively simpler energy-level diagram and non-degenerate ground ($^7F_0$) and excited ($^5D_0$) states. As a consequence of this, the emission spectra of Eu^{3+} show a strong dependence on its local site symmetry in the host material in which it's being doped. Fig. 2.15, shows the energy diagram of Eu^{3+} ($4f^6$) ion. The main transitions which are important as local structural probe are $^5D_0 \rightarrow {}^7F_1$ and $^5D_0 \rightarrow {}^7F_2$. The orange emission (590–600 nm) of Eu^{3+} due to the even parity magnetic dipole transition (MDT) $^5D_0 \rightarrow {}^7F_1$ is not influenced much by the local site symmetry, because they are parity-allowed, while the red emission (~610–630 nm) due to the odd-parity electric dipole transition (EDT) of $^5D_0 \rightarrow {}^7F_2$ ($\Delta J = \pm 2$), being hypersensitive, is affected by the site symmetry of Eu^{3+} ion. In a lattice site with inversion symmetry (Ci) the EDTs are strictly forbidden and the MDTs are usually the strongest emission line. In a site without inversion symmetry, the intensity of EDT is higher and thus the $^5D_0 \rightarrow {}^7F_2$ ($\Delta J = \pm 2$) transition is usually the strongest emission line. The symmetry around the lanthanide ion can thus be obtained from the shape of the emission spectrum of the Eu^{3+} ion.

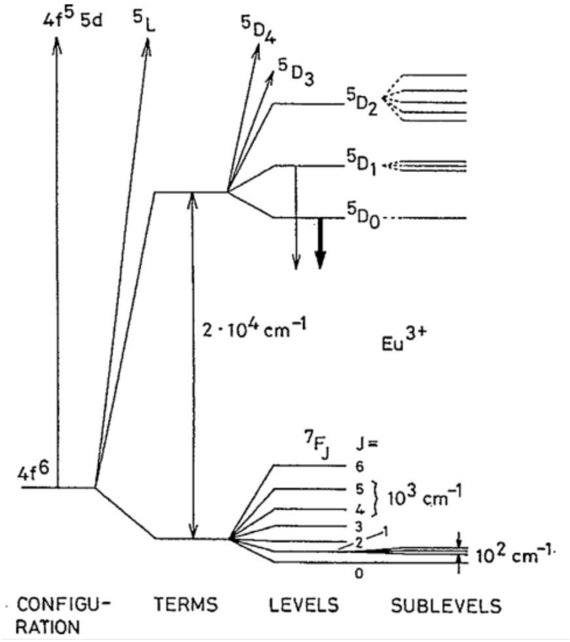

Figure 2.15 *Energy diagram of Partial energy diagram of* Eu^{3+} *(*$4f_6$*) showing the relative magnitude of the inter-electronic repulsion (terms), spin–orbit coupling (levels) and crystal-field effects (sublevels). The downward arrows indicate the excited states* $^5D_0$ *and* $^5D_1$ *from which luminescence occurs [12].*

2.12 Infrared spectroscopy (IR-spectroscopy)

IR-spectroscopy as similar to other spectroscopic techniques can be used to identify and study chemicals. Generally the vibrational energy at atomic scales fall in the range of IR region and thus this method is also called as vibrational spectroscopy. Infrared (IR) light passing through a sample is measured in order to determine the chemical functional groups in the sample. Different functional groups absorb characteristic frequencies of IR radiation. An IR spectrum is essentially a graph of infrared light absorbance (or transmittance) on the vertical axis vs. frequency or wavelength on the horizontal axis. Typical units of frequency used in IR spectra are reciprocal centimeters (sometimes called wave numbers), with the symbol cm^{-1}. A common laboratory instrument that uses this technique is a Fourier transform infrared (FTIR) spectrometer. The FTIR spectrometers with especial accessory can measure a wide variety of sample types such as gases, liquids, and solids. For convenience the infrared region can be divided into three parts: near, mid and far infrared (Table 2.3). The part of the mid infrared region between 4000 – 400 cm^{-1} is the most useful one.

Table 2.3 Infrared band divided into three regions.

Region	**Wavelength range**	
	μm	**cm^{-1}**
Near	0.78-2.5	12800-4000
Mid	2.5-50	4000-200
Far	50-1000	200-10

In diatomic molecule, the atoms can be considered to be connected with each other with spring. If the spring constant is ‘k’ then the principle vibration frequency is given as $\nu = \frac{1}{2\pi c}\sqrt{\frac{k}{\mu}}$, where c is the speed of light, and μ is the reduced mass of the A–B system given as $\mu = \frac{m_A+m_B}{m_A m_B}$ (m is the mass of atoms). When the IR photons of energy $h\nu$, is incident the molecule absorbs the photons and the molecule starts vibrating which is called as resonance condition. In complex molecules with N number of atoms, linear molecules have 3N – 5 degrees of vibrational modes, whereas nonlinear molecules have 3N – 6 degrees of vibrational modes (also called vibrational degrees of freedom). Out of these modes only those modes will absorb IR which has net change in electric dipole moment during the vibration. These modes are called as IR-active. Thus in general all modes are not IR-active and those can be observed using Raman spectroscopy. In solids the same principles apply, but the vibrations of the lattice instead of individual molecules must be considered. Every chemical group has their signature absorption frequencies or bands, and thus can be used for identification.

2.13 Positron annihilation lifetime spectroscopy (PALS)

Positron annihilation lifetime spectroscopy (PALS) is a non-destructive spectroscopy technique to study voids and defects in solids. Positron annihilation spectroscopy (PAS) is a well established technique to study the electronic structure and defects in materials [13].The lifetime of positrons depends on the electron density at the annihilation site. The positron annihilates with electrons in the material. This annihilation releases two gamma rays of 511keV energy each. The time between emission of positrons from a positron source (correlated with emission of 1.27MeV gamma ray of ^{22}Na positron source) and detection of 511keV gamma rays due to annihilation corresponds to the lifetime of positron. When positrons are injected into a solid body, they interact in some manner with the electrons in that species. For solids containing free electrons (such as metals or semiconductors), the implanted positrons annihilate rapidly unless voids such as vacancy defects are present. If voids are available, positrons will reside in them and annihilate less rapidly than in the bulk of the material, on time scales up to ~ 1 nanosecond. Positrons have high affinity for open volume defects and in the presence of defects; the electron density experienced by positron is reduced leading to increase in its lifetime. Thus, positron lifetime spectroscopy is capable of giving information about the size, type and relative concentration of various defects/vacancies even at ppm level concentration. Doppler broadening technique, on the other hand, measures the momentum distribution of the annihilating electrons. The low momentum part of the Doppler spectrum (511 keV gamma line) arises mainly from the annihilation with the valence electrons and the core electrons that can be taken as signature of an element, contribute to the high momentum part of the spectrum. A very small fraction of positrons annihilate with core electrons due to the repulsion of positron by the positively charged nucleus. The amplitude of the high momentum or core electron component is, therefore, low and it is buried in the Compton background in conventional Doppler spectrum. Coincidence Doppler broadening (CDB) technique using two HPGe detectors, is capable of eliminating the background to a great extent, e.g., peak to background ratio of ~ 10^6 can be obtained as compared to a few hundred in conventional Doppler technique. This enables unambiguous extraction of the shape and magnitude of the high momentum part of the Doppler spectrum. The chemical surrounding of the annihilation site or elemental specificity is obtained from the shape/magnitude of the high momentum core component, which carry the signature of the element. Since the core electron momentum distribution is not influenced by the physical or chemical state of the element, the CDB technique is capable of identifying the elements at the annihilation site irrespective of its physical or chemical state in the sample. Therefore, combined use of lifetime spectroscopy (LTS) and CDB technique can provide valuable information about the vacancy structure. A schematic representation of PALS technique and instrumentation is shown Fig. 2.16.

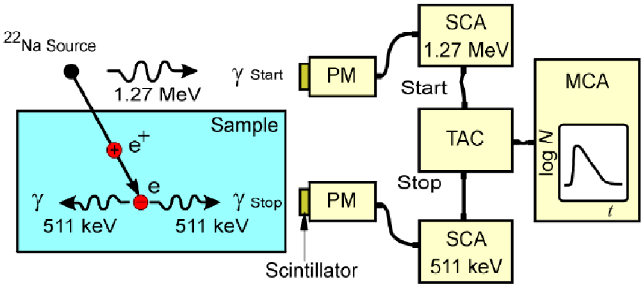

Figure 2.16 *The conventional positron lifetime measurement system*

2.14 References

[1] A.R. West, Solid State Chemistry and its Applications, Wiley (2014).

[2] B.D. Cullity, Elements of X-ray Diffraction, Addison-Wesley Publishing Company (1978).

[3] R.E. Dinnebier, S.J.L. Billinge, Powder Diffraction: Theory and Practice, Royal Society of Chemistry (2008).

[4] V. Pecharsky, P. Zavalij, Fundamentals of Powder Diffraction and Structural Characterization of Materials, Second Edition, Springer US (2008).

[5] G.E. Bacon, Neutron Diffraction: By G. E. Bacon. 3d Ed, Clarendon Press (1975).

[6] V.K. Aswal, D.Sen, R.Mukhopadhyay, S.L.Chaplot, National Facility for Neutron Beam Research [NFNBR], 2013. http://www.barc.gov.in/publications/tb/nfnbr-2013.pdf.

[7] R.A. Young, The Rietveld Method, Oxford University Press (1995).

[8] J. Rodriguez-Carvajal, Fullprof 2000: A Program for Rietveld, Profile Matching and Integrated Intensity Refinements for X-ray and Neutron Data, Laboratoire Leon Brillouin, Gif sur Yvette, France, **2000**.

[9] S. Basu, C. Nayak, A.K. Yadav, A. Agrawal, A.K. Poswal, D. Bhattacharyya, S.N. Jha, N.K. Sahoo, A comprehensive facility for EXAFS measurements at the INDUS-2 synchrotron source at RRCAT, Indore, India, Journal of Physics: Conference Series, **493,** (2014), p. 012032.

[10] M. Newville, IFEFFIT : interactive XAFS analysis and FEFF fitting, Journal of Synchrotron Radiation, **8,** (2001), p. 322.

[11] B. Ravel, M. Newville, ATHENA, ARTEMIS, HEPHAESTUS: data analysis for X-ray absorption spectroscopy using IFEFFIT, Journal of Synchrotron Radiation, **12,** (2005), p. 537.

[12] K. Binnemans, Interpretation of europium(III) spectra, Coordination Chemistry Reviews, **295,** (2015), p. 1.

[13] R.W. Siegel, Positron Annihilation Spectroscopy, Annual Review of Materials Science, **10,** (1980), p. 393.

Chapter 3.

Crystal Structure and magnetic properties of $Sr_2Co_{2-x}Ru_xO_6$ (x = 0.5, 1, 1.5) compounds.

3.1 Introduction

In this chapter we start with a brief introduction to cobalt (3d) and ruthenium (4d) based perovskites and discusses their properties. Cobalt is an interesting candidate in 3d transition metal series because like other transition metals it can exist in multiple oxidation states viz. $Co^{2+}(3d^7)$, $Co^{3+}(3d^6)$ and $Co^{4+}(3d^5)$. It has one distinct ability to have multiple spin states like low spin (LS), intermediate spin (IS) and high spin (HS) possible in octahedral geometry [1]. The multiple oxidation states offered by cobalt make it possible to have a wide range of stoichiometric as well as non-stoichiometric compounds where it can co-exist in different oxidation states simultaneously. Moreover its different spin states have an opportune to create novel magnetic and transport properties. The different spin states of Co and Ru in octahedral geometry are summarized in table 3.1. These different spin states originate because of comparable crystal field stabilization energy and pairing energy of electrons. Spin states of Co^{3+} are sensitive to Co-O bond length and Co-O-Co bond angle and thus spin states changes by varying pressure, temperature, magnetic field or doping (chemical pressure).

In Co^{2+} (HS) state, electrons are generally localized. Due to the small transfer energy of t_{2g} band, it is difficult for electrons to be transferred from t_{2g} band to top e_g band of HS Co^{3+} and similarly it is also not possible to transfer to LS Co^{3+} due to large spin flip. Thus compounds having valence state with pure Co^{2+} are insulators, while the compounds with valance in between 2+ and 3+, carriers are restricted only to Co^{2+}, inducing charge and/or spin ordering. In contrast, LS Co^{4+} is less stable and oxygen ligand hole is likely to exist in such systems. Such ligand hole induces ferromagnetic and metallic properties in mixed Co^{3+}/Co^{4+} systems.

Ruthenium element has its special position among 4d transition elements due to its interesting magnetic and electric properties. Ruthenium also shows multiple oxidation states from 3+ to 7+, where Ru^{4+} and Ru^{5+} are more frequently observed in the solid compounds with a normal synthesis methods. The crystal field splitting is strong in second row transition metals and as a result ruthenium adopts the (LS) configuration in both these oxidation states as shown in table 3.1. Ruthenium being a 4d ion it generally has more extended d orbitals than the corresponding 3d ions, and as a result it exhibits greater overlap and hybridization between the transition metal and O 2p orbitals [2].

Table3.1 Electronic and spin states configuration of cobalt and Ruthenium in different oxidation states.

	Cobalt			**Ruthenium**	
	Co^{2+}	Co^{3+}	Co^{4+}	Ru^{4+}	Ru^{5+}
LS	--	$t_{2g}^6e_g^0$ (S=0)	$t_{2g}^5e_g^0$ (S = 1/2)	$t_{2g}^4e_g^0$ (S=1)	$t_{2g}^3e_g^0$ (S=3/2)
IS	--	$t_{2g}^5e_g^1$ (S=1)	--	--	--
HS	$t_{2g}^5e_g^2$ (S=3/2)	$t_{2g}^4e_g^2$ (S=2)	--	--	--

We first briefly discuss the single perovskites phases containing cobalt and ruthenium separately and see the effect of doping non magnetic species on their physical properties. Finally, we discuss the double perovskites which contain both cobalt and ruthenium and their physical properties.

3.1.1 Perovskites containing cobalt

Single perovskite compound $LaCoO_3$ has been extensively studied over the past four decades and is documented in chapter one of the book by P. Gütlich and H.A. Goodwin [3]. Over the years many advancements has been made in understanding of the true magnetic nature of $LaCoO_3$. The recent model which is accepted for $LaCoO_3$ is Co^{3+} has LS state up to 100K. It undergoes spin state transition at around 100-120K and Co^{3+} is converted to IS. Later in the temperature region of 400 to 600K, 50% of Co^{3+} in IS is converted to HS state. Due to this spin state transition, it shows complex magnetic susceptibility curve with non-magnetic ground state and undergoes a transition to paramagnetic state coinciding with spin state transition. Similar spin state transition has also been observed in other rare-earth cobaltates $RECoO_3$. On the contrary, in $YCoO_3$, Co^{3+} remains in the LS configuration and shows the spin state transition at higher temperature of 600K [4]. In $LaCoO_3$ and $YCoO_3$ compounds, insulator-metal transition occurs at around 500 and 750K [4]. Many characterization techniques have been used for probing the spin state transition and related changes in the physical properties in $A^{3+}CoO_3$ compounds [1, 3-5]. By hole doping that is by substitution of Sr^{2+} for La^{3+} in $LaCoO_3$ gives rise to major changes in the physical properties. For lower concentration of doping, ferromagnetic hole rich nano-clusters are formed whereas rest of the bulk phase remains with $LaCoO_3$ character. With the increase in Sr^{2+} substitution leads to slow evolution of ferromagnetic metallic nature. It has been shown that hole doping causes stabilization of IS state in $Co^{3+/4+}$ ion. The extreme end compound $SrCoO_3$ where all the Co is in tetravalent state exhibits ferromagnetic metallic behavior with Tc ~305 K. The Co^{4+} in this compound has been shown to exist in IS state [6]. Interestingly, there exists many oxygen deficient $SrCoO_{3-d}$ intermediate phases with ordered oxygen deficiency and ordered magnetic structures [7, 8]. Brownmillerite phase $SrCoO_{2.5}$ shows high temperature anti-ferromagnetism with T_N~570K [9]. In generality using Goodenough-Kanamori rule [10] it can be inferred that in most cases (for $Co^{2+/3+}$) Co-O-Co 180° super-exchange is AF whereas for Co^{4+} it is FM but this has not been practically experienced in the above examples of cobalt single perovskites. The possible reason is because of the spin state transitions occurring at relatively higher temperatures where samples are in paramagnetic state.

Many double perovskite cobaltates exists with formula $AA'MCoO_6$ where (AA'= Ca, Sr, Ba, La) and (M=non-magnetic cation) [11]. Many of these compounds show anti-ferromagnetic transition. But because of the rock-salt type ordering between Co and M cations, the Co ions form fcc network. Such network is known to have geometric frustration among anti- ferromagnetically coupled species. These double perovskite cobaltates show high frustration factor $f=|\theta|/T_N$ [12, 13] and reduced magnetization. It is argued that lowering of symmetry (monoclinic in most of them) relaxes this frustration partially and the ground state exhibits AFM ordering with appreciable frustration in the background. In particular compounds $A_2Co^{2+}M^{6+}O_6$ (M=Mo, Te, W, Re & A=Ca, Sr, Ba) show cationic ordering between Co^{2+} and M^{6+} and have AF ground state [14] and references therein. The compound $BaLaCo^{2+}SbO_6$ also show cationic ordering and AF ground state [15]. These examples convey that cationic ordering in these DP creates Co^{2+}-O-M-O-Co^{2+} linkage which has AF interaction. But when this periodicity is broken by random distribution of Co and M, like in the case of A_2CoNbO_6, leads to the formation of spin glass or cluster glass phases [16, 17].

3.1.2 Perovskites containing ruthenium

Ruthenium containing perovskites have been receiving considerable attention of late, because of their magnetic nature. $SrRuO_3$ is the only ferromagnetic metal among all the 4d transition elements [18]. The discovery of superconductivity in layered Sr_2RuO_4 phase [19] and of recent cobalt doped Sr_2YRuO_3 [20] has also attracted research on transport properties of ruthenates. The strong spin-orbit coupling in the 4d transition elements compared to the 3d transition elements can also be harvested in magneto-crystalline and magneto-optical properties.

$SrRuO_3$ shows robust ferromagnetism with $T_C \approx 160K$, whereas $CaRuO_3$ do not show any sign of long range magnetic ordering down to 30mK [21]. Both the compounds show metallic property. This fact is still challenging to explain – why the strong ferromagnetic interaction in $SrRuO_3$ between Ru-O-Ru totally collapses in $CaRuO_3$ [22]. Hybridization of Ru t_{2g} and O 2p orbitals form narrow itinerant 4d band and is sensitive to degree of hybridization. It is interpreted that narrow itinerant 4d bandwidth in $CaRuO_3$, (narrower than for $SrRuO_3$), which is too narrow for long-range magnetic ordering, but not so narrow as to cause $CaRuO_3$ to be nonmetallic. $BaRuO_3$ is prepared under high pressure and exists in several polytype. Recently cubic $BaRuO_3$ has been synthesized at 18GPa at 1000°C and shown to have metallic character with ferromagnetic transition at $T_C=60K$ [23] which is much lower as compared to $SrRuO_3$. The exact nature of magnetic correlations in these $ARu^{4+}O_3$ (A=Ca, Sr, Ba) still remains controversial and continues to be investigated. It is difficult to form solid compounds with Ru^{3+} valence state. The most recent report on $La_{0.91}Ru_{0.93}O_3$, where the valence state of Ru is 3.52+, is shown to be paramagnetic down to 2K [24]. The Curie-Weiss temperature for $LaRuO_3$ is negative and high as $\theta \approx -160K$ indicating moderately anti-ferromagnetic interaction but still does not exhibit long range ordering. The single perovskites with pure Ru^{5+} are not reported in literature and as a consequence the nature of 180° super-exchange interaction of Ru^{5+}-O-Ru^{5+} in perovskites in not known. However, in La_3RuO_7 compound there exists one dimensional chain formed by corner sharing of Ru^{5+}O6 octahedra which imitates 180° super-exchange interaction. This compound shows AF transition at 10K [25] and thus supports G-K rule in Ru^{5+}-O-Ru^{5+} interaction. In other cases, interactions other than 180° between Ru^{5+} octahedral also show anti-ferromagnetism [26-30].

There is a long list of double perovskite compounds containing ruthenium along with other magnetic/nonmagnetic ions. Here we confine to the double perovskite phases containing ruthenium as the only magnetic cation. The most popular phase of this kind is Sr_2YRuO_6, which has been continuously studied for almost past four decades [31-34]. Despite this the complete understanding related to this compound remains unclear. As stated above $SrRuO_3$ shows itinerant ferromagnetism, while Sr_2YRuO_6 show uncommon semiconductor behavior with anisotropic conductivity and anti-ferromagnetism with T_N=24K [33, 35]. In Sr_2YRuO_6 compound, Ru^{5+} and Y^{3+} completely orders in rock salt type fashion and thus each RuO6 octahedra are separated by non-magnetic YO6 octahedra. This leads to absence of direct interaction between ruthenium but Ru^{5+} ions form a face-centered-cubic fcc type network. It is well known that anti-ferromagnetic interaction with fcc type network creates magnetic frustration in the system. Despite this Sr_2YRuO_6 shows long range magnetic ordering, where it was shown that next nearest neighbor interactions and/or weak anisotropy stabilizes the AF phase [36]. Similar other double compounds *viz.* $A_2MRu^{5+}O_6$ (A=Ba, Ca and M =La, Y) and $La_2B'Ru^{5+}O_6$ (B'=Li, Na) are shown to have anti-ferromagnetic ordering [31, 32, 37-40]. Thus in general, magnetic interaction between Ru^{5+}-O-M-O-Ru^{5+} is anti-ferromagnetic in nature.

3.1.3 Perovskite phases containing cobalt and ruthenium

Previously we have discussed the perovskites with Co and Ru separately. Clubbing these two cations leads to very rich magnetic phase diagram and thus they provide an opportune system to investigate complex magnetic interactions between high magnetic moments of 3d and itinerancy of 4d. After the discovery of colossal magneto-resistance and half metallic property in Sr_2FeMoO_6 [41], there has been tremendous research on double perovskites for exploring similar properties which have potential applications in spintronic devices. On the similar lines, J. Paul Attfield and co-workers studied $(La_{1+x}Ca_{1-x})CoRuO_6$ and $(La_{1+x}Sr_{1-x})CoRuO_6$ double perovskites [42, 43]. Starting from extreme end x=1, compound La_2CoRuO_6 show partial B-cation ordering with 10% inversion between Co^{2+} and Ru^{4+}. It undergoes anti-ferromagnetic transition at 25K [44]. For x=0 i.e. for $LaMCoRuO_6$ (M=Ca, Sr), there is complete ordering in Co^{2+} and Ru^{5+}. Both the compounds show anti-ferromagnetic transition at 96K for Ca and at 85K for Sr. Whereas for the compounds with composition having x<0 and x>0, there is an increase in the anti-site disorder as the difference between the B-cations decreases following the Anderson's criteria [45] for obtaining a high degree of rock-salt ordering in double perovskites. At other extreme end with x= -1 i.e. for Sr_2CoRuO_6 there is complete disorder between Co^{3+} and Ru^{5+} cations. This compound show spin glass behavior at T_{SG}=95K. We will discuss the compound Sr_2CoRuO_6 and related compounds with more details in the discussion below. The above series set examples to shows that cation ordering plays a crucial role in determining its physical properties. This point was captured in another interesting work carried out by I-Wei Chen and co-workers where magnetic and transport properties was studied on $(Sr_{1-x}La_x)(Ru_{1-x}Co_x)O_3$ system with $(0 \leq x \leq 0.5)$ [46]. Here they dissolved x amount of $LaCoO_3$ into (1-x) amount of stoner ferromagnet (itinerant ferromagnet) $SrRuO_3$. From the XANES studies and variation of the cell volume with 'x' they could show that, with increasing amount of x, Ru^{4+} is converted to Ru^{5+} in the close vicinity of Co by reducing Co^{3+} to Co^{2+}. Weakly diluted sample with x=0.1 shows increased saturation magnetization as compared to the sample with x=0 i.e. pure $SrRuO_3$ and is attributed to polarization of the itinerant electron of $SrRuO_3$ around Co ion. The AC magnetic susceptibility measurements showed that phase with x=0.2 forms cluster glass state while disordered phase with x=0.4 and x=0.5 (which corresponds to $LaSrCoRuO_6$) form in a spin glass state. By using low temperature neutron diffraction the loss of long range magnetic ordering in disordered $LaSrCoRuO_6$ compound was further confirmed by K. R. Priolkar and co-workers [47]. They prepared disordered $LaSrCoRuO_6$ with 20% B-cation inversion by quenching the sample from high temperature. Disordered $LaSrCoRuO_6$ compound shows absence of reflections in the neutron diffraction corresponding to the long range anti-ferromagnetic ordering are suppressed. These observations are attributed to B-cation disorder where Ru-O-Ru interaction now sets in and form ferromagnetic clusters within the sample. This increased ferromagnetic interaction disturbs the anti-ferromagnetic long range ordering and the competing interaction leads to spin glass phase.

Magnetic property of Sr_2CoRuO_6 was first studied by S. H. Kim and P. D. Battle [48]. They showed that Co and Ru are randomly distributed over B-site and the compound show DC magnetic susceptibility nature similar to spin glass type. Similarly Sr_2FeRuO_6 also crystallizes with random distribution of Fe^{3+} and Ru^{5+} and show spin glass behavior at T_{SG}=50K [49]. $Sr_2Co_{1-x}Ru_xO_6$ system show very interesting magnetic phase diagram where end members $SrRuO_3$ and $SrCoO_3$ have ferromagnetic ground state, while all the intermediate compositions studied so far show spin glass type behavior [50, 51]. Even 10 atom % doping of Ru in $SrCoO_3$ i:e with composition $Sr_2Co_{1.8}Ru_{0.2}O_6$ show spin glass behavior [51]. On the contrary, recently studied 2D (thin film) structures of Sr_2CoRuO_6, where Co/Fe and Ru were deliberately ordered, show ferrimagnetic ground state [52].

Similarly thin film study of Sr_2FeRuO_6 also showed high temperature magnetic transition [53]. Interestingly, there are always few exceptions present which break the common notion - the compounds like $Sr_2Cr_xRu_{1-x}O_6$, Sr_2MnRuO_6 and $LaSrMnRuO_6$ lack B-cation ordering but still exhibit long range magnetic ordering [54, 55].

3.2 Issue and plan of work

As discussed above double perovskites containing only Co^{3+} or only Ru^{5+} ions show AF in spite of forming 3D geometrically frustrated fcc network. But even a small amount of inter-mixing in $Sr_2Co_{2-x}Ru_xO_6$ system causes remarkable change in the magnetic ground state. According to G-K rule, 180° super-exchange magnetic interactions between Co^{3+}-O-Co^{3+}, Ru^{5+}-O-Ru^{5+} and Co^{3+}-O-Ru^{5+} are strong anti-ferromagnetic, moderate anti-ferromagnetic and moderate ferromagnetic in nature, respectively. All the bulk compounds reported in the $Sr_2Co_{2-x}Ru_xO_6$ system show absence of cationic ordering. Thus all the three interactions stated above are randomly oriented. For that matter statistically if we consider all the cases of intermediate compounds, it is more likely that there are more AF interacting couples (Co-O-Co and Ru-O-Ru) compared to FM interacting Co-Ru couple. In spite of this, all compounds are reported to be spin glass from magnetic susceptibility studies. It is unclear from the previous work whether the intermediate compounds are true spin glass or co-existing with FM or AF states [50]. In our study we have probed three intermediate phases $Sr_2Co_{2-x}Ru_xO_6$ (x=0.5, 1 & 1.5) using low temperature neutron diffraction. For Sr_2CoRuO_6 compound we have carried out additional experiments to confirm the spin glass state in this compound.

3.3 Synthesis

All the compounds were prepared by solid state reaction. $SrCO_3$, Co_3O_4 and RuO_2 were mixed in required stoichiometric amount and initially heated at 800°C with several intermittent grinding and later heated at 1200°C for 50h in air with several intermittent grinding until pure phase was obtained.

3.4 Results and Discussion

3.4.1 Crystal Structure

Fig. 3.1 shows the Rietveld refinement of XRD data for the $Sr_2Co_{1.5}Ru_{0.5}O_6$, Sr_2CoRuO_6 and $Sr_2Co_{0.5}Ru_{1.5}O_6$ (henceforth referred to as compounds x=0.5, x=1 and x=1.5, respectively). The compounds x=0.5, x=1 and x=1.5 adopt crystal structure with space groups Imma (orthorhombic), I2/c (monoclinic) and Pnma (orthorhombic), respectively. In all the three structures, Co and Ru atoms are randomly distributed over the B-site. It is observed that tolerance factor decreases with lowering of the Co content and consecutively the type of tilting of the octahedral changes from Glazer notation ($a^0b^-b^-$) to ($a^-b^-b^-$) to ($a^+b^-b^-$) accordingly.

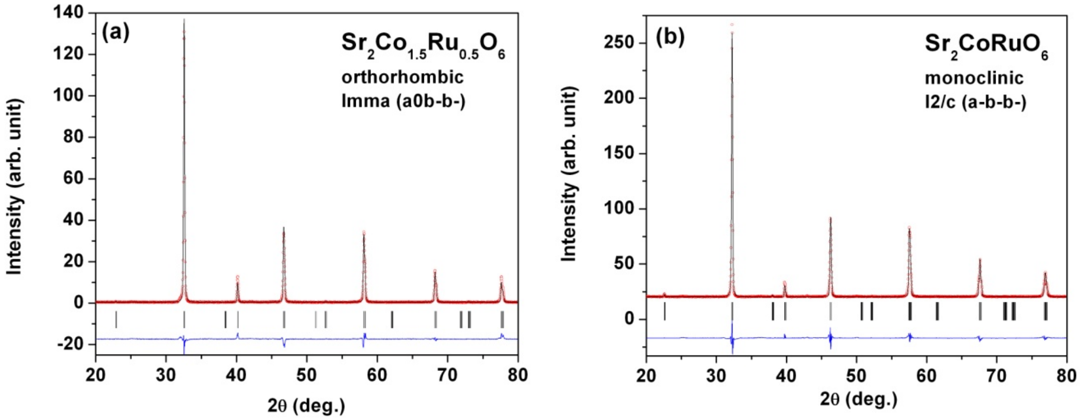

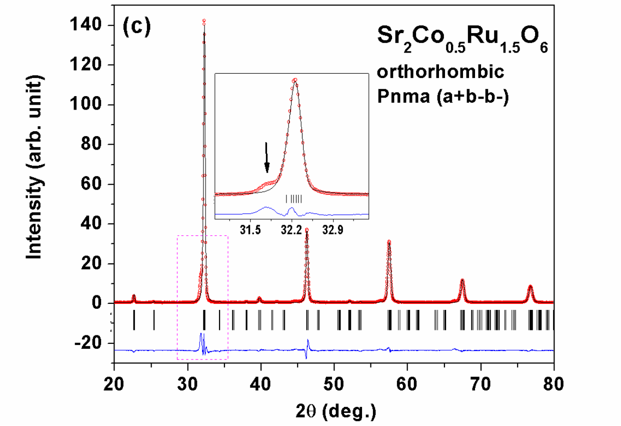

Figure 3.1 *XRD Rietveld refinement plot for a) $Sr_2Co_{1.5}Ru_{0.5}O_6$, b) Sr_2CoRuO_6 and c) $Sr_2Co_{0.5}Ru_{1.5}O_6$. Inset in the graph c, shows the presence of small amount of impurity phase in $Sr_2Co_{0.5}Ru_{1.5}O_6$.*

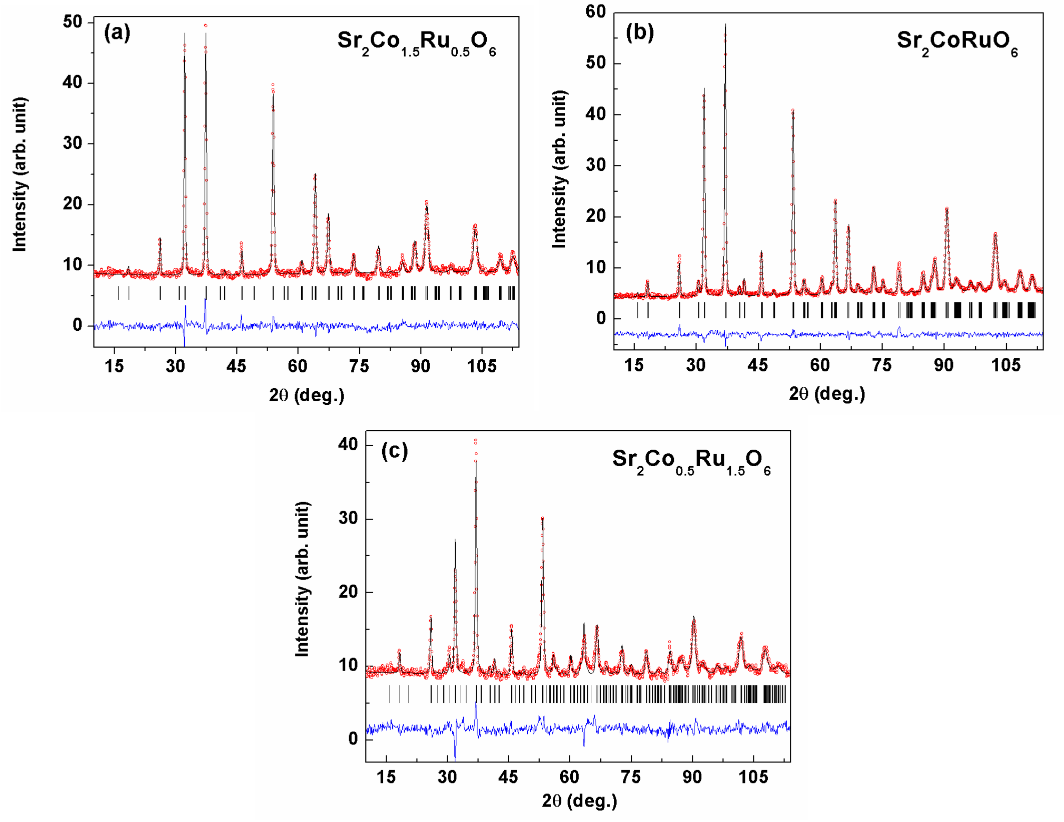

Figure 3.2 *Powder neutron diffraction: Rietveld refinement plot for a) $Sr_2Co_{1.5}Ru_{0.5}O_6$, b) Sr_2CoRuO_6 and c) $Sr_2Co_{0.5}Ru_{1.5}O_6$ at 300K.*

In the crystal structure of Sr_2CoRuO_6; Sr occupies 4e, Co/Ru at 4a and O at 4e and 8f site in the I2/c space group. The refined room temperature cell parameters are a = 5.5272 Å, b = 5.5323 Å, c = 7.8384 Å, β = 90.1998° and these values are comparable to the earlier reports [48]. The crystal structure of Sr_2CoRuO_6 compound was investigated by low temperature powder neutron diffraction (NPD) recorded at various temperatures from 6K to 300K. High temperature XRD (HT-XRD) data was also recorded at from 300K to 1273K. Fig. 3.2 shows the PND Rietveld refinement plot for Sr_2CoRuO_6 at 300K. Similar Rietveld refinement was done on each PND data and HT-XRD data at various temperatures. No structural transition was observed either in X-ray or neutron diffraction studies. However, an anomalous behavior in temperature dependence of the cell parameters is observed below ~300 K as shown in Fig. 3.3 The cell parameters a and b decreases while c increases on lowering of temperature below 300 K.

In Sr_2CoRuO_6 compound, valency of Co and Ru can be either Co^{3+} and Ru^{5+} or Co^{4+} and Ru^{4+}. Considering the redox potentials for Co^{4+}–Co^{3+} and Ru^{5+}–Ru^{4+} couples which have values 1.42 V and 1.07 V, respectively; starting with Co^{4+} and Ru^{4+} couple, the Co^{3+} will act as an oxidizing agent for Ru^{4+} and finally resulting in Co^{3+} and Ru^{5+} couple. Therefore, we infer that Co^{3+} and Ru^{5+} is the more stable configuration than Co^{4+} and Ru^{4+} in this compound. Bond Valence Sum (BVS) calculation was performed using bond distance values derived from room temperature crystal structure model refined using neutron diffraction data. VaList program was used for BVS calculation [56]. All the possible valence states for Co and Ru were tried out for BVS calculation. Best match between oxidation states and BVS values was found to be Co^{3+} and Ru^{5+}. Calculated BVS values were 2.97 and 5.102 for Co^{3+} and Ru^{5+}, respectively. Using high-resolution electron energy loss spectroscopy, A. D. Lozano-Gorrìn et. al. had shown that valency of cobalt is Co^{3+} in Sr_2CoRuO_6 [50]. But spin state of cobalt is not clear from these studies. The anomalous behavior of c-axis below 300K in x=1 compound can be due to the spin state transition in Co^{3+} similar to that observed in $LaCoO_3$ [3] and references therein. Co^{3+} is known to exist in intermediate spin IS and is a Jahn-Teller active ion which causes elongation of octahedra along the c-axis. Due to the random distribution of Co and Ru at octahedral site, it is not possible to check the variation of Co-O bond length individually. Fig. 3.4 shows the variation of the Co/Ru-O bond-lengths below 300K. Bond Co/Ru-O1 increases while Co/Ru-O2 decreases showing octahedral J-T distortion below 300K. As will be discussed later, such anomalous behavior in cell parameters was not observed in other two compounds x=0.5 and x=1.5.

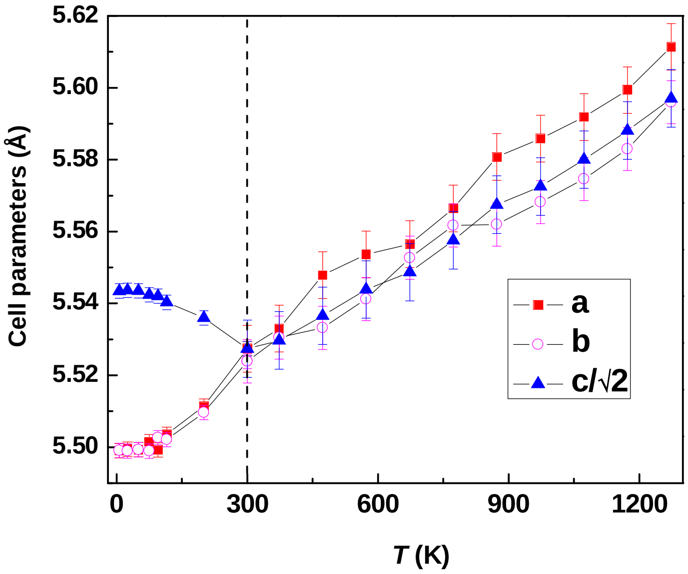

Figure 3.3 *Temperature dependence of cell parameters a, b, c/√2 for* Sr_2CoRuO_6.

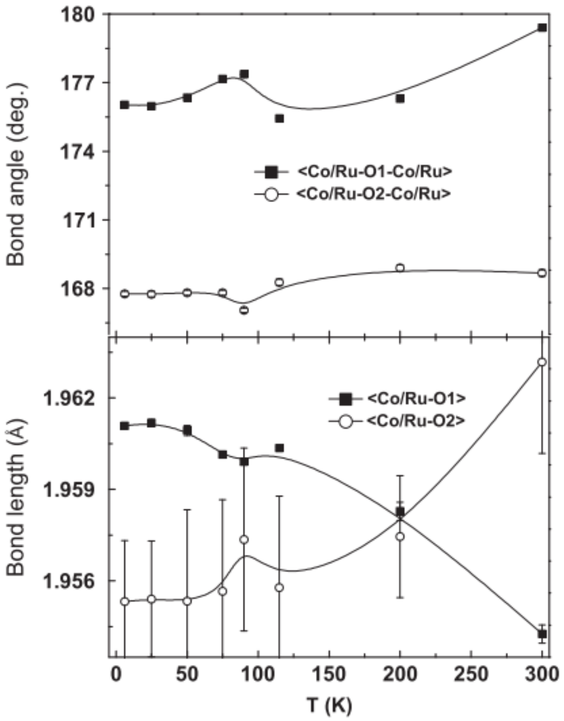

Figure 3.4 *Temperature variations of the bond-lengths and bond-angle in* Sr_2CoRuO_6.

Fig. 3.5 shows temperature dependence of cell volume obtained from high temperature XRD. Average volume thermal expansion co-efficient (α_V) is calculated in the temperature range of 300–1273 K by using

$\alpha_V = (dV/dT)/V_{300K}$.

α_V obtained for Sr_2CoRuO_6 is $41\text{x}10^{-6}$ K^{-1}. The cell volume expansion with temperature was fitted using the Grüneisen approximation

$$V(T) = \frac{\gamma U(T)}{B_0} + V_0 ,$$

where γ is a Grüneisen parameter, B_0 is the bulk modulus and V_0 is the volume at T=0 K. The internal energy, U(T) in the Debye approximation is described as

$$U(T) = 9Nk_BT\left(\frac{T}{\theta_D}\right)^3\int_0^{\frac{\theta_D}{T}}\frac{x^3}{e^x-1}dx ,$$

where N is number of atoms per unit cell, kB is Boltzmann's constant, θ_D is Debye temperature. The fitted parameters are V_0, γ/B_0, and θ_D. The obtained value of θ_D =539 K is close to that reported in other similar samples [57]. These parameters obtained from the high temperature fit also describes the temperature dependence of cell volume at low temperatures and is shown in the inset of Fig. 3.5

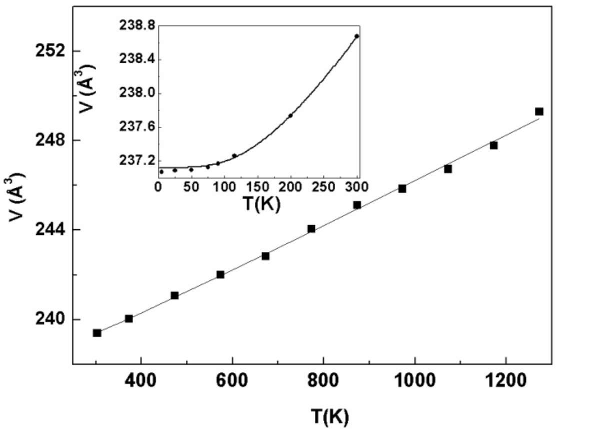

Figure 3.5 *Temperature dependence of cell volume for Sr_2CoRuO_6 and the solid lines show the data fitted using Grüneisen approximation.*

Fig. 3.6 shows the temperature variation of cell parameters and cell volume for $Sr_2Co_{1.5}Ru_{0.5}O_6$ and $Sr_2Co_{0.5}Ru_{1.5}O_6$. In this case anomalous behavior in the temperature variation of cell parameters as observed in the case of Sr_2CoRuO_6 is not observed. The Debye temperature obtained using Grüneisen approximation for x=0.5 and x=1.5 are 454K and 290K, respectively.

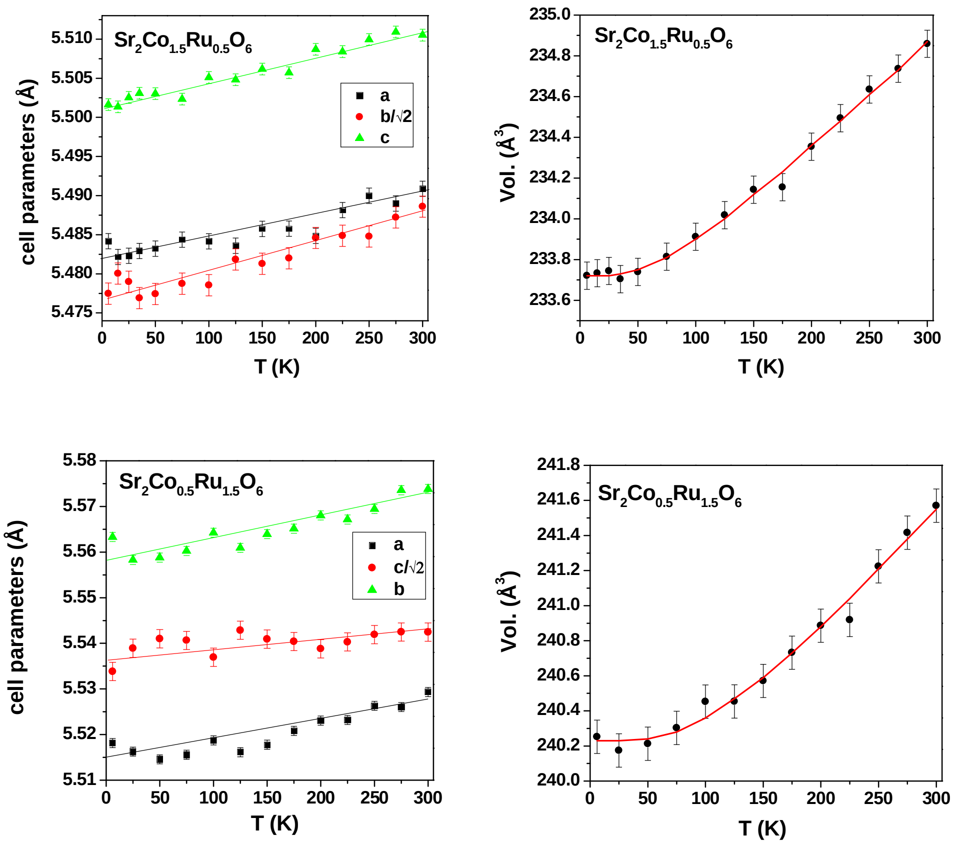

Figure 3.6 *Temperature variations of cell parameters and cell volume for $Sr_2Co_{1.5}Ru_{0.5}O_6$ and $Sr_2Co_{0.5}Ru_{1.5}O_6$. The solid lines show the data fitted using Grüneisen approximation.*

3.4.2 DC Magnetization study

Fig. 3.7 shows the DC magnetic susceptibility data for all the three compounds. For x=1 compound, on lowering of temperature a cusp in M(T) is observed at 95 K. Together with it a bifurcation of the zero-field cooled (ZFC) and field-cooled (FC) data is observed below this temperature as reported earlier in this sample [48]. This observation has been attributed to spin glass behavior. Significant deviation from the true paramagnetic character is observed immediately in the vicinity of transition temperature, T~95 K and a Curie–Weiss (C-W) fit to the M/H data could be carried out only in the temperature range of 200–300 K and is shown in the inset. The effective magnetic moment (μ_{eff}) and Curie-Weiss temperature (θ_C) obtained are 4.82 μ_B and −83 K, respectively. This observation has been attributed to spin glass behavior.

Table 3.2 Crystal structure parameters for $Sr_2Co_{1.5}Ru_{0.5}O_6$, Sr_2CoRuO_6 and $Sr_2Co_{0.5}Ru_{1.5}O_6$ compounds at 300K.

$Sr_2Co_{1.5}Ru_{0.5}O_6$					
System: Orthorhombic, space group: Imma, Z=2					
a = 5.4979(5)Å, b = 7.7658(3)Å, c = 5.4960(5)Å, V = 234.66(3)Å^3					
Atom	**Site**	**x**	**y**	**z**	**Occupancy**
Sr	4e	0	0.25	0.502(9)	1
Co/Ru	4a	0	0	0	0.75/0.25
O1	4e	0	0.25	0.01(7)	1
O2	8g	0.25	0.50(1)	0.25	1
Sr_2CoRuO_6					
System: Monoclinic, space group: I2/c, Z=2					
a = 5.5272(6)Å, b = 5.5323(6)Å, c = 7.8384(3)Å, β = 90.1998(4)°, V = 239.68(4)Å^3					
Sr	4e	0	0.499(3)	0.25	1
Co/Ru	4a	0	0	0	0.5/0.5
O1	4e	0	0.005(8)	0.25	1
O2	8f	0.266(8)	0.771(5)	0.016(3)	1
$Sr_2Co_{0.5}Ru_{1.5}O_6$					
System: Orthorhombic, space group: Pnma, Z=2					
a = 5.5432(5)Å, b = 7.8441(3)Å, c = 5.5695(5)Å, V = 242.17(3)Å^3					
Sr	4c	0.479(3)	0.25	0.009(3)	1
Co/Ru	4a	0	0	0	0.25/0.75
O1	4c	0.502(3)	0.25	0.546(3)	1
O2	8d	0.237(3)	0.019(1)	0.267(2)	1

Significant deviation from the true paramagnetic character is observed immediately in the vicinity of transition temperature, T~95 K and a Curie–Weiss (C-W) fit to the M/H data could be carried out only in the temperature range of 200–300 K and is shown in the inset. The effective magnetic moment (μ_{eff}) and Curie-Weiss temperature (θ_C) obtained are 4.82 μ_B and −83 K, respectively. The negative value of Curie-Weiss temperature ($\theta_C \approx -83$ K) indicates anti-ferromagnetic interaction. Considering Co^{3+} with HS (S=2) and Ru^{5+} with LS

(S=3/2), the calculated spin only moment μ_{eff}=4.42 μ_B. The deviation of observed μ_{eff} value from the calculated value may be due to limited data available for C-W fit in the temperature 200 to 300K. A. D. Lozano-Gorrín et al. observed μ_{eff}=4.14 μ_B for Sr_2CoRuO_6 from the high temperature magnetic susceptibility data which is close to calculated value [50]. But with these results true spin state of Co^{3+} ion in the temperature below 300K is not clear for Sr_2CoRuO_6. The anomalous increase of c-axis below 300K which is indicative of Jahn-Teller distortion in IS state of Co^{3+} needs to be verified.

The compound $Sr_2Co_{1.5}Ru_{0.5}O_6$ also shows a cusp in M(T) at 100 K and the bifurcation of ZFC and FC below 150K. The cusp at 100K is attributed to spin glass transition similar to Sr_2CoRuO_6 compound. It is commonly observed that the compounds which contains Sr and Ru, is contaminated with ferromagnetic impurity phase of $SrRuO_3$ and cause the bifurcation of ZFC and FC below its TC=150K. Though impurity phase $SrRuO_3$ is not observed in our XRD, we still observe its presence in the magnetization data. The field dependent magnetization M(H) loop done at 3K is linear and unsaturated up to 9 Tesla. It shows very small hysteresis due to $SrRuO_3$ impurity.

The compound $Sr_2Co_{0.5}Ru_{1.5}O_6$ is ruthenium rich and contains higher $SrRuO_3$ impurity. Very weak reflections as a shoulder to main peaks corresponding to $SrRuO_3$ are observed in the XRD. Due to this there is a huge rise in the FC susceptibility below 150K temperature and the weak spin glass transition at lower temperature is unseen. But this spin glass transition was clearly observed by A. D. Lozano-Gorrín et al [50]. The field dependent magnetization recorded at 310K does not show any hysteresis, whereas magnetization recorded at 3K shows the hysteresis due to $SrRuO_3$ impurity. The broad hysteresis in $Sr_2Co_{0.5}Ru_{1.5}O_6$ as compared to $Sr_2Co_{1.5}Ru_{0.5}O_6$ shows the increased amount of $SrRuO_3$ impurity in x=1.5 compound.

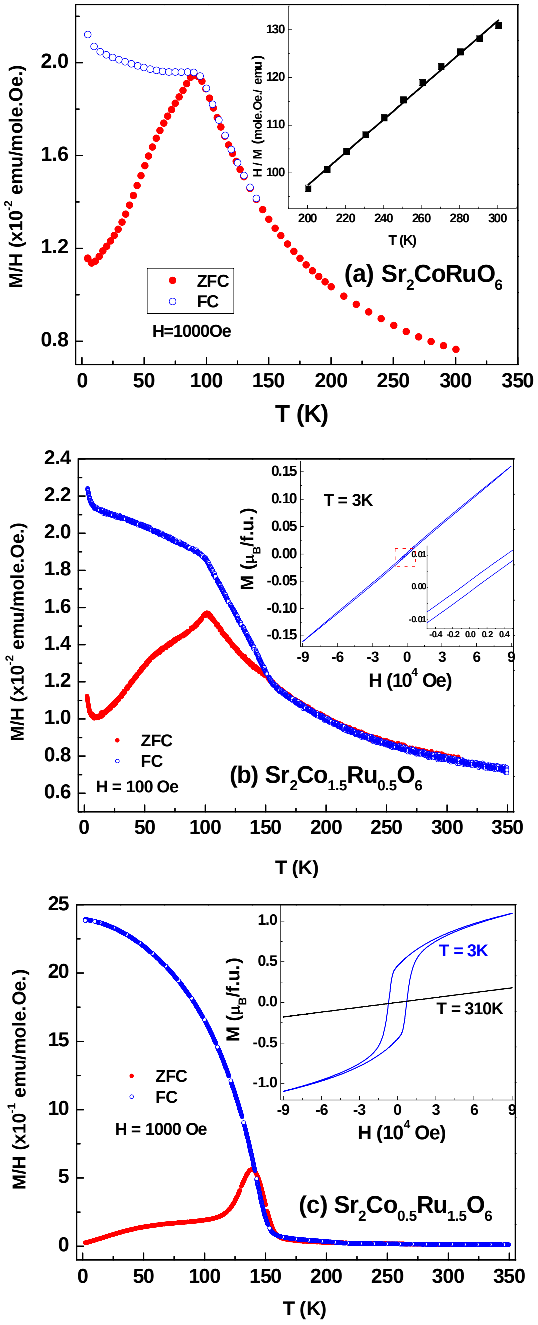

Figure 3.7 *Temperature dependent DC magnetic susceptibility (ZFC and FC) for the three compounds. The inset in the graph a) shows variation of inverse susceptibility with temperature and fit to the Curie–Weiss behavior for* Sr_2CoRuO_6. *The inset in the graphs b) & c) shows field dependent magnetization for other two compounds at indicated temperatures.*

3.4.3 AC Magnetization study and thermo remnant magnetization

Further investigation was done on Sr_2CoRuO_6 compound which shows the spin glass type transition below 95K. The ac magnetic susceptibility measurements were carried out at 13, 130 and 1000 Hz. Fig. 3.8 shows the real part of ac susceptibility, $\chi'(T)$, recorded at 13 Hz with 1 Oe magnetic field. A cusp at the same temperature as seen in the DC magnetization curve is observed. The position of the cusp (T_f) exhibits frequency dependence and is shown in Fig. 3.8(a). T_f shifts to higher temperatures with increase in frequency which is characteristic feature of a spin or cluster glass state [58]. A difference in freezing temperature of 2.84 K is observed between 13 Hz and 1 kHz. An estimate of the relative shift of the freezing temperature, T_f as a function of frequency is given as $K = \Delta T_f/(T_f \Delta \log f)$. The value obtained for K is 0.01. In manganites this value is found to vary between 0.03 and 0.1 [51, 59]. We also observe time dependent phenomena of the thermo remnant magnetization, MTRM. For this experiment, the sample was cooled in zero field from 300 K down to 2 K. It

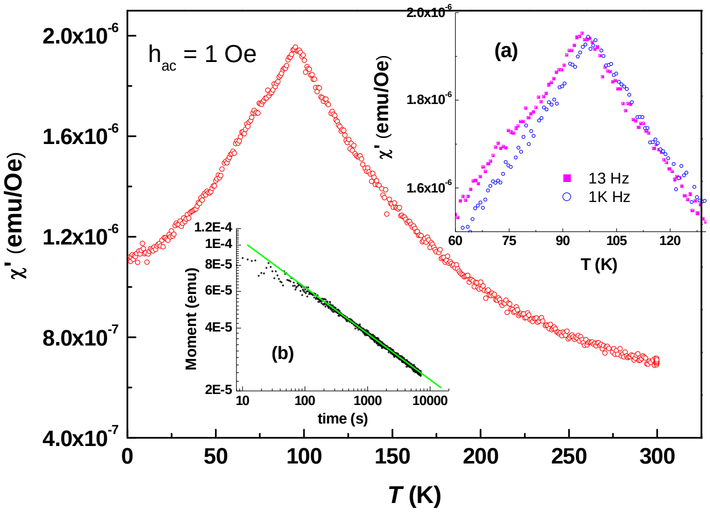

Figure 3.8 *Temperature dependence of the real part of AC magnetic susceptibility data recorded at 13 Hz. (Inset a) AC magnetic susceptibility at 13 and 1 K Hz. (Inset b) Isothermal time dependent magnetization measured at 80 K.*

was then heated to 80 K. At this temperature a magnetic field of 5 T was applied and the field was switched off. The magnetization was then recorded as a function of time. In Fig. 3.8(b) is shown log–log plot of MTRM versus time. The linear behavior indicates that MTRM decays following a power law, $M = At^{-\alpha}$. This power law behavior is found to better describe the decay of MTRM over an extended time scale in classical spin glasses [58].

3.4.4 Low temperature neutron diffraction and neutron depolarization measurements

Neutron diffraction measurement was carried out on Sr_2CoRuO_6 compound at several temperatures below 300 K. Fig. 3.9 shows a section of the neutron diffraction patterns at 6 K and 115 K. It is observed that there are no super-lattice reflections or enhancement in the intensity of the low angle fundamental reflections on lowering of temperature. This indicates that there is no long range magnetic ordering, either ferromagnetic or anti-ferromagnetic, in this sample. To further rule out the possibility of ferromagnetic ordering we have carried out neutron depolarization measurements (shown in the inset of Fig. 3.9). The transmitted beam polarization does not undergo any change below 95K confirming the absence of ferromagnetic correlations in the sample [60] and references there in. Similar results were obtained for the other two compounds indicating that all the three intermediate compounds show absence of long range magnetic ordering and show spin glass behavior.

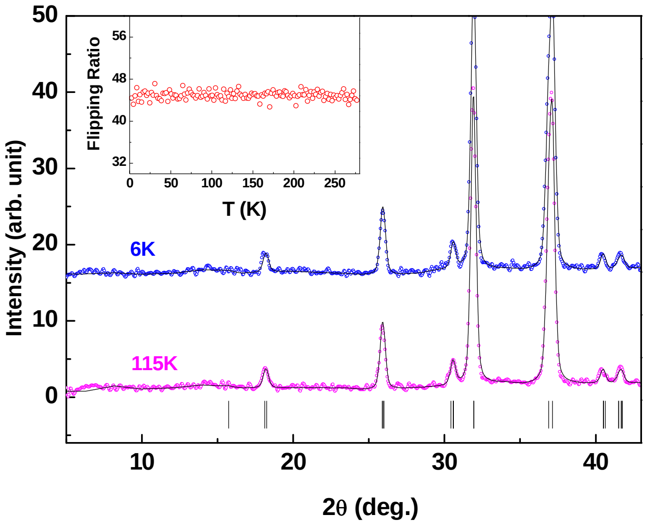

Figure 3.9 *A section of the neutron diffraction pattern at 6 K and 115 K. (Inset) Temperature dependence of flipping ratio obtained using neutron depolarization experiment.*

3.4.5 Dielectric measurements

The ac dielectric study was carried out from 6K to 300K in the frequency range of 1Hz to 1MHz using a frequency response analyzer. Fig. 3.10 shows the temperature dependence of the real part of dielectric constant ε'. It shows typical frequency dependent dielectric relaxation in the temperature region of 50K to 150K. Loss tangent also shows a frequency dependent hump in the same temperature region. In both the curves, peak temperature where the maximum occurs shifts to the higher temperature with increase in frequency. This is characteristic property of dielectric relaxor. The sharp increase in the tangent loss shows increase in the dc conductivity and is in agreement with the semiconductor like conductivity [61]. Semiconductor like conductivity restricts the investigation in the higher temperature region. The frequency dependent dielectric data at different temperatures is shown in the fig. 3.10.

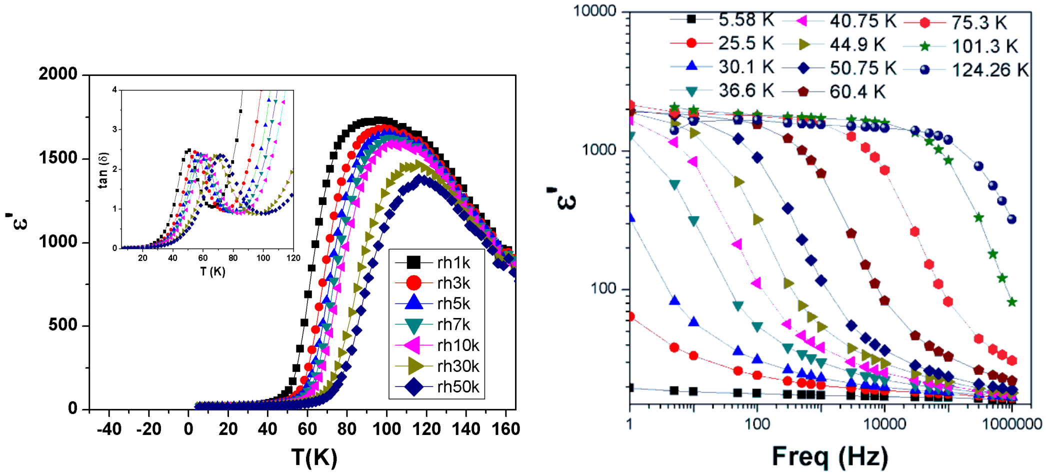

Figure 3.10 *Temperature dependence of dielectric constant ε' and loss tangent at selected frequencies. Frequency dependence of dielectric constant ε' at selected temperatures.*

This data were fitted using Cole-Cole model [62] given as

$$\varepsilon' = \varepsilon^{\infty} + \frac{\varepsilon_S - \varepsilon_\infty}{1+(i\omega\tau)^{1-\alpha}} ,$$

where ε_∞ and ε_S are the relative permittivity at high and low frequency respectively, $\omega = 2\pi f$, τ is relaxation time and α is a distribution of relaxation time with values between 0 to 1. The fitted values of relaxation time showed the thermal dependence of Arrhenius type given by the equation $\tau = \tau_0 \exp(E_a/k_B T)$, where, τ_0 is a constant and E_a is the activation energy. The fitting parameters obtained are E_a=0.05eV and τ_0=1.98E-8. The value of activation energy is much smaller in comparison to typical ferroelectric and dielectric compound like $Pb(Zr_{0.2}Ti_{0.8})O_3$ with E_a=0.9eV. Interestingly, the dielectric relaxor and spin glass transition is observed at same temperature (95K). Temperature dependence of bond length and angle (Fig. 3.4) shows that the bond length along the axis increases while the planar one decreases with temperature. An anomaly in both bond length and angle coincides with the magnetic transition temperature which is the evidence of weak magneto-elastic coupling. Such coupling may be linked with the observed relaxor behavior.

3.5 Conclusion

In this chapter, we have studied the crystal structure and magnetic properties of $Sr_2Co_{2-x}Ru_xO_6$ (x=0.5, 1, 1.5) compounds. All the three compounds have random distribution of Co and Ru cations at octahedral B-site. As the tolerance factor decreases with lowering of the Co content, the type of tilting of the octahedral changes from Glazer notation ($a^0b^-b^-$) to ($a^-b^-b^-$) to ($a^+b^-b^-$) with the space group Imma (orthorhombic), I2/c (monoclinic) and Pnma (orthorhombic), respectively. The low temperature NPD and high temperature XRD measurements shows that in Sr_2CoRuO_6 compound, c-axis undergoes anomalous negative thermal expansion below 300K which is possibly due to the spin state transition of Co^{3+} from HS to IS. Such behavior is absent in the other two studied compounds. Using various techniques we confirm that all the intermediate compounds show absence of long range magnetic ordering and undergo spin glass type transition at ~100K. The random distribution of Co and Ru cations in the intermediate compounds causes competing FM and AFM interaction leading to frustrated magnetic system. Thus it is interesting to observe that magnetic phase diagram of $Sr_2Co_{2-x}Ru_xO_6$ system is dominated by a spin glass intermediate compounds while end members $SrCoO_3$ and $SrRuO_3$ being ferromagnetic in nature. The dielectric measurement shows relaxor dielectric behavior for Sr_2CoRuO_6 compound in the same temperature region where it undergoes spin glass. The random distribution of Co^{3+} and Ru^{5+} ions causes formation of nano-polar regions. The anomalous behavior of bond parameters at 95K, indicate magneto-elastic coupling, which may be the reason for the identical relaxor and spin glass transition temperature.

3.6 References

[1] B. Raveau, M. Seikh, Cobalt Oxides: From Crystal Chemistry to Physics, Wiley (2012).
[2] R.J. Cava, Schizophrenic electrons in ruthenium-based oxides, Dalton Transactions, (2004), p. 2979.

[3] P. Gütlich, H.A. Goodwin, Spin Crossover in Transition Metal Compounds II, Topics in Current Chemistry, Springer-Verlag Berlin Heidelberg, **2004**.

[4] K. Knížek, Z. Jirák, J. Hejtmánek, M. Veverka, M. Maryško, B.C. Hauback, H. Fjellvåg, Structure and physical properties of $YCoO_3$ at temperatures up to 1000K, Physical Review B, **73,** (2006), p. 214443.

[5] K. Knížek, J. Hejtmánek, Z. Jirák, P. Tomeš, P. Henry, G. André, Neutron diffraction and heat capacity studies of $PrCoO_3$ and $NdCoO_3$, Physical Review B, **79,** (2009), p. 134103.

[6] L. Youwen, K. Yoshio, I. Shintaro, T. Yasujiro, T. Yoshinori, Synthesis of cubic $SrCoO_3$ single crystal and its anisotropic magnetic and transport properties, Journal of Physics: Condensed Matter, **23,** (2011), p. 245601.

[7] R. Le Toquin, W. Paulus, A. Cousson, C. Prestipino, C. Lamberti, Time-Resolved in Situ Studies of Oxygen Intercalation into $SrCoO_{2.5}$, Performed by Neutron Diffraction and X-ray Absorption Spectroscopy, Journal of the American Chemical Society, **128,** (2006), p. 13161.

[8] C.K. Xie, Y.F. Nie, B.O. Wells, J.I. Budnick, W.A. Hines, B. Dabrowski, Magnetic phase separation in $SrCoO_x$ ($2.5 \leq x \leq 3$), Applied Physics Letters, **99,** (2011), p. 052503.

[9] T. Takeda, Y. Yamaguchi, H. Watanabe, Magnetic Structure of $SrCoO_{2.5}$, Journal of the Physical Society of Japan, **33,** (1972), p. 970.

[10] J.B. Goodenough, Magnetism and the chemical bond, Interscience Publishers (1963).

[11] S. Vasala, M. Karppinen, $A2B'B''O_6$ perovskites: A review, Progress in Solid State Chemistry, **43,** (2015), p. 1.

[12] J.-W.G. Bos, J.P. Attfield, Magnetic frustration in $(LaA)CoNbO_6$ (A = Ca, Sr, and Ba) double perovskites, Physical Review B, **70,** (2004), p. 174434.

[13] J.E. Greedan, Geometrically frustrated magnetic materials, Journal of Materials Chemistry, **11,** (2001), p. 37.

[14] R. Mathieu, S.A. Ivanov, R. Tellgren, P. Nordblad, Influence of the A cation on the low-temperature antiferromagnetism of ordered antiferroelectric A_2CoTeO_6 perovskites, Physical Review B, **83,** (2011), p. 174420.

[15] M. Cecilia Blanco, J.M. De Paoli, S. Ceppi, G. Tirao, V.M. Nassif, J. Guimpel, R.E. Carbonio, Synthesis, structural characterization and magnetic properties of the monoclinic ordered double perovskites $BaLaMSbO_6$, with M = Mn, Co and Ni, Journal of Alloys and Compounds, **606,** (2014), p. 139.

[16] K. Yoshii, Structural and magnetic properties of the perovskites $Sr_{n+1}(Co_{0.5}Nb_{0.5})_nO_{3n+1}$ (n=∞, 2 and 1), Journal of Alloys and Compounds, **307,** (2000), p. 119.

[17] K. Yoshii, Magnetic Transition in the Perovskite Ba_2CoNbO_6, Journal of Solid State Chemistry, **151,** (2000), p. 294.

[18] J.M. Longo, P.M. Raccah, J.B. Goodenough, Magnetic Properties of $SrRuO_3$ and $CaRuO_3$, Journal of Applied Physics, **39,** (1968), p. 1327.

[19] Y. Maeno, H. Hashimoto, K. Yoshida, S. Nishizaki, T. Fujita, J.G. Bednorz, F. Lichtenberg, Superconductivity in a layered perovskite without copper, Nature, **372,** (1994), p. 532.

[20] M.K. Wu, D.Y. Chen, F.Z. Chien, S.R. Sheen, D.C. Ling, C.Y. Tai, G.Y. Tseng, D.H. Chen, F.C. Zhang, Anomalous magnetic and superconducting properties in a Ru-based double perovskite, Zeitschrift für Physik B Condensed Matter, **102,** (1996), p. 37.

[21] T.C. Gibb, R. Greatrex, N.N. Greenwood, P. Kaspi, Ruthenium-99 Mossbauer studies of the magnetic properties of ternary and quaternary ruthenium(IV) oxides, Journal of the Chemical Society, Dalton Transactions, (1973), p. 1253.

[22] S. Kim, R.I. Dass, J.B. Goodenough, Interatomic versus intraatomic Ru interactions in perovskites, Journal of Solid State Chemistry, **181,** (2008), p. 2989.

[23] C.-Q. Jin, J.-S. Zhou, J.B. Goodenough, Q.Q. Liu, J.G. Zhao, L.X. Yang, Y. Yu, R.C. Yu, T. Katsura, A. Shatskiy, E. Ito, High-pressure synthesis of the cubic perovskite $BaRuO_3$ and evolution of ferromagnetism in $ARuO_3$ (A = Ca, Sr, Ba) ruthenates, Proceedings of the National Academy of Sciences, **105,** (2008), p. 7115.

[24] A. Sinclair, J.A. Rodgers, C.V. Topping, M. Míšek, R.D. Stewart, W. Kockelmann, J.-W.G. Bos, J.P. Attfield, Synthesis and Properties of Lanthanide Ruthenium(III) Oxide Perovskites, Angewandte Chemie International Edition, **53,** (2014), p. 8343.

[25] R. Lam, F. Wiss, J.E. Greedan, Magnetic Properties of the Fluorite-Related La_3MO_7 Phases, M=Ru and Os, Journal of Solid State Chemistry, **167,** (2002), p. 182.

[26] M. Soma, H. Sato, Lithium Ruthenates: Controlling Dimensionality and Topology of Magnetic-Ion Arrangements, Journal of the Physical Society of Japan, **75,** (2006), p. 124802.

[27] K.A. Regan, Q. Huang, R.J. Cava, Isolated spin 3/2 plaquettes in Na_3RuO_4, Journal of Solid State Chemistry, **178,** (2005), p. 2104.

[28] P. Manuel, D.T. Adroja, P.-A. Lindgard, A.D. Hillier, P.D. Battle, W.-J. Son, M.-H. Whangbo, Neutron scattering and μSR investigations of quasi-one-dimensional magnetism in the spin =3/2 compound Li_3RuO_4, Physical Review B, **84,** (2011), p. 174430.

[29] P. Khalifah, D.M. Ho, Q. Huang, R.J. Cava, The Structure and Properties of β-La_3RuO_7: A New Structure Type with Isolated RuO_6 Octahedra, Journal of Solid State Chemistry, **165,** (2002), p. 359.

[30] W. Tian, C. Svoboda, M. Ochi, M. Matsuda, H.B. Cao, J.G. Cheng, B.C. Sales, D.G. Mandrus, R. Arita, N. Trivedi, J.Q. Yan, High antiferromagnetic transition temperature of the honeycomb compound $SrRu_2O_6$, Physical Review B, **92,** (2015), p. 100404.

[31] R. Greatrex, N.N. Greenwood, M. Lal, I. Fernandez, A study of the ruthenium(V) perovskites M_2LnRuO_6 (M = Ca, Ln = Y, La, or Eu; M = Sr, Ln = Y; M = Ba, Ln = La or Eu) by ^{99}Ru Mössbauer spectroscopy and other techniques, Journal of Solid State Chemistry, **30,** (1979), p. 137.

[32] P.D. Battle, W.J. Macklin, The crystal and magnetic structures of Ca_2YRuO_6 and the electronic properties of the series $M_{2+2X}^{3+}Ru^{5+}O_6$ (M = Ca, Sr, Ba; X = La, Y), Journal of Solid State Chemistry, **54,** (1984), p. 245.

[33] G. Cao, Y. Xin, C.S. Alexander, J.E. Crow, Weak ferromagnetism and spin-charge coupling in single-crystal Sr_2YRuO_6, Physical Review B, **63,** (2001), p. 184432.

[34] S.M. Disseler, J.W. Lynn, R.F. Jardim, M.S. Torikachvili, E. Granado, Spin dynamics and two-dimensional correlations in the fcc antiferromagnetic Sr_2YRuO_6, Physical Review B - Condensed Matter and Materials Physics, **93,** (2016), p.

[35] E. Granado, J.W. Lynn, R.F. Jardim, M.S. Torikachvili, Two-Dimensional Magnetic Correlations and Partial Long-Range Order in Geometrically Frustrated Sr_2YRuO_6, Physical Review Letters, **110,** (2013), p. 017202.

[36] E.V. Kuz'min, S.G. Ovchinnikov, D.J. Singh, Effect of frustrations on magnetism in the Ru double perovskite Sr_2YRuO_6, Physical Review B, **68,** (2003), p. 024409.

[37] P.D. Battle, J.B. Goodenough, R. Price, The crystal structures and magnetic properties of Ba_2LaRuO_6 and Ca_2LaRuO_6, Journal of Solid State Chemistry, **46,** (1983), p. 234.

[38] P.D. Battle, C.W. Jones, The crystal and magnetic structures of Sr_2LuRuO_6, Ba_2YRuO_6, and Ba_2LuRuO_6, Journal of Solid State Chemistry, **78,** (1989), p. 108.

[39] P.D. Battle, C.P. Grey, M. Hervieu, C. Martin, C.A. Moore, Y. Paik, Structural chemistry and magnetic properties of La_2LiRuO_6, Journal of Solid State Chemistry, **175,** (2003), p. 20.

[40] A.A. Aczel, D.E. Bugaris, L. Li, J.Q. Yan, C. de la Cruz, H.C. zur Loye, S.E. Nagler, Frustration by competing interactions in the highly distorted double perovskites $La_2NaB'O_6$ (B′=Ru, Os), Physical Review B, **87,** (2013), p. 014435.

[41] K.I. Kobayashi, T. Kimura, H. Sawada, K. Terakura, Y. Tokura, Room-temperature magnetoresistance in an oxide material with an ordered double-perovskite structure, Nature, **395,** (1998), p. 677.

[42] J.-W.G. Bos, J.P. Attfield, Control of antisite disorder, magnetism, and asymmetric doping effects in $(La_{1+x}Ca_{1-x})CoRuO_6$ double perovskites, Physical Review B, **69,** (2004), p. 094434.

[43] J.-W.G. Bos, J.P. Attfield, Structural, Magnetic, and Transport Properties of $(La_{1+x}Sr_{1-x})CoRuO_6$ Double Perovskites, Chemistry of Materials, **16,** (2004), p. 1822.

[44] J.-W.G. Bos, J.P. Attfield, Crystal and magnetic structures of the double perovskite La_2CoRuO_6, Journal of Materials Chemistry, **15,** (2005), p. 715.

[45] M.T. Anderson, K.B. Greenwood, G.A. Taylor, K.R. Poeppelmeier, B-cation arrangements in double perovskites, Progress in Solid State Chemistry, **22,** (1993), p. 197.

[46] A. Mamchik, W. Dmowski, T. Egami, I.W. Chen, Magnetic impurities in conducting oxides. II. $(Sr_{1-x}La_x)(Ru_{1-x}Fe_x)O_3$ system, Physical Review B, **70,** (2004), p. 104410.

[47] P.S.R. Murthy, K.R. Priolkar, P.A. Bhobe, A. Das, P.R. Sarode, A.K. Nigam, Structure, transport and magnetic properties in $La_{2x}Sr_{2-2x}Co_{2x}Ru_{2-2x}O_6$, Journal of Magnetism and Magnetic Materials, **323,** (2011), p. 822.

[48] S.H. Kim, P.D. Battle, Structural and Electronic Properties of the Mixed Co/Ru Perovskites AA′ $CoRuO_6$ (A, A′ = Sr, Ba, La), Journal of Solid State Chemistry, **114,** (1995), p. 174.

[49] P.D. Battle, T.C. Gibb, C.W. Jones, F. Studer, Spin-glass behavior in Sr_2FeRuO_6 and $BaLaNiRuO_6$: A comparison with antiferromagnetic $BaLaZnRuO_6$, Journal of Solid State Chemistry, **78,** (1989), p. 281.

[50] A.D. Lozano-Gorrín, J.E. Greedan, P. Núñez, C. González-Silgo, G.A. Botton, G. Radtke, Structural characterization, magnetic behavior and high-resolution EELS study of new perovskites $Sr_2Ru_{2-x}Co_xO_{6-\delta}$ ($0.5 \leq x \leq 1.5$), Journal of Solid State Chemistry, **180,** (2007), p. 1209.

[51] T. Motohashi, V. Caignaert, V. Pralong, M. Hervieu, A. Maignan, B. Raveau, Competition between ferromagnetism and spin glass: The key for large magnetoresistance in oxygen-deficient perovskites $SrCo_{1-x}M_xO_{3-\delta}$ (M=Nb,Ru), Physical Review B, **71,** (2005), p. 214424.

[52] K. Watarai, K. Yoshimatsu, K. Horiba, H. Kumigashira, O. Sakata, A. Ohtomo, Epitaxial synthesis and physical properties of double-perovskite oxide Sr_2CoRuO_6 thin films, Journal of Physics: Condensed Matter, **28,** (2016), p. 436005.

[53] J. Chang, K. Lee, M.H. Jung, J.H. Kwon, M. Kim, S.K. Kim, Emergence of room-temperature magnetic ordering in artificially fabricated ordered-double-Perovskite Sr_2FeRuO_6, Chemistry of Materials, **23,** (2011), p. 2693.

[54] A.J. Williams, A. Gillies, J.P. Attfield, G. Heymann, H. Huppertz, M.J. Martínez-Lope, J.A. Alonso, Charge transfer and antiferromagnetic insulator phase in $SrRu_{1-x}Cr_xO_3$ perovskites: Solid solutions between two itinerant electron oxides, Physical Review B, **73,** (2006), p. 104409.

[55] P.M. Woodward, J. Goldberger, M.W. Stoltzfus, H.W. Eng, R.A. Ricciardo, P.N. Santhosh, P. Karen, A.R. Moodenbaugh, Electronic, Magnetic, and Structural Properties of Sr_2MnRuO_6 and $LaSrMnRuO_6$ Double Perovskites, Journal of the American Ceramic Society, **91,** (2008), p. 1796.

[56] A.S. Wills, VaList. Program available from www.ccp14.ac.uk

[57] M.R. Ibarra, P.A. Algarabel, C. Marquina, J. Blasco, J. García, Large magnetovolume effect in yttrium doped La-Ca-Mn-O perovskite, Physical Review Letters, **75,** (1995), p. 3541.

[58] K. Binder, A.P. Young, Spin glasses: Experimental facts, theoretical concepts, and open questions, Reviews of Modern Physics, **58,** (1986), p. 801.

[59] J.A. Mydosh, Spin Glasses: An Experimental Introduction, Taylor & Francis (1993).

[60] A. Das, S.K. Paranjpe, S. Honda, S. Murayama, Y. Tsuchiya, Neutron depolarization measurements on the reentrant spin-glass bcc Cr-Fe-Mn alloy, Journal of Physics: Condensed Matter, **11,** (1999), p. 5209.

[61] R. Phatak, K. Krishnan, S.K. Sali, A. Das, A.K. Nigam, Structure and magnetic properties of Sr_2CoRuO_6, Journal of Magnetism and Magnetic Materials, **344,** (2013), p. 129.

[62] K.S. Cole, R.H. Cole, Dispersion and Absorption in Dielectrics I. Alternating Current Characteristics, The Journal of Chemical Physics, **9,** (1941), p. 341.

Chapter 4.

Crystal structure and site symmetry studies on BaLaMM'O_6 compounds (M = alkali/alkaline earth metal, M'= Nb, Sb, Te).

4.1 Introduction

AA'BB'O_6 is a variant of double perovskite $A_2BB'O_6$, where A is replace by two different cations A and A'. Cation ordering at B-site is very common compared to A-site ordering. In AA'BBO_6, ordering between A and A' cations is rare. Generally, A-cations are alkali, alkali earth, lanthanide, Pb^{2+}, or Bi^{3+} cations which do not have charge difference greater than 2 which is the reason main why the ordering at A-site is rare. On the contrary charge difference between B and B' greater than 3 can be easy achieved. Despite this fact recently many AA'BB'O_6 compounds being reported which are ordered in A-site. The type of ordering in A-site is quite different than B-site where the layered ordering at A-site being the most common. Electrostatically rock-salt type ordering is the favored one because highly charged cations are apart from each other and this is the reason that rock-salt ordering is the most common at B-site. But for A-site, layer type of ordering is the preferred and the reason for this lies in the oxygen environment and related stability. If there is rock-salt ordering at A site, oxygen will be connected to two of each A-cations in trans fashion, and by symmetry the oxygen has no way to shift and stabilize the bonding (Fig. 4.1a). Whereas when there is layered type of ordering at A-site, the oxygen can now shift to form stable bonds with each of the A-cation (Fig. 4.1b). One sixth of the anions will reside in the AO layer and will be surrounded by four A-cations while another 1/6 of the anions will reside in the A'O layer and will be surrounded by four A'-cations. Since the A and A' cations are of different charges one of these anions will be over-bonded while the other will be under-bonded. Except for these 1/3 anions, rest 2/3 anions have stable bonding as compared to none stable bonding in rock-salt ordering of A-cations. But still the 1/3 bonding instability has to be relieved by some mechanism as described below.

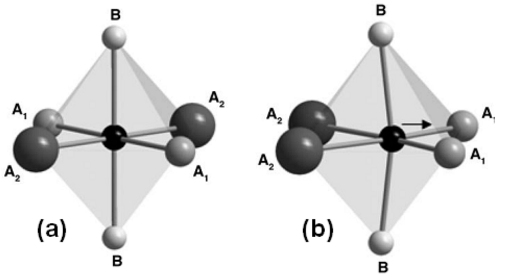

Figure 4.1 *Oxygen environments (a) with rock-salt ordering of A-cations, (b) with layered ordering of A-cations.*

Many examples are reported in literature where A-site ordering is observed in non-stoichiometric perovskite phases. Perovskites with $A_{1-x}BO_3$ show layered ordering of the A-site cation vacancies [1-4]. Perovskites of the type $A_{1-x}A'_yMO_3$ with a mixture of two different cations and vacancies on the A-sites shows various degrees of layered ordering and such system with formula $(Li_{3x}La_{2/3-x})TiO_3$ has been extensively studied for its lithium ion conductivity [5-7]. In this series the end compound $LiLaTi_2O_6$ does not show the A-cation ordering. While to the other end of non-stoichiometry, compounds with oxygen deficient perovskites $AA'B2O_{6-d}$ show layer type of ordering of A-cations. For example $RBaB_2O_5$ perovskites (R = trivalent rare earth cation) where the R and Ba atoms order into layers that run perpendicular to the c-axis with oxygen vacancies that lie exclusively within the R layers [8-11]. Thus in both the non-stoichiometric cases the bonding instability is relieved by formation of anion or cation deficiency. There are very few cases of non-stoichiometric where large charge differences can drive the ordering, although a significant amount of disorder is still present. For example, $Na_{2/3}Th_{1/3}TiO_3$, $NdAgTi_2O_6$, show partial ordering of A-cations [12, 13].

Since 1984 after the report of A-site ordered perovskite in $NaLaMgWO_6$ [14], many compounds were investigated to and shown to have such simultaneous ordering in A and B site [15-17]. The common features observed in these compounds are B’ cation is highly charged d0 cation which can displace off-center in its octahedron by means of a second order Jahn-Teller (SOJT) distortion. A SOJT distortion drives a displacement of the B’ cation, which in turn stabilizes layered ordering of the A and A’ cations as shown in the Fig. 4.2. Both effects act synergistically to remove the bonding disorder as discussed above.

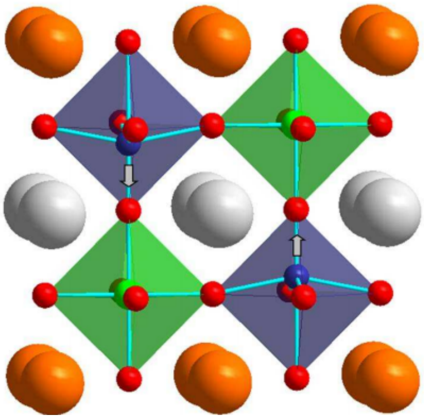

Figure 4.2 *A typical crystal structure of double perovskite AA’BB’O_6 with layered A-cations. A and A’ cations are ordered in layer shown in orange and grey color, respectively while B and B’ cations are ordered in rock-salt pattern shown in green and blue color, respectively. SOJT active B’cation is displaced from its mean position.*

Apart from the interesting crystal chemistry aspects of these A-cation ordered perovskites, they have been studied for functional properties like ionic conductivity [18-20], ferroelectric materials [21, 22], solar oxide fuel cells [23] etc. Lately, AA’BB’O_6 type perovskites are also been studied for their photoluminescence properties and shown to have applications in solid state devices in lighting [24-28].

4.2 Issues and scope of work

Many double perovskite compounds $A_2BB'O_6$ has been reported with highly charged B' cation (like Nb, Sb, Te, W, U) where almost always there is complete B-cation ordering [29]. But there was no study which reports $AA'BB'O_6$ compounds where the effect of size of A' cation is reported. Also crystal structure of the compounds in the above series are not reported previously or reported to be incorrect. Thus detailed crystal structure analysis was carried out in our study. M. L. Lopez et. al. reported the compound $NaLaMgTeO_6$ and showed to have A-cation ordering [30] but later M. C. Knapp and P. M. Woodward reported only partial (≈10%) ordering between Na and La in the same compound [15]. In the light of the above discussed criteria required for simultaneous ordering at A and B site, it is not clear why $NaLaMgTeO_6$ where Te^{6+} having d^{10} electronic configuration show A-site ordering. Thus in our study of series of compounds we check for such A-cation ordering and in particular compounds containing Te, Sb, and U at B'-site.

4.3 Synthesis

All the compounds were synthesized by solid state method. The initial reactants were preheated up to 300°C before weighing to remove any loose moisture. Carbonates of alkali metals and alkaline earth metals, $La(OH)_3$, TeO_2, Nb_2O_5, Sb_2O_3, WO_3, U_3O_8, Eu_2O_3 were used as starting reactants. For tellurate compounds the final annealing temperature for the formation of pure compound is 1000 °C and 740 °C for Na and K/Rb compounds, respectively with 35h of heating with intermittent grinding. For niobates and antimonates the final annealing temperature was 1350°C for 60h with intermittent grinding. Samples for photoluminescence measurements were prepared by gel combustion method with 2 atom% Eu doped at La site. The final annealing temperature and duration was kept same as for the un-doped samples.

4.4 Results and discussion

Five different systems BaLaBB'O_6 where B'= 4d (Nb, Sb, Te), B'=5d (W) and B'=5f (U) were considered for the study. Out of these syntheses pure single phase compound formation was possible only with 4d elements. Compounds with tungsten and uranium were not successful and were accompanied with impurity phases. In tungsten compounds there was formation of impurity like BWO_4 and with uranium compounds, impurities like barium uranates/ alkali metal uranates were formed. Hence the further study was carried out on 4d elements.

4.4.1 Niobate compounds

Crystal structure, photoluminescence and Infrared absorption spectroscopy studies were carried out on the $BaLaM^{2+}NbO_6$ (M=Mg, Ca, Sr, Ba) compounds (hence forth referred as MgNb, CaNb, SrNb and BaNb compounds, respectively). Of these the crystal structure of BaNb compound i.e. Ba_2LaNbO_6 has already been reported [31] and it is considered here for the comparison of crystal structure with other member of the series. Compound SrNb does not form pure homogeneous compound so is omitted from the discussion.

4.4.1.1 Crystal structure study

The XRD analysis confirmed the formation of perovskite type phase in the compounds $BaLaM^{2+}NbO_6$ (M=Mg, Ca), except for compound containing strontium. The reason for the same is discussed ahead. For MgNb compound the tolerance factor close to unity (τ =0.98) indicates that it crystallizes in higher symmetry. Figure 4.3a shows the XRD pattern of MgNb compound. The presence of low angle reflection marked with an asterisk "*" in corresponds to rock-salt ordering at B-cations. The XRD data was fitted with cubic $Fm\bar{3}m$ space group. The refinement residue and χ^2 values indicated good fit but the large value of thermal parameter (B_{iso}) for oxygen indicates lower symmetry. The next choice of space group which is closely related to cubic $Fm\bar{3}m$ space group is $R\bar{3}$. This space group gave smaller χ^2 values and acceptable Biso values indicating that space group $R\bar{3}$ is the better choice for MgNb compound than $Fm\bar{3}m$ space group. In this compound Ba and La atoms occupy A-site with no indication of A-site ordering and Mg and Nb atoms occupy B-site. Refinement of the anti-site disorder between Mg and Nb gave small anti-site disorder of 3%. Although many double perovskites with Nb^{5+} are shown to have A-cation ordering, in the current niobate compounds, no A-cation ordering between Ba and La is observed. The small charge and size difference between Ba^{2+} and La^{3+} cations is not sufficient to cause layer ordering at A-site.

The XRD pattern for CaNb compound (see Fig.4.3b) was indexed using $R\bar{3}$ space group. Though the tolerance factor reduced as compared to MgNb, the rhombohedral crystal structure is retained. The attempts to fit the XRD data using lower symmetry space groups like I4/m and I2/m were unsuccessful. Like in MgNb compound it can be assumed that Ba and Nb atoms will occupy A and B site, respectively considering their sizes. But the position of La and Ca is not straight forward as it was in MgNb compound. The ionic sizes of (La^{3+} and Ca^{2+}) cations in 12 and 6 co-ordinations very close, with the values (1.36Å and 1.34Å) for 12 co-ordinations and (1.032Å and 1.0Å) for 6 co-ordinations, respectively. The refinement was initiated by equal distribution of La and Ca atom at A and B-site. The converged occupancies show that, Ca preferably occupies B-site while La occupies A-site with 11% anti-site disorder. The ionic size of La being slightly larger than Ca drives the Ca ion to occupy B-site but, 11% anti-site disorder remains due to close ionic radii values. Similar to MgNb compound, CaNb compound also do not show A-cation ordering due to the same reason, that there is small difference between ionic charge and size between La and Ba atom. The Rietveld refinement analysis shows that the observed peaks are broad than calculated and this can be attributed to close solid solutions formed in the system $Ba(La_{1-x}Ca_x)(Ca_{1-x}La_x)NbO_6$. The high thermal parameter values for La and Ca atoms clearly show anti-site disorder effect (See table 4.1).

When Mg or Ca is replaced by Ba in BaNb compound, Ba atom occupies the A-site and La occupies B-site to give formula Ba_2LaNbO_6. W. T. Fu et al. reported the crystal structure of this compound and shown to have monoclinic structure with a space group I2/m [31]. The generated XRD pattern for Ba_2LaNbO_6 is shown in figure 4.3c. It is also observed in this compound that La and Nb are ordered in rock-salt pattern but the corresponding intensity of the reflection due to B-cation ordering decreases (marked with '*' sign in Fig.4.3c). It is observed that SrNb compound do not form pure phase but contains multiple phase mixtures. This can be understood from the structure of CaNb and BaNb compound. In CaNb compound Ca occupies B-site while in BaNb, La occupies B-site. Thus in case of SrNb compound there is competition for occupancy of Sr atom in A-site or B-site leading to instability and formation of mixture of phases.

Table 4.1 Refined crystal structural parameters for $BaLaMgNbO_6$ and $BaLaCaNbO_6$ compounds.

$BaLaMgNbO_6$

System: Rhombohedral, space group: R-3, Z=3

a = 5.6975(2)Å, c = 13.9628(9)Å, V = 392.52(3)Å^3,

Rp(%)=6.89, Rwp(%)=10.4, χ^2=1.58

Atom	**Site**	**x**	**y**	**z**	**Biso**	**Occupancy**
Ba/La	6c	0	0	0.2518(2)	0.46(8)	0.5/0.5
Mg	3b	0	0	1/2	0.17(3)	1
Nb	3a	0	0	0	0.31(5)	1
O	18f	0.120(2)	0.333(2)	0.0738(9)	0.23(7)	1

$BaLaCaNbO_6$

System: Rhombohedral, space group: R-3, Z=3

a = 5.9101(1)Å, c = 14.3908(7)Å, V = 435.31(2)Å^3,

Rp(%)=8.56, Rwp(%)=11.3, χ^2=1.51

Ba/La/Ca	6c	0	0	0.2466(4)	0.63(8)	0.5/0.445/0.055
Ca/La	3b	0	0	1/2	1.1(3)	0.89/0.11
Nb	3a	0	0	0	0.40(5)	1
O	18f	0.083(2)	0.288(3)	0.098(7)	0.75(7)	1

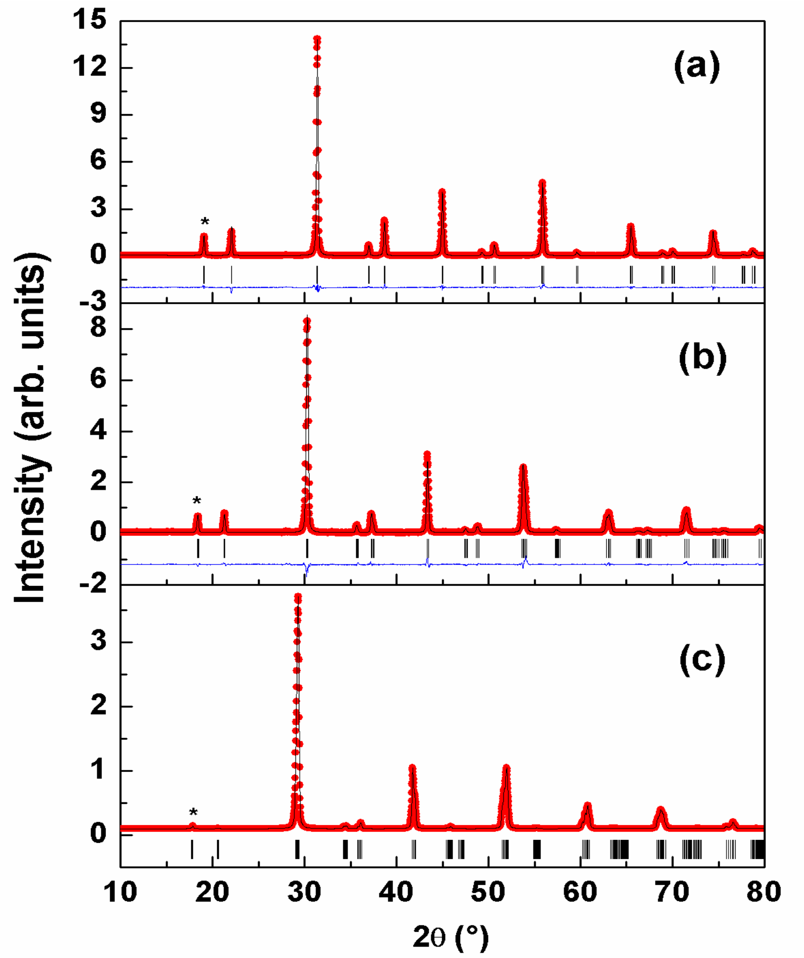

Figure 4.3 *Rietveld refinement of XRD data of (a)* $BaLaMgNbO_6$*, (b)* $BaLaCaNbO_6$ *and (c)* Ba_2LaNbO_6 *(pattern generated using crystal structure reported in reference [31]). The asterisk sign '*' indicates the reflection arising due to B-site rock salt ordering.*

4.4.1.2 Photoluminescence study

To probe the local geometry around the La atom in these compounds, photoluminescence study was carried out on 2 at. % europium doped samples. As Eu^{3+} has same ionic charge and similar ionic radius to La^{3+}, it is substituted at La position. Figure 4.4 shows the PL emission spectra for $BaLaM^{2+}NbO_6$ (M=Mg, Ca) and Ba_2LaNbO_6 compounds. The spectra shows two prominent emission lines $^5D_0$-$^7F_1$ (594nm) and $^5D_0$-$^7F_2$ (614nm) corresponding to magnetic dipole transition (MD) and electric dipole transition (ED), respectively. For comparison the spectra of all the compounds has been normalized with respect to emission line $^5D_0$-$^7F_1$. The MD transition $^5D_0$-$^7F_1$ is insensitive to local environment around the Eu^{3+} ion and thus used for normalizing the PL emission spectra, whereas ED transition $^5D_0$-$^7F_2$ is hyper-sensitive to local environment around the Eu^{3+} ion [32]. The relative ratio between these two emission lines gives a measure of the degree of distortion from the inversion symmetry around the Eu^{3+} ion in the host matrix. It is observed that MgNb compound has intense ED transition. In MgNb compound, La occupies A-site having 12-coordination and thus have distorted environment around Eu^{3+} ion. On the contrary, in BaNb compound i.e. Ba_2LaNbO_6, La ion occupies B-site with octahedral environment which has inversion symmetry and thus ED transition is very weak compared to MD transition. As discussed above, the CaNb compound solid solutions formed in the system $Ba(La_{1-x}Ca_x)(Ca_{1-x}La_x)NbO_6$, and thus Eu^{3+} ion is distributed over both A and B-site. Due to this, the ratio of emission lines in CaNb compound lies in between of MgNb and BaNb compounds. The PL emission study clearly supports the crystal structure analysis done using x-ray diffraction refinement.

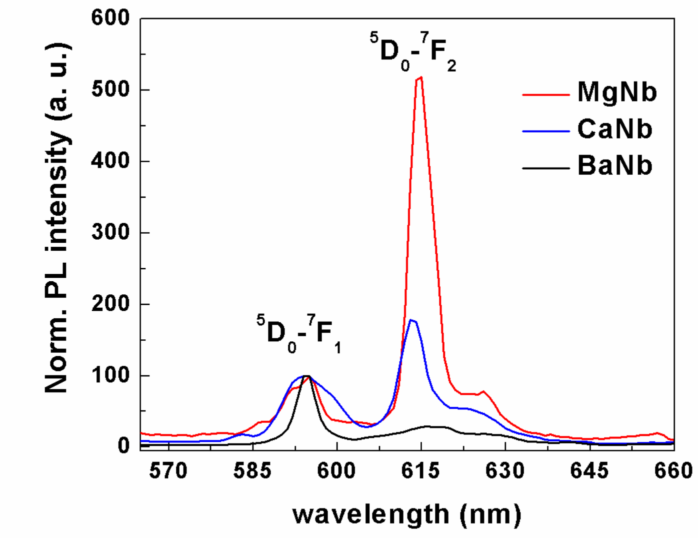

Figure 4.4 *Normalized PL emission spectra with 2 atom percent* Eu^{3+} *doped samples of* $BaLaM^{2+}NbO_6$ *(M=Mg, Ca) and* Ba_2LaNbO_6 *compounds.*

4.4.1.3 Infrared spectroscopy

Figure 4.5 shows the FTIR spectra recorded at room temperature for the three niobium compounds. The spectra match well with the reported perovskite phases containing Nb^{5+} [33, 34]. In general for perovskite compounds, the IR-spectra are dominated by the vibration of BO6 octahedra and leads to the strong absorption band in the frequency range 400–800 cm^{-1}. These bands are assigned to the asymmetric stretching and deformational modes of BO6 octahedra [35]. In double perovskites with two B-cations, the IR spectra have the combined effect of both BO6 and B’O6 octahedral vibrations. In these compounds it is observed that the centre of the absorption band shifts to the lower frequency with doping of larger alkaline earth metal. Here the NbO6 octahedra is common for all the compounds, thus the shifting of the band corresponds to the MgO6, CaO6 and LaO6 octahedral vibrations in $BaLaMgNbO_6$, $BaLaCaNbO_6$ and Ba_2LaNbO_6 compounds, respectively. In general, square of the frequency of any vibration is proportional to spring constant and inversely to reduced mass; $\omega = \sqrt{k/\mu}$. To a first approximation, assuming that the spring constant (k) is proportional to electronegativity of B-cation and considering the reduced mass of B-atom and oxygen atom it can be shown that centre of the vibration band is linear to $\sqrt{k/\mu}$ (shown in the inset of Fig. 4.5). Here the ratio $\sqrt{k/\mu}$ is averaged over both the B and B’ cations. Additionally, it is observed that the FWHM of the IR-absorption band is small in MgNb compound and it increases in CaNb and BaNb compounds. This fact can be explained from crystal symmetry of the compounds. The compound MgNb has rhombohedral symmetry with angle 59.98° which shows that it is very close to cubic symmetry whereas with same symmetry the CaNb compound has angle 60.26°. Moreover CaNb compound has anti-site disorder between Ca and La ions between A and B-site. The BaNb compound has monoclinic symmetry. Thus, as the symmetry reduces from MgNb to CaNb or BaNb compounds the FWHM of IR-absorption band increases.

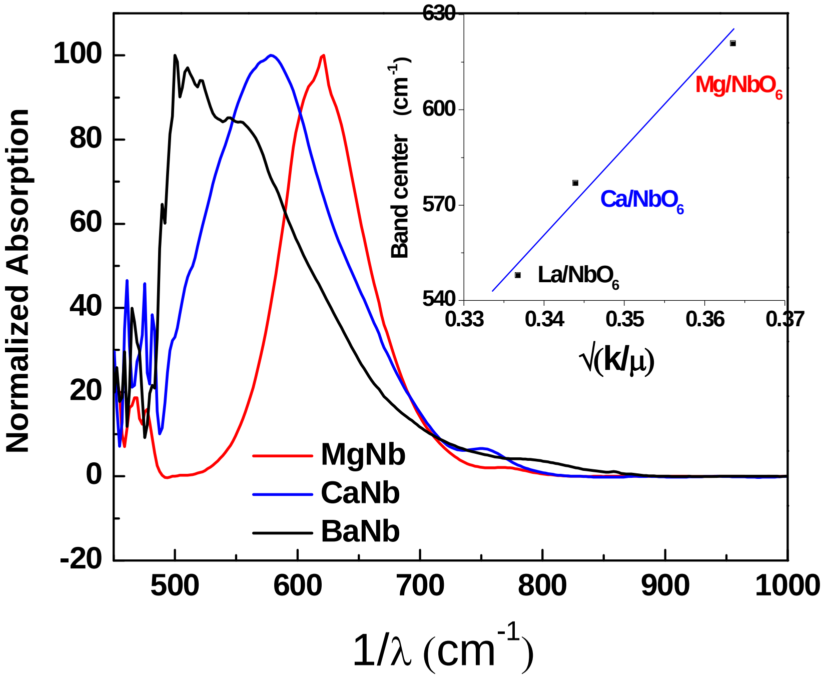

Figure 4.5 *FTIR spectra for* $BaLaM^{2+}NbO_6$ *(M=Mg, Ca, Ba) compounds. The absorption band corresponds to both octahedral vibrations B/B'O6. Inset shows linear trend between centre of vibration band and square root of ratio of electronegativity and reduced mass of B/B' and O atom averaged over both the B and B' atoms.*

4.4.2 Antimonate compounds

Crystal structure, photoluminescence and Infrared absorption spectroscopy studies were carried out on the $BaLaM^{2+}SbO6$ (M=Mg, Ca, Sr, Ba) compounds (Hence forth referred as MgSb, CaSb, SrSb and BaSb compounds, respectively). The crystal structure of Ba_2LaSbO_6 has already been reported [36], but we consider it here for the comparison of crystal structure with other members of the series. Compound SrSb does not form pure homogeneous compound so is omitted from the discussion.

4.4.2.1 Crystal structure study

The XRD analysis confirmed the formation of perovskite type phase in MgSb, CaSb compounds. Fig. 4.6 shows the observed XRD pattern for MgSb and CaSb compounds along with calculated XRD pattern of reported BaSb compound. The XRD pattern of MgSb compound shows mixture of two phases, the major phase corresponding to the stoichiometry $BaLaMgSbO_6$ (reflection peaks shown with upper line markers) and the minor secondary phase (reflection peaks shown with lower line markers) which also shows reflections similar to main phase but shifted to the lower two-theta. The large volume of the minor secondary phase and XRD peaks values match with the reported Ba_2LaSbO_6 compound indicates that it has the stoichiometry similar to Ba_2LaSbO_6 compound. The XRD analysis of the main phase shows that it crystallizes in high symmetry and it is indicative of its tolerance factor (τ =0.99). The presence of low angle reflection marked with an asterisk "*" corresponds to rock-salt ordering at B-cations. The major phase in MgSb compound was fitted with $Fm\bar{3}m$ space group but the large value of the thermal parameter (B_{iso}) for oxygen indicates lower symmetry. Thus similar to the MgNb compound, MgSb compound was indexed using $R\bar{3}$ space group. Ba and La atoms occupy A-site while Mg and Nb atoms occupy B-site. Negligible amount of anti-site disorder was observed at B-site and thus neglected. The minor secondary phase was refined using I2/m space group with stoichiometry Ba_2LaSbO_6. The 8 w/w % weight percentage of the minor secondary phase was estimated from Rietveld refinement of two phase mixtures.

The XRD pattern of CaSb compound (see Fig. 4.6b) was indexed using $R\bar{3}$space group. Similar to CaNb compound the XRD peaks of CaSb compound are broad and this indicates that there is mixture of nearby stoichiometric phases. The presence of intense reflection corresponding to B-cation ordering and Rietveld analysis show absence of anti-site disorder at B-site. CaSb compound show only 1% anti-site disorder between La and Ca between A and B-site, thus showing that almost all La occupies A-site. The refined crystal structure parameters are given in table 4.2.

When Mg or Ca is replaced by Ba in BaSb compound, Ba atom occupies the A-site and La occupies B-site to give Ba_2LaSbO_6. W. T. Fu et al. reported the crystal structure of this compound and shown to have rhombohedral structure with $R\bar{3}$ space group [36]. The generated XRD pattern for Ba_2LaSbO_6 is shown in fig. 4.6c. It is interesting that all the compounds in the antimonate series have rhombohedral structure. Although in both the cases of CaNb and CaSb compounds the tolerance factor is low as 0.92 and 0.93 respectively, the best structure refinement was possible using rhombohedral $R\bar{3}$ space group. The monoclinic space groups like I2/m or I4/m were considered for the refinement of crystal structure of CaNb and CaSb compounds, but gave poor results compared to rhombohedral $R\bar{3}$ space group.

Table 4.2 Refined crystal structural parameters for BaLaMgSbO$_6$ and BaLaCaSbO$_6$ compounds.

BaLaMgSbO$_6$						
System: Rhombohedral, space group: R-3, Z=3						
a = 5.6873(1)Å, c = 13.9473(4)Å, V = 390.69(2)Å^3,						
Rp(%)= 7.08, Rwp(%)= 10.7, χ^2= 1.77						
Atom	**Site**	**x**	**y**	**z**	**Biso**	**Occupancy**
Ba/La	6c	0	0	0.2527(2)	0.37(5)	0.5/0.5
Mg	3b	0	0	1/2	0.21(3)	1
Sb	3a	0	0	0	0.21(3)	1
O	18f	0.122(3)	0.329(2)	0.075(3)	0.41(7)	1
BaLaCaSbO$_6$						
System: Rhombohedral, space group: R-3, Z=3						
a = 5.9028(1)Å, c = 14.4081(4)Å, V = 434.76(2)Å^3,						
Rp(%)= 7.97, Rwp(%)= 12.9, χ^2= 2.6						
Ba/La	6c	0	0	0.2485(2)	0.46(8)	0.5/0.465/0.035
Ca	3b	0	0	1/2	0.17(3)	0.93/0.07
Sb	3a	0	0	0	0.31(5)	1
O	18f	0.109(4)	0.299(2)	0.085(1)	0.23(7)	1

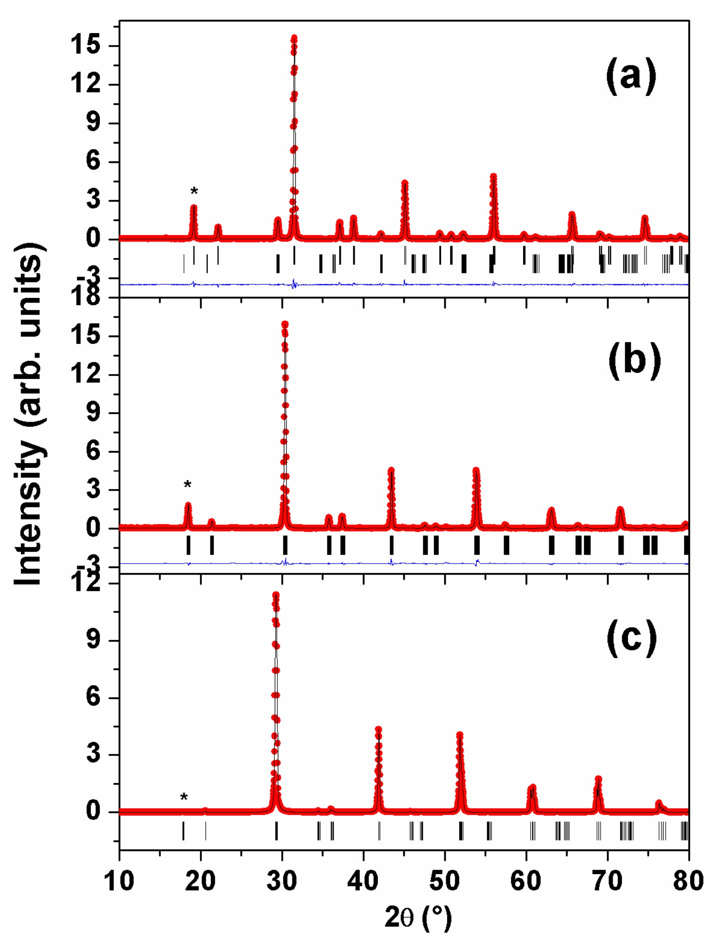

Figure 4.6 *Rietveld refinement of XRD data of (a) $BaLaMgSbO_6$, (b) $BaLaCaSbO_6$ and (c) Ba_2LaSbO_6 (pattern generated using crystal structure reported in reference [36]). The asterisk sign '*' indicates the reflection arising due to B-site rock salt ordering.*

4.4.2.2 Photoluminescence study

To probe the local geometry around the La atom in these compounds, photoluminescence study was carried out on 2 atom percent europium doped samples. Similar to MgNb compound, Eu^{3+} ion will occupy the La^{3+} site. Fig. 4.7 shows the PL emission spectra for the three compounds. In contrast to MgNb compound, MgSb compound shows less intensity of ED transition ($^5D_0$-$^7F_2$) and even less as compared to the CaSb compound. This can be attributed to two phase mixtures formed in MgSb compound. In the major phase Eu^{3+} occupy A-site and should give high intensity for ED transition similar to MgNb compound. But the observed PL emission spectra shows that ED transition is less and comparable to MD transition. The minor secondary phase have the stoichiometry close to Ba_2LaSbO_6 and considering the smaller size of Eu^{3+}, it will preferably occupy the La^{3+} site in this phase. Thus presence of 8% w/w of minor phase leads to decrease in the ED transition line in PL emission spectra. Similar to BaNb compound, BaSb compound shows very weak intensity of ED transition as Eu^{3+} ion occupies B-site with octahedral environment. Compound CaSb shows similar intensity ratio of ED and MD transition as compared to CaNb compound. As discussed earlier, CaNb compound show anti-site disorder between Ca and La causes decrease in intensity of ED transition. But similar situation of anti-site disorder between Ca and La is not observed in CaSb compound and thus this reason is not correct in CaSb compound. The decrease in ED transition intensity indicates that Eu^{3+} ion occupy symmetric octahedral site. Even though the samples for PL study were prepared by solution route, thermodynamically it is always possible to form phases having nearby stoichiometric. Thus, the formation of $BaCaEuSbO_6$ compound is responsible for the decrease of ED transition intensity.

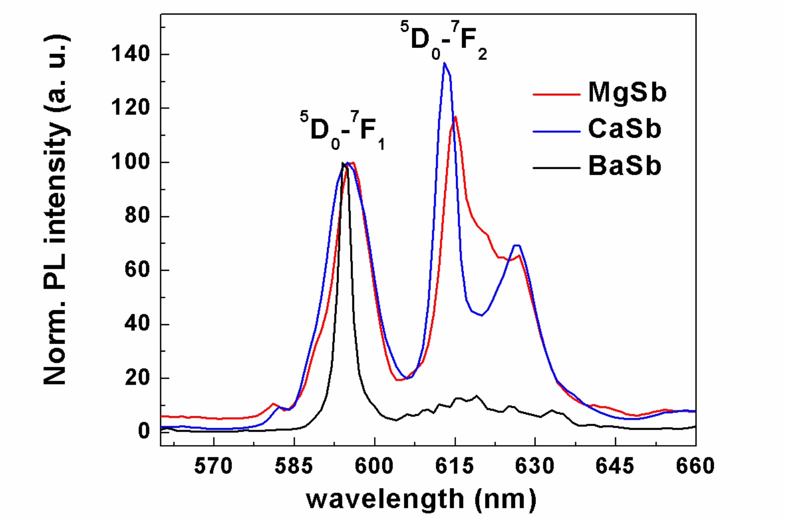

Figure 4.7 *Normalized PL emission spectra with 2 atom percent* Eu^{3+} *doped samples of* $BaLaM^{2+}SbO_6$ *(M=Mg, Ca) and* Ba_2LaSbO_6 *compounds.*

4.4.2.3 Infrared spectroscopy

Fig. 4.8 shows the FTIR spectra recorded at room temperature for the three antimony compounds. Spectra match well with the reported IR-spectra of perovskites containing Sb^{5+} [37, 38]. In antimonates the strong absorption band corresponding to BO6 octahedra are shifted to the higher wave-number (i.e. to higher energy) as compared to niobates. This is due to the higher elctronegativity value for Sb^{5+} (1.971) compared to Nb^{5+} (1.862). This indicates that the bond strength is more in case of antimonates. Similar to niobates the center of the absorption band shifts to the lower energy from Mg to Ba and can be co-related to Mg/SbO6, Ca/SbO6 and La/SbO6 octahedra for $BaLaMgSbO_6$, $BaLaCaSbO_6$ and $Ba2LaSbO_6$ compounds, respectively. Similar to niobates centre of the absorption band varies linearly to $\sqrt{k/\mu}$, where k is proportional to electronegativity and μ is the reduced mass of B atom and oxygen averaged over both the B and B' cations (shown in the inset of Fig. 4.8). The FWHM of IR-absorption band is small in MgSb compound and increases in CaSb and BaSb compounds. Similar to niobates this again can be correlated to decrease in the crystal symmetry.

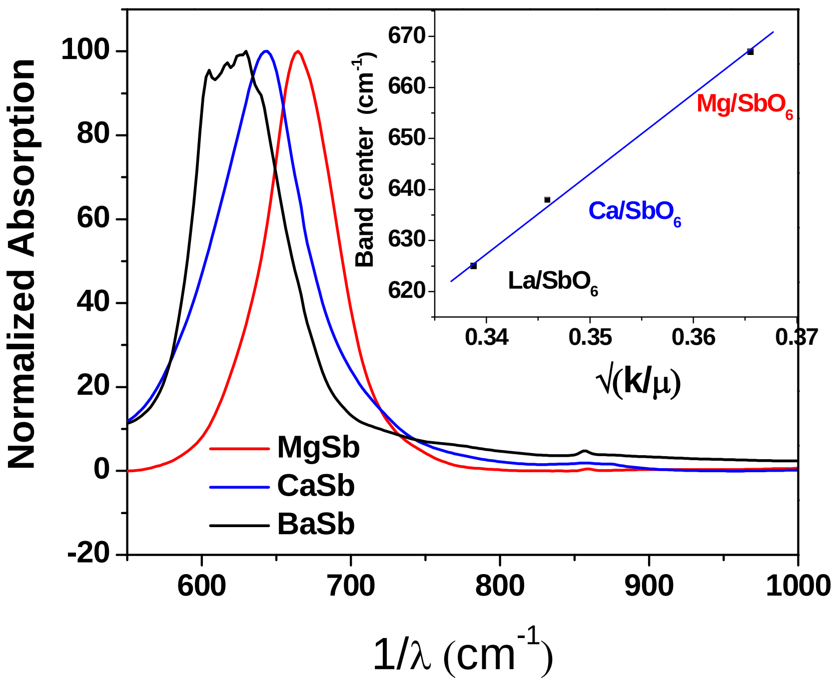

Figure 4.8 *FTIR spectra for BaLaM^{2+}SbO$_6$ (M=Mg, Ca, Ba) compounds. The absorption band corresponds to both octahedral vibrations B/B'O6. Inset shows linear trend between centre of vibration band and square root of ratio of electronegativity and reduced mass of B/B' and O atom averaged over both the B and B' atoms.*

4.4.2 Tellurate compounds

Crystal structure and photoluminescence study was carried out on the BaLaM^{1+}TeO$_6$ (M=Na, K, Rb) compounds (hence forth referred as NaTe compound, KTe compound and RbTe compound, respectively).

4.4.2.1 Crystal structure study

The XRD data analysis confirmed formation of a single phase compounds. The 2θ positions for the NaTe compound matched with the initial reported in literature [39]. According to this report, the NaTe compound crystallizes in cubic $Fm\bar{3}m$ space group. However, the Rietveld refinement using the space group $Fm\bar{3}m$ was unsuccessful as the higher angle reflections clearly shows multiple hkl reflections merged together and could not be fitted correctly with single peaks described by $Fm\bar{3}m$ space group. The XRD data could be properly indexed using monoclinic system which is indicative of its low tolerance (τ =0.93). The XRD shows low angle super lattice reflection due to rock-salt type ordering at B site as marked with an asterisk "*" in Fig. 4.9 The ionic size of Ba^{2+} and Te^{6+} clearly forces them to occupy A and B sites, respectively but ionic size of La^{3+} and Na^{1+} are very close in both the 12 and 6 co-ordination and occupation of them is not straight forward. Very intense super lattice reflection due to rock-salt type ordering at B site indicates that Na occupy the B site. The good contrast in atomic number of Na and Te as compared to La and Te results in intense B-cation ordering reflection. Space group $P2_1/n$ was used for the refinement of the XRD data. Using this space group, intensities of the reflection for the NaTe compound were fitted correctly. The Rietveld refinement of XRD data is shown in Fig. 4.9a. In order to check the possibility for the site disorder between La and Na at A and B site, respectively, we varied the occupancy of La at A-site and Na at B site by exchanging their positions and checked for the variation in the R factors and χ^2 values.

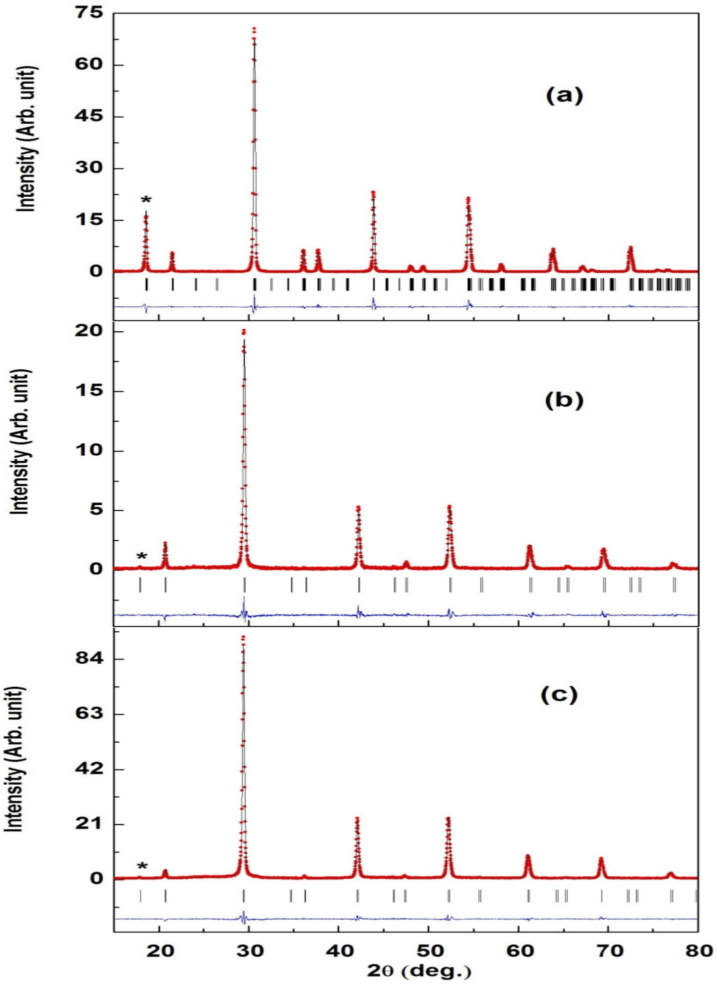

Figure 4.9 *Rietveld refinement of XRD data of (a) BaLaNaTeO$_6$, (b) BaKLaTeO$_6$ and (c) BaRbLaTeO$_6$. The asterisk sign '*' indicates the prominent reflection due to B site rock salt ordering.*

χ^2 values. Even small variation of 1% from their preferred sites led to a significant increase in χ^2 values. It is therefore, concluded, La and Na purely occupy A and B sites, respectively. XRD analysis also shows 100% B-cation ordering between Na and Te. As described by Graham King and Patrick M. Woodward in their article [17], the ordering between Ba and La is not possible and thus no signs of A-site ordering was observed in our XRD data. XRD patterns of KTe and RbTe compounds indicate cubic structure as against the monoclinic structure of the NaTe compound (Fig. 4.9). It is expected in the KTe/RbTe compound, that the K/Rb ion will occupy A site due to their large ionic radii. In case of KTe and RbTe compounds low angle supper-lattice reflection due to rock-salt type ordering at B site (marked with "*" sign in Fig. 4.9) is weak compared to the NaTe compound. In KTe/RbTe compounds ordering take place between La and Te ions, where the atomic number difference is less and result in weak charge ordering reflection. Though this reflection is weak in KTe and RbTe compounds, they are clearly observed in order to assign the $Fm\bar{3}m$ space group. Rietveld refinement was done for KTe and RbTe compounds, where Ba and K/Rb occupy A site with random distribution; La and Te occupy B site. XRD analysis shows complete ordering Between B-cations and confirms that charge difference of three and the respective ionic size difference between La^{3+} and Te^{6+} is enough for ordering to occur at B site in KTe/RbTe compounds. Attempts to distribute La over both A and B sites result in a poor fit, thus confirming that La occupies only B site in KTe and RbTe compounds in contrast to the NaTe compound where it occupies A site to give crystallographic site swapping of La. To get a better estimate of the structural parameters, particularly those of the lighter oxygen atom in the presence of other heavier elements, NPD was recorded at room temperature for the NaTe and RbTe compounds. Fig. 4.10 shows the Rietveld refinement of NPD data. Details of the crystal structure analysis for all the three compounds are given in table 4.3.

Table 4.3 Refined crystal structural parameters for $BaLaNaTeO_6$, $BaKLaTeO_6$ and $BaRbLaTeO_6$ compounds.

$BaLaNaTeO_6$						
System: Monoclinic, space group: $P2_1/n$, Z=2						
a = 5.8245(3)Å, b = 5.8412(3)Å, c = 8.2444(4)Å, β = 90.295(3)°, V = 280.48(2)$Å^3$,						
Rp(%)=8.77, Rwp(%)=13.1, χ^2=1.37						
Atom	**Site**	**x**	**y**	**z**	**Biso**	**Occupancy**
Ba/La	4e	0.4934(3)	0.5071(2)	0.2467(3)	0.68(3)	0.5/0.5
Na	2d	1/2	0	0	0.99(4)	1
Te	2c	0	1/2	0	0.37(3)	1
O1	4e	0.221(4)	0.265(4)	0.056(1)	1.89(5)	1
O2	4e	0.196(3)	0.760(5)	0.030(3)	1.89(5)	1
O3	4e	0.535(3)	0.025(4)	0.264(3)	1.89(5)	1
$BaKLaTeO_6$						
System: Cubic, space group: Fm-3m, Z=4						
a = 8.5530(4)Å, V = 625.70(5)$Å^3$,						
Rp(%)=12.0, Rwp(%)=17.2, χ^2=1.04						
Ba/K	8c	1/4	1/4	1/4	0.30(9)	0.5/0.5
La	4a	0	0	0	0.84(3)	1
Te	4b	1/2	1/2	1/2	0.84(4)	1
O	24e	0.271(3)	0	0	2.13(4)	1
$BaRbLaTeO_6$						
System: Cubic, space group: Fm-3m, Z=4						
a = 8.5781(2)Å, V = 631.21(2)$Å^3$,						
Rp(%)=7.81, Rwp(%)=10.4, χ^2=1.43						
Ba/Rb	8c	1/4	1/4	1/4	0.71(3)	0.5/0.5
La	4a	0	0	0	0.49(4)	1
Te	4b	1/2	1/2	1/2	0.49(4)	1
O	24e	0.276(3)	0	0	1.35(3)	1

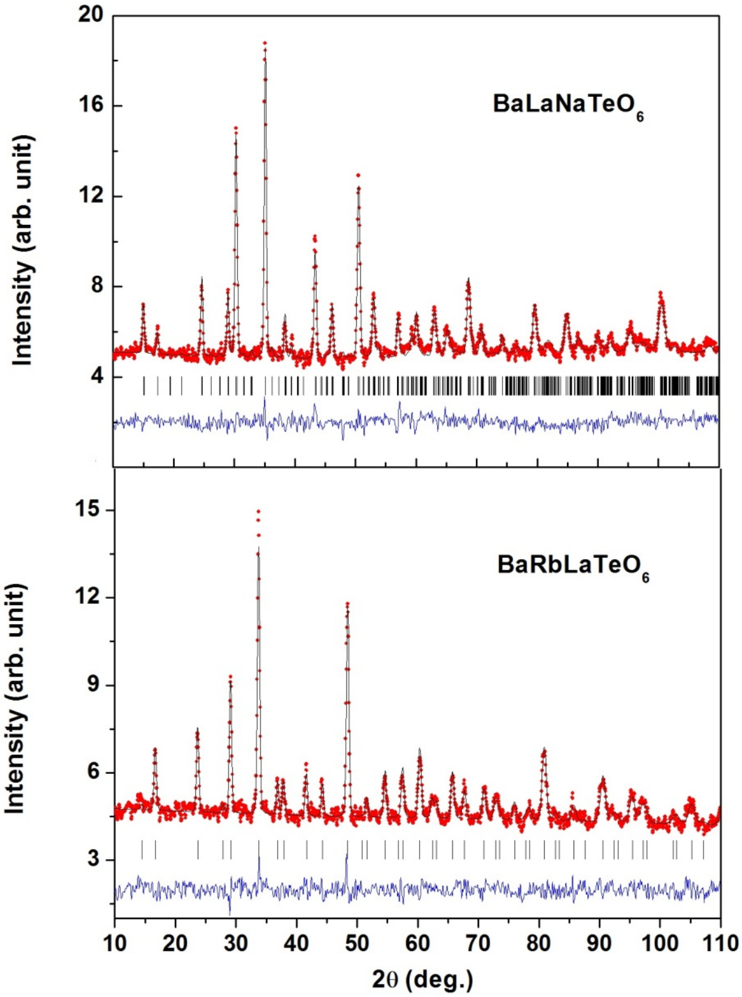

Figure 4.10 *Room temperature neutron diffraction Rietveld refinement plot for* $BaLaNaTeO_6$ *and* $BaRbLaTeO_6$

The refined crystal structure is indicative of the tolerance factor. The tolerance factor calculated for $BaLaNaTeO_6$ compound is 0.93 and thus suggests a low symmetry. In case of $BaLaLiTeO_6$ the tolerance factor increases to 0.99 indicating the cubic symmetry. $BaLaLiTeO_6$ crystallizes in $Fm\bar{3}m$ space group as previously reported in the literature [40]. Assuming the same formula as the NaTe compound; tolerance factors calculated for $BaLaKTeO_6$ and $BaLaRbTeO_6$ are 0.86 and 0.84, respectively. The low values of tolerance factors for these compounds suggest that both the compounds should have lower symmetry like the NaTe compound. The tolerance factor calculated by interchanging the position of La and K/Rb atoms corresponding to the formula $BaKLaTeO_6$ and $BaRbLaTeO_6$ are 0.97 and 0.99, respectively. These values indicate a cubic symmetry for these compounds and are confirmed from our diffraction analysis.

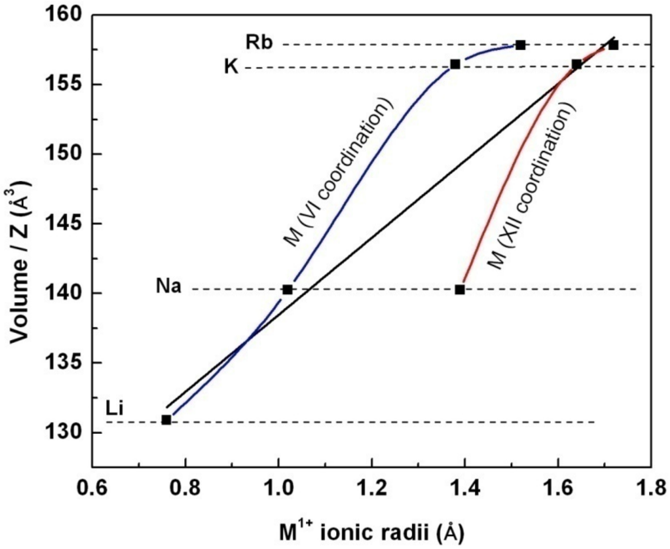

Figure 4.11 *Volume per unit formula vs. ionic radii. Blue and red line are drawn using the ionic size of alkali metal in six and twelve coordination, respectively; while the black line is drawn using Li and Na in six coordination and K and Rb in twelve coordination*.

Fig. 4.11 shows the plot of volume per formula (Volume/Z) unit with ionic radii of alkali metals in six and twelve coordination environment (values of ionic radii are taken from Shannon's data [41]). It is interesting to note that the variation of (Volume/Z) with ionic radii in six coordination (blue line) or twelve coordination (red line) is nonlinear, while it is linear in the case where Na and Li are in six coordination and K and Rb are in twelve coordination (black line). This is apparent due to the interchange of La ionic position with alkali metal ion in NaTe and KTe/RbTe compounds.

4.4.2.2 Photoluminescence study

To further investigate the observed crystallographic site swapping of La^{3+} ion in NaTe and KTe/RbTe compounds and study its effect on photoluminescence properties, Eu^{3+} was doped in place of La^{3+}.

Fig. 4.12 shows the dependence of the PL emission spectra (obtained with excitation of wavelength $\lambda_{ex} = 260$ nm) of Eu^{3+} ion in NaTe and RbTe compounds. The emission spectrum shows the europium emission lines of $^5D_0 \rightarrow ^7F_1$ (MD transition), $^5D_0 \rightarrow ^7F_2$ (ED transition). In NaTe compound the ED transition is more intense than MD transition. In NaTe compound, Eu3+ ion occupy A-site and thus have distorted environment with 12-coordination. While in RbTe compound the Eu^{3+} ion occupy octahedral B-site. This site is being octahedral is more symmetric and thus the ED transition intensity decreases. This PL analysis supports the crystal structure analysis done using diffraction data.

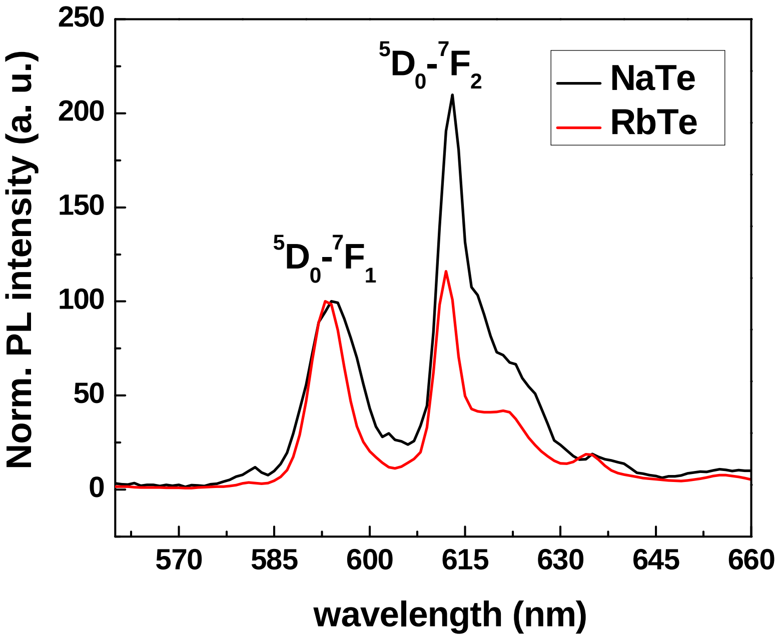

Figure 4.12 *Normalized emission spectra on excitation with charge transfer band for 6 atom percent Eu^{3+} doped sample of $BaLaNaTeO_6$ and $BaRbLaTeO_6$.*

4.5 Conclusions

Compounds of the series $BaLaBB'O_6$ where B'= 4d (Nb, Sb, Te), B'=5d (W) and B'=5f (U) were studied. Compounds with tungsten and uranium do not form pure perovskite type compounds. In rest of the cases i.e. in niobates, antimonates and tellurates form the pure perovskite type phases and were further investigated using X-ray powder diffraction, photoluminescence and IR-spectroscopy methods. All the compounds in these series show rock-salt type B-cation ordering due to large ionic charge and relatively small size of B'-cations (Nb^{5+}, Sb^{5+}, Te^{6+}). None of the compound showed layer type ordering between A-cations. Particularly, for Nb^{5+} which is SOJT active ion, many niobates has been reported to show simultaneous A and B-cation ordering. In tellurate system, $NaLaMgTeO_6$ compound is the only known perovskite phase which shows simultaneous A and B-cation ordering. But in the currently studied niobate and tellurate series, relatively small difference in size and ionic charge at A-site is not favorable for ordering at A-site. In all these series, as the size of the B-cation increases it is shifted from B-site to A-site and La ion is shifted to B-site. Due to this the tolerance factor changes accordingly and causes change in the crystal symmetry. The shifting of the La^{3+} cation from A-site to B-site was studied using photoluminescence of Eu^{3+} doped samples, where Eu^{3+} ion is doped at La^{3+} site. The ratio of the ED ($^5D_0$-$^7F_2$) to MD ($^5D_0$-$^7F_1$) transition in PL emission spectra signifies the local environment around Eu^{3+} ion. When Eu^{3+} ion occupy A-site, it gives strong ED transition intensity while when Eu^{3+} occupy B-site intensity of the ED transition decreases drastically as compared to MD transition. Thus in all these compounds the PL analysis is used for probing local environment around Eu^{3+} ion and it is in concordance with crystal structure analysis. FTIR spectra were recorded for niobate and antimonate series and spectra shows prominent absorption band in the range 400–800 cm^{-1}. These bands are assigned to the asymmetric stretching and deformational modes of B/B'O6 octahedra. The center position of the absorption bands are correlated to the electronegativity values of B/B’ cations and reduced mass of B/B’-O system. From the first principle approximation, assuming the bond force constant is proportional to electronegativity value, the absorption band center was shown to be proportional to $\sqrt{k/\mu}$. Additionally the FWHM of absorption band in IR-spectra increases as the symmetry of the compounds in the series decreases.

4.6 References

[1] A.R. Chakhmouradian, R.H. Mitchell, P.C. Burns, The A-site deficient ordered perovskite $Th_{0.25}\square_{0.75}NbO_3$: a re-investigation, Journal of Alloys and Compounds 307(1–2) (**2000**) 149-156.

[2] B.J. Kennedy, C.J. Howard, Y. Kubota, K. Kato, Phase transition behaviour in the A-site deficient perovskite oxide $La_{1/3}NbO_3$, Journal of Solid State Chemistry 177(12) (**2004**) 4552-4556.

[3] A.S. Sefat, G. Amow, M.-Y. Wu, G.A. Botton, J.E. Greedan, High-resolution EELS study of the vacancy-doped metal/insulator system, $Nd_{1-x}TiO_3$, x = 0 to 0.33., Journal of Solid State Chemistry 178(4) (**2005**) 1008-1016.

[4] J.H. Christopher, Z. Zhaoming, Structures and phase transition in the layered perovskite $La_{0.6}Sr_{0.1}TiO_3$: a new orthorhombic structure solved from high-resolution diffraction in combination with group theoretical analysis, Journal of Physics: Condensed Matter 15(26) (**2003**) 4543.

[5] A.G. Belous, Lithium ion conductors based on the perovskite $La_{23-x}Li_{3x}TiO_3$, Journal of the European Ceramic Society 21(10–11) (**2001**) 1797-1800.

[6] A. Rivera, C. León, J. Santamaría, A. Varez, M.A. Paris, J. Sanz, $Li_{3x}La_{(2/3)-x}TiO_3$ fast ionic conductors.: Correlation between lithium mobility and structure, Journal of Non-Crystalline Solids 307–310 (**2002**) 992-998.

[7] Y. Harada, T. Ishigaki, H. Kawai, J. Kuwano, Lithium ion conductivity of polycrystalline perovskite $La_{0.67-x}Li_{3x}TiO_3$ with ordered and disordered arrangements of the A-site ions, Solid State Ionics 108(1–4) (**1998**) 407-413.

[8] J.P. Chapman, J.P. Attfield, M. Molgg, C.M. Friend, T.P. Beales, A Ferrimagnetic Manganese Oxide with a Layered Perovskite Structure: $YBaMn_2O_5$, Angewandte Chemie International Edition in English 35(21) (**1996**) 2482-2484.

[9] P. Karen, E. Suard, F. Fauth, P.M. Woodward, $YBaMnCoO_5$; neither valence mixed nor charge ordered, Solid State Sciences 6(11) (**2004**) 1195-1204.

[10] P.M. Woodward, E. Suard, P. Karen, Structural Tuning of Charge, Orbital, and Spin Ordering in Double-Cell Perovskite Series between $NdBaFe_2O_5$ and $HoBaFe_2O_5$, Journal of the American Chemical Society 125(29) (**2003**) 8889-8899.

[11] P.M. Woodward, P. Karen, Mixed Valence in $YBaFe_2O_5$, Inorganic Chemistry 42(4) (**2003**) 1121-1129.

[12] R.H. Mitchell, A.R. Chakhmouradian, A Structural Study of the Perovskite Series $Na_{1/2+x}La_{1/2-3x}Th_{2x}TiO_3$, Journal of Solid State Chemistry 138(2) (**1998**) 307-312.

[13] J.H. Park, P.M. Woodward, J.B. Parise, Predictive Modeling and High-Pressure−High-Temperature Synthesis of Perovskites Containing Monovalent Silver, Chemistry of Materials 10(10) (**1998**) 3092-3100.

[14] S. Tadashi, Y. Tetsuo, T. Yasuyoshi, Cation Ordering in $(NaLa)(MgW)O_6$ with the Perovskite Structure, Bulletin of the Chemical Society of Japan 57(7) (**1984**) 1859-1862.

[15] M.C. Knapp, P.M. Woodward, A-site cation ordering in $AA'BB'O_6$ perovskites, Journal of Solid State Chemistry 179(4) (**2006**) 1076-1085.

[16] G. King, S. Thimmaiah, A. Dwivedi, P.M. Woodward, Synthesis and Characterization of New AA′BWO$_6$ Perovskites Exhibiting Simultaneous Ordering of A-Site and B-Site Cations, Chemistry of Materials 19(26) (**2007**) 6451-6458.

[17] G. King, P.M. Woodward, Cation ordering in perovskites, Journal of Materials Chemistry 20(28) (**2010**) 5785-5796.

[18] S. Stramare, V. Thangadurai, W. Weppner, Lithium Lanthanum Titanates: A Review, Chemistry of Materials 15(21) (**2003**) 3974-3990.

[19] H. Stephen, Superionics: crystal structures and conduction processes, Reports on Progress in Physics 67(7) (**2004**) 1233.

[20] B. Zhang, G. Chen, H. Li, Review of perovskite structure solid state lithium ion conductor, Journal of Rare Earths 24(SUPPL. 3) (**2006**) 132-138.

[21] N.A. Benedek, J.M. Rondinelli, H. Djani, P. Ghosez, P. Lightfoot, Understanding ferroelectricity in layered perovskites: new ideas and insights from theory and experiments, Dalton Transactions 44(23) (**2015**) 10543-10558.

[22] T. Fukushima, A. Stroppa, S. Picozzi, J.M. Perez-Mato, Large ferroelectric polarization in the new double perovskite NaLaMnWO$_6$ induced by non-polar instabilities, Physical Chemistry Chemical Physics 13(26) (**2011**) 12186-12190.

[23] J.C. Pérez-Flores, D. Pérez-Coll, S. García-Martín, C. Ritter, G.C. Mather, J. Canales-Vázquez, M. Gálvez-Sánchez, F. García-Alvarado, U. Amador, A- and B-Site Ordering in the A-Cation-Deficient Perovskite Series La$_{2-x}$NiTiO$_{6-\delta}$ ($0 \leq x < 0.20$) and Evaluation as Potential Cathodes for Solid Oxide Fuel Cells, Chemistry of Materials 25(12) (**2013**) 2484-2494.

[24] J. Hou, X. Yin, F. Huang, W. Jiang, Synthesis and photoluminescence properties of NaLaMgWO$_6$:RE^{3+} (RE = Eu, Sm, Tb) phosphor for white LED application, Materials Research Bulletin 47(6) (**2012**) 1295-1300.

[25] L. Zhang, Z. Lu, P. Han, L. Wang, Q. Zhang, Synthesis and photoluminescence of Eu3+-activated double perovskite NaGdMg(W, Mo)O$_6$ - a potential red phosphor for solid state lighting, Journal of Materials Chemistry C 1(1) (**2013**) 54-57.

[26] R. Phatak, S.K. Gupta, K. Krishnan, S.K. Sali, S.V. Godbole, A. Das, Crystallographic site swapping of La^{3+} ion in BaA'LaTeO6 (A' = Na, K, Rb) double perovskite type compounds: diffraction and photoluminescence evidence for the site swapping, Dalton Transactions 43(8) (**2014**) 3306-3312.

[27] Q. Liu, L. Wang, L. Zhang, H. Yang, M. Yu, Q. Zhang, Enhanced luminescence and structure evolution of double perovskite (K, Na)LaMgWO$_6$:Eu^{3+} phosphor for white LEDs, Journal of Materials Science: Materials in Electronics 26(10) (**2015**) 8083-8088.

[28] A.R. Sharits, J.F. Khoury, P.M. Woodward, Evaluating NaREMgWO$_6$ (RE = La, Gd, Y) Doubly Ordered Double Perovskites as Eu^{3+} Phosphor Hosts, Inorganic Chemistry 55(23) (**2016**) 12383-12390.

[29] S. Vasala, M. Karppinen, A2B′B″O$_6$ perovskites: A review, Progress in Solid State Chemistry 43(1–2) (**2015**) 1-36.

[30] M.L. Lopez, M.L. Veiga, C. Pico, Cation ordering in distorted perovskites (MLa)(MgTe)O$_6$, M = Na, K, Journal of Materials Chemistry 4(4) (**1994**) 547-550.

[31] W.T. Fu, D.J.W. Ijdo, New insight into the symmetry and the structure of the double perovskites Ba$_2$LnNbO$_6$ (Ln=lanthanides and Y), Journal of Solid State Chemistry 179(4) (**2006**) 1022-1028.

[32] K. Binnemans, Interpretation of europium(III) spectra, Coordination Chemistry Reviews 295 (**2015**) 1-45.

[33] A.E. Lavat, E.J. Baran, IR-spectroscopic characterization of A2BB′O$_6$ perovskites, Vibrational Spectroscopy 32(2) (**2003**) 167-174.

[34] R. Mukherjee, B. Ghosh, S. Saha, C. Bharti, T.P. Sinha, Structural and electrical transport properties of a rare earth double perovskite oxide: Ba2ErNbO$_6$, Journal of Rare Earths 32(4) (**2014**) 334-342.

[35] S.D. Ross, Inorganic infrared and Raman spectra, McGraw-Hill**1972**.

[36] W.T. Fu, D.J.W. Ijdo, X-ray and neutron powder diffraction study of the double perovskites Ba_2LnSbO_6 (Ln=La, Pr, Nd and Sm), Journal of Solid State Chemistry 178(7) (**2005**) 2363-2367.

[37] W. Zheng, W. Pang, G. Meng, Hydrothermal synthesis and characterization of perovskite-type Ba_2SbMO_6 (M=In, Y, Nd) oxides, Materials Letters 37(4–5) (**1998**) 276-280.

[38] C. Vijayakumar, H.P. Kumar, S. Solomon, J.K. Thomas, P.R.S. Wariar, A. John, FT-Raman and FT-IR vibrational spectroscopic studies of nanocrystalline Ba_2RESbO_6 (RE = Sm, Gd, Dy and Y) perovskites, Journal of Alloys and Compounds 480(2) (**2009**) 167-170.

[39] Y.U.N. Venevtsev, E.D. Politova, G.S. Zhdanov, Tellurium containing ferroelectrics: X-ray data, dielectric properties, phase transitions, Ferroelectrics 8(1) (**1973**) 489-490.

[40] M.L. López, A. Jerez, C. Pico, R. Sáez-Puche, M.L. Veiga, Synthesis, Crystal Structure, and Magnetic Susceptibility of $MLnLiTeO_6$ (M = Ca, Sr, Ba), Journal of Solid State Chemistry 105(1) (**1993**) 19-26.

[41] R.D. Shannon, Revised effective ionic radii and systematic studies of interatomic distances in halides and chalcogenides, Acta Crystallographica Section A 32(5) (**1976**) 751-767.

Chapter 5.

Crystal structure analysis of $Ba_2La_{2/3}M^{5+}O_{5.5}$ compounds for M=Nb, Sb, Bi, U.

5.1 Introduction

It is well known that perovskite crystal structure has stability towards anion as well as cation deficiency and gives an extra dimension to tailor-make the required functional properties. These cation and anion deficient perovskite have found wide application in solid oxide fuel cells, ionic conductors, catalyst etc [1, 2]. In general, it is observed that anion deficient perovskite compounds are more stable than cation deficient due to the fact that defect energy in cation deficient phase is much higher. There are a wide range of oxide deficient perovskite compounds and are covered in details in various review articles [3-7]. Though, it is difficult to synthesize cation deficient perovskites there are several reports on the possibility of creating vacancy at A and B site i:e $A_{1-x}BO_3$ or $AB_{1-x}O_3$ [4, 8-11].

On the other end it is observed that when the defect energy is high, the cations from A and/or B site occupies the vacant sites to form the equilibrium structure [12]. This is also observed in few extreme cases where the structure avoid creating B-site cation vacancies by filling the octahedral B site vacancies with large cation like Ba^{2+}. There are only few reports in literature on perovskites where large size cation like Ba^{2+} occupies the octahedral B-site viz. $Ba_{2.414}U_{1.554}O_6$ [13], $Ba_{2.5}Bi_{1.5}O_{5.5}$ [14].

In general, non-stoichiometric compounds have intricate crystal structure and difficult to solve. Neutron diffraction provides a powerful technique while analyzing oxygen deficient perovskite structure. But still in many cases the x-ray and neutron diffraction together cannot completely solve the problem and one has to look for other evidences from supporting techniques like electron diffraction, density measurements, thermogravimentry, positron annihilations lifetime spectroscopy, etc [15, 16].

Considering particular examples of complex uranates of the formula A_2REUO_6 (RE= rare earth metals), these compounds were shown to have impurity of RE_2O_3 and does not form perfect stoichiometric phase but have B-site deficiency at RE^{3+} ion (However, in the later chapter we study these phases and have shown to have complete end stoichiometry and uranium exists in +5 oxidation state). Considering the deficiency of RE^{3+}, S. Kemmler-Sack and co-workers explored $A_2RE_{2/3}UO_{5.5}$ compounds where 1/3rd amount of RE was removed but oxidation state of uranium was maintained as +5 [17-22]. The density measurements on these compounds show that they have stoichiometry of $A_{2.18}RE_{0.73}U_{1.09}O_6$ which does not have any deficiency. But later it was shown that this phase on slow oxidation gives $A_2RE_{2/3}UO_6$ phase. Thus it is not clear how $Ba_2RE_{2/3}UO_{5.5}$ ($A_{2.18}RE_{0.73}U_{1.09}O_6$) transforms to $A_2RE_{2/3}UO_6$ compound, as the starting phase is already shown to be stoichiometric and how the excess oxygen is incorporated during the oxidation. Similarly, Kemmler-Sack and co-workers reported number of other such cation deficient perovskite phases with the formulae $A_2B_{2/3}\square_{1/3}B'O_6$, $A_2B_{3/4}\square_{1/4}B'O_6$, $A_2B_{4/5}\square_{1/5}B'O_6$, $A_2B_{5/6}\square_{1/6}B'O_6$ and $A_2B_{7/8}\square_{1/8}B'O_6$ ($\square$ denote cation vacancy) where the B-cation to vacancy ratio varies from 5:1, 7:1, 9:1, 11:1 and 15:1 respectively [23]. Though these compounds are not well characterized and the crystal structure is not known, they form interesting class of perovskite compounds to be studied in detail.

5.2 Issues and scope of work

As discussed above, these $A_2RE_{2/3}M^{5+}O_{5.5}$ types of compounds were not well characterized and the crystal structure was not reported. Also, there is an ambiguity with respect to the vacancies, stoichiometry of the prepared samples and impurity phases formed during the synthesis. In the present work, we have studied compounds with the stoichiometry $Ba_2La_{2/3}MO_{5.5}$ (*called La2/3M henceforth*) and compared the crystal structure with $Ba_2LaM^{5+}O_6$ (M= Nb, Sb, Bi, U) compounds (*called LaM henceforth*). There remains a fair possibility that the synthesized compounds may have cation and anion vacancies. In order to check the presence of cation vacancy in the prepared compounds, samples were investigated using positron annihilation lifetime spectroscopy (PALS). X-ray or neutron diffraction was not sufficient to solve the correct crystal structure. Thus using the PALS technique, correct crystal structure was modelled and was further refined using x-ray and neutron diffraction. Comparison of the local site symmetry around the La atom in LaM and La2/3M compounds is probed by photoluminescence (PL) studies (for M=Nb, Sb compounds) and infrared spectroscopy (IRS) study (for M=Nb, Sb, Bi compounds), where as EXAES technique was used for uranium compound.

5.3 Synthesis

Compounds La2/3M with M=Nb, Sb, and Bi were prepared by gel combustion method. Reactants $Ba(NO_3)_2$ (99.9%), $La(OH)_3$ (99.9%), Nb_2O_5 (99.9%), Sb_2O_3 (99.99%), Bi_2O_3 (99.9%) and Eu_2O_3 (99.9%) were used in the synthesis. All the reactants were dried at 300°C before weighing. The reactants in the form of respective oxides were weighted to have required stoichiometry of 2Ba:2/3La:(Nb/Sb/Bi) and dissolved in concentrated nitric acid. Citric acid with quantity equal to 1.5 molar content of metal ions was added to the solution as a fuel. Reactants like Nb_2O_3 and Sb_2O_3 are not soluble in nitric acid and remain as suspended particles. Finally, the pH of the solution is adjusted by ammonia and solution is dried on a hot plate with continuous stirring to form dry solid precursor powder. This precursor in then slowly heated up to 600°C to remove the unburned carbon. Later, after grinding the mixture is heated at high temperatures with intermittent grindings. Nb and Sb samples were heated up to 1350°C for 60 h while for Bi compound was heated up to 900°C for 50h. For PL studies, 2 at. % Eu was doped at La site in both Ba_2LaMO_6 and $Ba_2La_{2/3}MO_{5.5}$ (M=Nb and Sb) series of compounds. Same synthesis conditions were applied for preparing samples for PL study.

La2/3U compound was prepared by solid state reaction. $BaCO_3$ (99.9%), RE_2O_3 (RE=La, Nd, Sm) (99.9%), $UO_{2.00}$ (99.9%) and UO_3 (99.9%) were mixed in stoichiometric ratio as follows,

$2BaCO_3 + 1/3\ RE_2O_3 + 1/2\ UO_{2.00} + 1/2\ UO_3$

Reactants $BaCO_3$ and RE_2O_3 were pre-dried at 573K and 1073K respectively. $UO_{2.00}$ was freshly prepared by heating U_3O_8 in Ar- 8%H_2 atmosphere at 1073K. UO_3 was prepared by decomposing uranyl nitrate at 623K. This reaction mixture was initially heated at 1173K for 20 h and later heated at 1673K for 20 h in high purity Ar atmosphere (oxygen content ~ 6 ppm). Finally, the compounds were heat treated at 1673K for 60 h in Ar- 8%H_2 atmosphere with several intermittent grinding.

5.4 Results and discussion

The results and discussion related to compounds containing M= Nb, Sb and Bi and M=U are discussed separately in two sections.

Section a: M=Nb, Sb, Bi

5.4.1.a Crystal structure

Fig. 5.1 shows the room temperature XRD pattern for La2/3M compounds. With single A cation the most common space groups are $a^0a^0a^0$ ($Fm\bar{3}m$), $a^-a^-a^-$ ($R\bar{3}$), $a^0a^0c^-$ ($I4/m$), $a^0b^-b^-$ ($I2/m$) and $a^+b^-b^-$ ($P2_1/n$) [24]. The assigning of the space group is inferred from the observation of particular reflections in the XRD pattern corresponding to in-phase and out of-phase tilts [25]. For double perovskite, first the reflections are indexed using double edge primitive cubic cell (a~8 Å). The reflections (hkl)=(odd odd even), correspond to M-point reflections. Presence of M-point reflections is unambiguous indication of in-phase tilting of octahedral. The XRD pattern for La2/3M compounds, show the absence of these M-point reflections ruling out the $a^+b^-b^-$ $(P2_1/n)$ option. Reflection $(400)_p$ is doublet in $I2/m$ while singlet in $R\bar{3}$ and reflection $(444)_p$ is singlet in $I4/m$, but can be doublet in $R\bar{3}$ and triplet in $I2/m$. The insets in Fig. 1 show $(400)_p$ and $(444)_p$ reflections for La2/3M and LaM compounds. From the XRD pattern, it is observed that the La2/3Nb compound adopts $R\bar{3}$ space group with lattice parameters a=6.10509(7)Å, c=14.8643(3)Å which is closely related to reported LaSb (Ba_2LaSbO_6) compound. When La and O vacancy was forcefully incorporated in the crystal structure model, it was observed that the XRD pattern could be fitted only by distributing Ba atom from A site to vacant La site leading to vacancies present in both Ba site and La site. If this non-stoichiometric model is true, then it has to be carefully investigated by other methods.

PALS is a well established technique for probing defects in materials [26]. The propensity of positron to get trapped in low electron density regions like open volume defects or vacancies enables identification of defects in materials. The lifetime of the positron in a material depends on electron density distribution and therefore, can provide information about the trapping sites/defects. When the vacancy defects are present, the average lifetime $\tau_{avg} = \sum \tau_i I_i$, where, τ_i and I_i is lifetime and its intensity in the i^{th} state, is greater than the bulk lifetime of the positron in defect-free material. PALS measurement can provide sub-ppm level sensitivity for defects [27]. PALS technique has been used widely used for probing cation vacancies in perovskites [28-31]. We have employed PALS to investigate the presence of cation vacancies in the LaM and La deficient La2/3M compounds.

Table 5.1 Average positron lifetime (τ_{avg}) in ps for Ba_2LaMO_6 and $Ba_2La_{2/3}MO_{5.5}$

Samples	**Sb**	**Bi**	**Nb**
LaM compound	202 (5)	198 (6)	223 (6)
La2/3M compound	228 (8)	208 (5)	268 (8)

Table 5.1 shows the experimentally obtained average positron lifetime (τ_{avg}) in LaM and La2/3M compounds. The τ_{avg} for LaM compounds is seen to be higher than the reported bulk values in perovskite oxides [28-30]. It indicates the presence of cation vacancies (~ ppm) in the as-prepared LaM compounds. It is reported that the cation vacancies would tend to increase the lifetime by more than 40-60 ps for 6-coordinated B-site monovacancy and 100-150 ps for 12-coordinated A-site monovacancy [31]. Therefore, any additional cation vacancy formed due to the deficiency of La in La2/3M compounds should be reflected in τ_{avg}. In the case of La2/3Sb and La2/3Bi compounds, τ_{avg} changes only by 10-25 ps compared to LaSb and LaBi compounds indicating the absence of any additional B-site vacancy defects as compared to LaM compounds. On the other hand, in the case of La2/3Nb compound, the τ_{avg} increases by ~ 45 ps which can be correlated to the presence of additional La vacancy in La2/3M compound. However, considering the fact that similar other two compounds show no cation vacancies, the increase of lifetime may be due to other reasons. In Nb compounds there are two important differences between LaNb and La2/3Nb compounds; the crystal symmetry is different and the presence of additional anti-site disorder in La2/3Nb compound may create stress and defects in the crystal structure of La2/3Nb. This defects/disorder in the crystal structure might also be responsible for the increase in τ_{avg}. Moreover, as discussed further the good fit of calculated XRD data using vacancy free crystal structure model with the observed data and similar volume per formula unit for LaM and La2/3M compounds supports the absence of B site vacancies. Thus using the PALS technique we can establish

that there is no additional B site vacancy created in La2/3M compound as compared to LaM compound.

From these analyses, it was found that the synthesized La2/3M compounds do not have any significant vacancy to be consistent with the above non-stoichiometric model used in fitting XRD data. Considering the fact that the synthesized La2/3M compounds are pure and single phase, there must be a vacancy free crystal structure model which should satisfy the experimental observations. It has been shown by Kemmler-Sack and co-workers [8, 32] that the perovskite structure can either have vacancies at A or B site, or it may be stabilized by the occupation of B sites by A ions. $Ba_{1+y}UO_{3+x}$ [13], $Sr_2UO_{4.5}$ [33] and $Ca_2UO_{4.5}$ [34] are few examples which can be thought as an extreme end of vacancies with formula $A_2B'\square O_{6-x}$, but such extreme case of vacancy is not stable and structure stabilizes by adopting the second option i.e. occupation of vacant B sites by A ions. Thus in reality $Sr_2UO_{4.5}$ adopts perovskite structure with the formula $Sr_2(Sr_{2/3}U_{1/3})UO_6$. Considering similar possibility in our compounds; the normalized formula for synthesized compounds should be $Ba_{2.18}La_{0.73}Nb_{1.09}O_6$. Here excess of 0.18Ba and 0.09Nb atoms should occupy the vacant La site and have formula $Ba_2(La_{0.727}Ba_{0.182}M_{0.091})MO_6$. These compounds are very rare and novel because large Ba atom occupies octahedral B site to stabilize the structure. Using $R\bar{3}$ space group and above model structure, Rietveld refinement was performed on La2/3Nb XRD data. Despite weak super-lattice reflections corresponding to B site ordering, there is still a noticeable difference between fully ordered and partial anti-site disorder. Thus during the refinement, additional anti-site disorder between La and Nb atom was considered. Such anti-site disorder is missing in LaNb compound. It is interesting to observe that 0.18Ba atom occupying La site and additional anti-site disorder at B site forces crystal symmetry to adopt rhombohedral compared to monoclinic symmetry in LaNb compound.

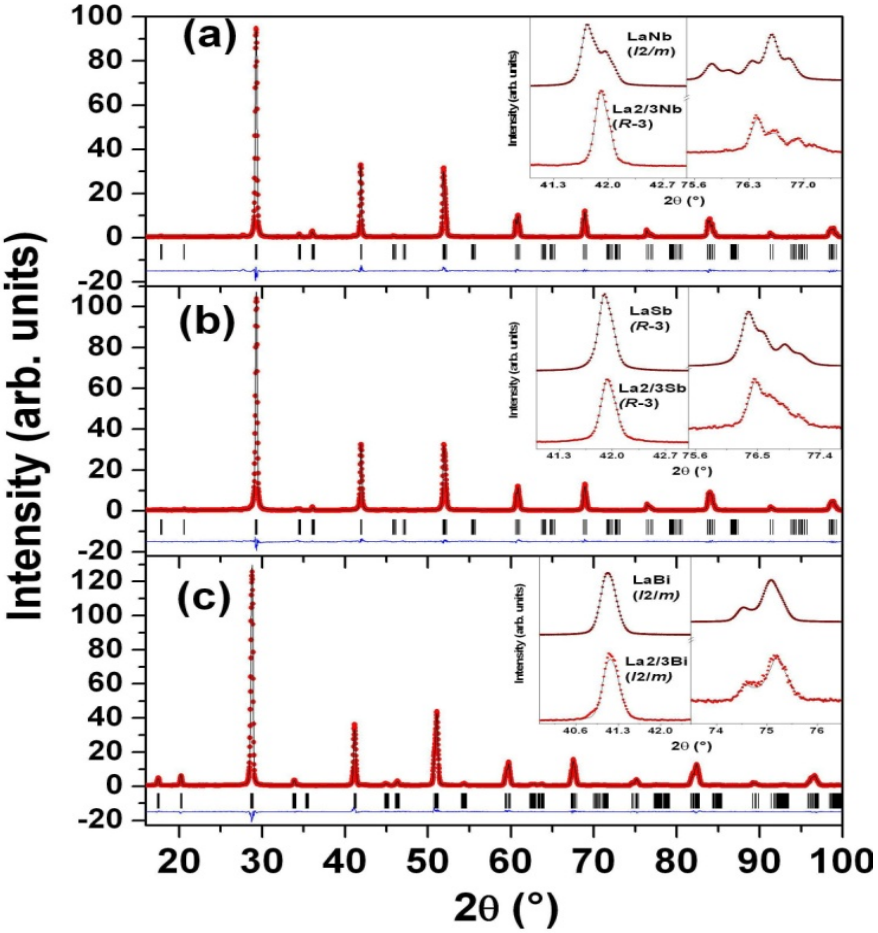

Figure 5.1 *X-ray diffraction Rietveld refinement plot for (a) La2/3Nb (b) La2/3Sb (c) La2/3Bi compounds. Scattered points and line show observed and calculated pattern, respectively. Difference between observed and calculated pattern is shown below in blue. Vertical lines are the Bragg reflection markers. Insets show the comparison of $(400)_p$ and $(444)_p$ reflections between the La2/3M and reported LaM compounds (see the text for details).*

Similar crystal structure refinement was done on La2/3Sb and La2/3Bi compounds. Conversely, it can be observed that crystal symmetry for La2/3Sb and La2/3Bi compounds remains the same as that of compounds LaSb ($R\bar{3}$ space group) and LaBi ($I2/m$ space group), respectively. The crystal structure of compounds La2/3Sb and La2/3Bi are shown in Fig. 5.2. Table 5.2 & 5.3 gives refined crystal structure parameters.

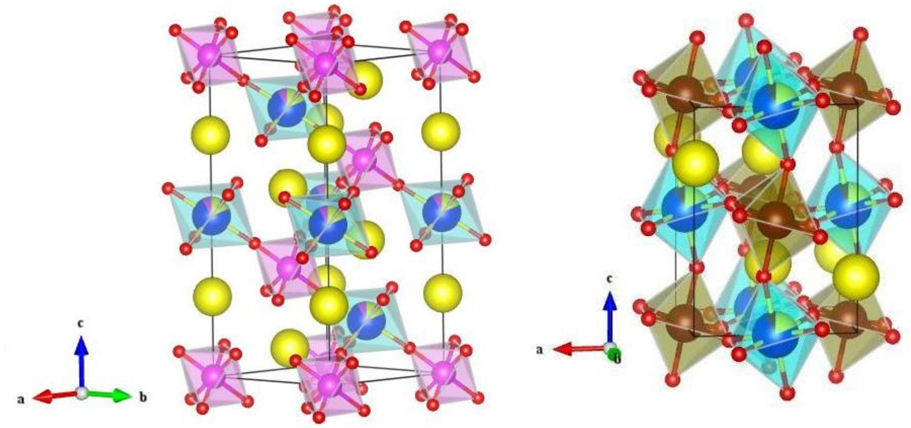

Figure 5.2 *Crystal structure of La2/3Sb (Rhombohedral $R\bar{3}$) and La2/3Bi (Monoclinic $I2/m$) compounds. Colour: Ba-yellow, La-blue, Sb-pink, Bi-brown, oxygen-red. [Structure was drawn using VESTA software: K. Momma and F. Izumi, "VESTA: a three-dimensional visualization system for electronic and structural analysis." J. Appl. Crystallogr., 41:653-658, 2008].*

In contrast to La2/3Nb sample, there was no anti-site disorder observed in the La2/3Sb and La2/3Bi samples. The observed bond lengths <Sb-O> and <Bi-O> in La2/3Sb and La2/3Bi compounds are 1.999Å and 2.151 Å respectively. These values match well with the sum of ionic radii (R_{M5+} +R_{O2-}); with the values 0.6Å, 0.76Å and 1.4Å for 6 co-ordination Sb^{5+}, Bi^{5+} and O^{2-}, respectively. For La2/3Nb compound, bond length <Nb-O>=2.007 is less than expected value of 2.04 (R_{Nb5+}=0.64 Å). Similar results were obtained in Ba_2LnNbO_6 compounds where mean <Nb-O>= 1.99 Å [35]. It is expected that in La2/3M compound local symmetry around the La atom is more distorted as compared to LaM compound due to the occupancy of Ba and M atom at vacant La site. This argument can be further probed by photoluminescence study by doping Eu^{3+} at La^{3+} site and by infrared spectroscopy as discussed ahead.

Table 5.2 Refined crystallographic data for $Ba_2La_{2/3}MO_{5.5}$ (RE=Nb, Sb, Bi) compounds.

Compound	**$Ba_2La_{2/3}NbO_{5.5}$**	**$Ba_2La_{2/3}SbO_{5.5}$**	**$Ba_2La_{2/3}BiO_{5.5}$**
Crystal system	Rhombohedra*	Rhombohedra*	Monoclinic
Space Group	$R\bar{3}$ (148)	$R\bar{3}$ (148)	$I2/m$ (12)
Z	3	3	2
Lattice Parameter (Å and °)	a = 6.10509(7) c = 14.8643(3) β = 120.00	a = 6.10166(9) c = 14.8729(4) β = 120.00	a = 6.2266(2) b = 6.1870(3) c = 8.7479(2) β = 90.300(2)
Volume/formula (Å ^{3})	159.94(1)	159.85(2)	168.50(1)

* Rhombohedral system is represented in standardized hexagonal units.

Table 5.3 Atomic parameters and bond lengths for $Ba_2La_{2/3}MO_{5.5}$ (RE=Nb, Sb, Bi) compounds obtained using refinement of x-ray diffraction data.

Atom	Site	x	y	z	Biso($Å^2$)	Occupancy
$Ba_2La_{2/3}NbO_{5.5}$ (La2/3Nb)						
Ba	6c	0	0	0.249(2)	0.89(4)	1
La/Ba/Nb	3b	0	0	1/2	0.39(4)	0.608/0.182/0.210
Nb/La	3a	0	0	0	0.39(4)	0.881/0.119
O	18f	0.093(1)	0.291(2)	0.084(6)	0.90(7)	1
<Ba-O> = 3.061(6)Å						
<La-O> = 2.358(4)Å						
<Nb-O> = 2.007(4)Å						
$Ba_2La_{2/3}SbO_{5.5}$ (La2/3Sb)						
Ba	6c	0	0	0.2488(2)	0.75(4)	1
La/Ba/Sb	3b	0	0	1/2	0.20(5)	0.72/0.182/0.09
Sb	3a	0	0	0	0.20(5)	1
O	18f	0.103(3)	0.295(2)	0.082(2)	0.91(3)	1
<Ba-O> = 3.058(2)Å						
<La-O> = 2.348(2)Å						
<Sb-O> = 1.999(2)Å						
$Ba_2La_{2/3}BiO_{5.5}$ (La2/3Bi)						
Ba	4i	0.4914(4)	1/2	0.2556(3)	0.41(2)	1
La/Ba/Bi	2c	1/2	0	0	0.20(3)	0.72/0.182/0.09
Bi	2b	0	1/2	0	0.20(3)	1
O1	8j	0.246(2)	0.270(3)	1.050(1)	0.7(2)	1
O2	4i	0.573(4)	0	0.256(3)	0.7(2)	1
<Ba-O> = 3.118(4)Å						
<La-O> = 2.324(4)Å						
<Bi-O> = 2.151(4)Å						

$Ba_2La_{2/3}NbO_{5.5}$: R_{wp}=11.4%, R_p=7.7%, R_B=3.3%, χ^2=1.3

$Ba_2La_{2/3}SbO_{5.5}$: R_{wp}=11.5%%, R_p=7.1%, R_B=2.9%, χ^2=1.5

$Ba_2La_{2/3}BiO_{5.5}$: R_{wp}=9.55%, R_p=6.64%, R_B=3.9%, χ^2=1.5

5.4.2.a Photoluminescence Study (PL)

In the present work, the emission and lifetime characteristics of Eu^{3+} ion in the lattices of $Ba_2LaM^{5+}O_6$ compounds (LaM) and $Ba_2La_{2/3}M^{5+}O_{5.5}$ compounds (La2/3M) have been investigated for M=Nb and Sb samples and the variation of PL signals are correlated with the variation of local coordination around La^{3+} ion. The PL study was not recorded on Bi samples due to their dark brown colour.

Fig. 5.3 shows the excitation spectra of Eu^{3+} ion in the lattices of $Ba_2LaM^{5+}O_6$ (LaM) and $Ba_2(La_{0.727}Ba_{0.182}M_{0.091})MO_6$ (La2/3M) with an emission wavelength of 594 nm; corresponding to $^5D_0$-$^7F_1$ transition of Eu^{3+} ion. The niobium sample spectra display an intense broad band in the spectral range of 230–320 nm peaking at 287 nm corresponds to charge transfer (CT) transitions of $O^{2-} \rightarrow Eu^{3+}$ from filled 2p to vacant 4f orbital. There may be some contribution from $O^{2-} \rightarrow Nb^{5+}$ but the contribution of the O-Eu CT transition is the dominant one. The interesting observation is that $O^{2-} \rightarrow Eu^{3+}$ charge transfer peak in antimony compound (both europium doped La2/3Sb and LaSb) is blue shifted by almost 25 nm relative to niobium compounds.

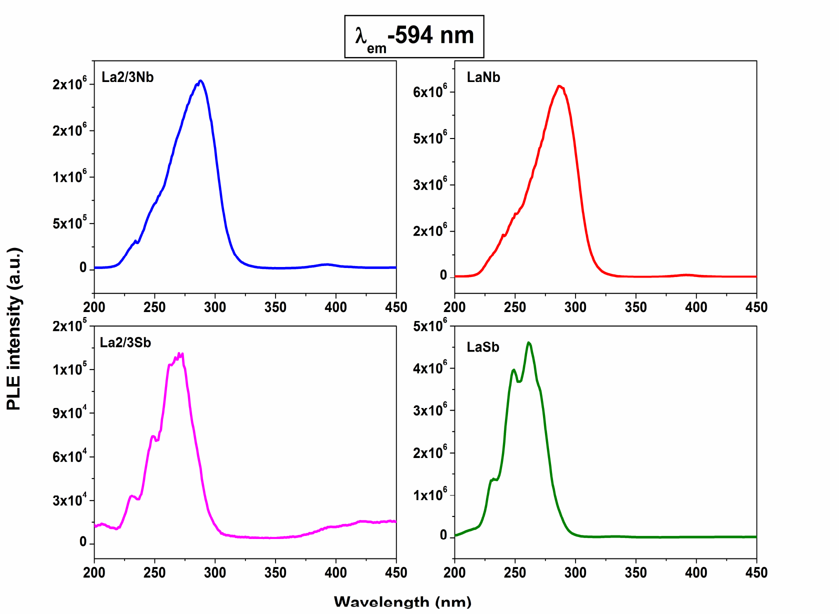

Figure 5.3 *Excitation spectra of Europium doped LaM and La2/3M compounds for M= Nb and Sb.*

It is well known that position and emission intensity of charge transfer band (CTB) are strongly affected by the extent of covalency in O^{2-}-Ln^{3+} bond [36]. In the moiety of Eu^{3+}–

O^{2-}—M^{5+} (M = Nb and Sb), the covalent character in Eu^{3+}–O^{2-} bond is relatively weaker in europium doped La2/3Sb and LaSb because of higher electronegativity of pentavalent antimony ion compared to niobium ion. So, it is easier for the electron from O-2p state to get transferred to Eu 4f state in europium doped La2/3Nb and LaNb host than that in europium doped La2/3Sb and LaSb. As a result, charge transfer energy is higher in europium doped La2/3Sb and LaSb and is blue shifted.

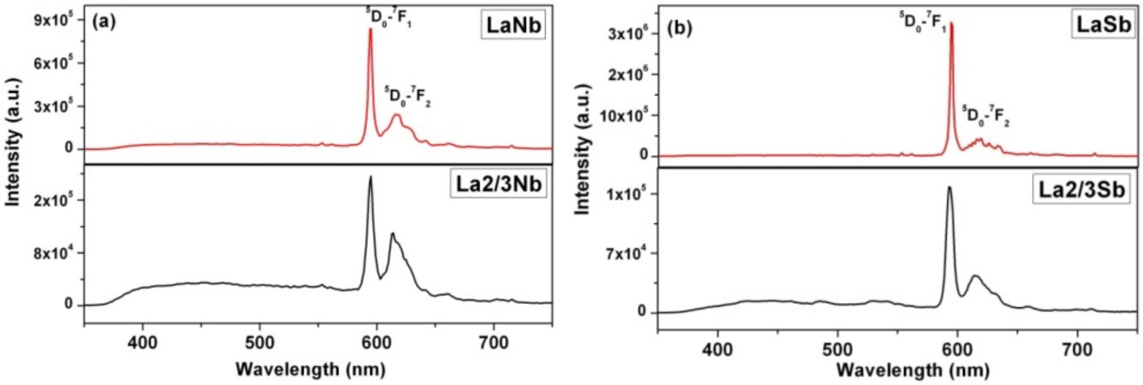

Figure 5.4 *Emission spectra of Europium doped LaM and La2/3M compounds for (a) M= Nb λex-287 nm and (b) Sb, λex-260 nm.*

Upon excitation at 287 nm (charge transfer band; CTB in case of M=Nb^{5+}), the emission spectrum (Fig. 5.4a) exclusively contains the strong bands of $^5D_0\rightarrow^7F_1$ (591 nm), $^5D_0\rightarrow^7F_2$ (616 nm) and very feeble peaks due to $^5D_0\rightarrow^7F_3$ (651 nm) and $^5D_0\rightarrow^7F_4$ (697 nm). The fact that asymmetry ratio (EDT/MDT) is larger in case of La2/3Nb (~ 0.58) compared to LaNb compound (~ 0.29) is an indication of the fact that local symmetry around europium in case of La2/3Nb compound is low compared to LaNb compound in case of niobium sample. Though crystal symmetry wise La2/3Nb is rhombohedral which is more symmetric than monoclinic for LaNb, the PL study shows that local symmetry around La is more distorted in La2/3Nb compound. A similar situation is seen in the case of antimony compounds (Fig. 5.4b). Here also asymmetry ratio (EDT/MDT) is larger in case of La2/3Sb (~ 0.29) compared to LaSb (~0.15). Interestingly, here both the compound has same space group but still displaying more distorted symmetry around La in the case of La2/3Sb compound. This fact is in agreement with our crystal structure model which states that in La2/3M compound, vacant La site is occupied by Ba and M atoms which create additional distortion at La site.

On comparison of emission spectra, it can be seen that ratio of MDT/EDT is more in antimony sample compared to niobium sample bring the take home message that europium is having higher local symmetry in antimony based sample compared to niobium one. This pinpoints that though La2/3Nb and La2/3Sb have same space group with close lattice parameters, replacing Nb^{5+} with higher electronegativity of Sb^{5+} ion; europium occupies a more symmetric environment.

Observed fact is also corroborated using Judd-Ofelt parameter analysis. Judd-Ofelt (JO) intensity parameters, Ω_J (J = 2, 4) calculated using Judd-Ofelt theory [37, 38], provide information about the local environment and bonding in the proximity of lanthanide ion. Ω_2 represent short range ordering gives the information on the degree of covalency and polarizability which can be indirectly correlated to local chemical environment experienced by the Ln^{3+} ion in a host whereas Ω_4 represent long range ordering is related to the bulk properties such as viscosity and rigidity of the inorganic matrices [39].

In the case of europium doped La2/3Nb and LaNb as well as La2/3Sb and LaSb sample the value of Ω_4 is greater than Ω_2 which indicates that overall europium possess a highly symmetric environment in all the samples. This is also reflected by the fact that magnetic dipole transition dominates electric dipole transition in the emission spectrum. But their respective value is different in niobium and antimony samples. The $(\Omega_4/\ \Omega_2)_{Nb}$ is less than $(\Omega_4/\ \Omega_2)_{Sb}$ clearly supports our emission spectroscopy that europium has higher symmetry in antimony sample compared to niobium sample.

It could also be seen from Fig. 4 that emission spectra of La2/3M displayed broad emission in both the sample in the range 400 -530 nm which can be attributed to host emission. But the extent of host-dopant energy transfer (HDET) is different in both the sample. The efficiency of HDET is more in LaM samples. This is clearly evident from the presence of substantial host emission band along with Eu^{3+} spectral features in europium doped lanthanum deficient sample. This is the very tricky scenario and extremely difficult to interpret because dopant ion is same, the level of doping is 2.0 at. % in both the host matrix and synthesis conditions are exactly identical, but still, Eu^{3+} display different emission characteristics in lanthanum rich and deficient sample. Also, overall HDET efficiency is more in antimony sample compared to niobium one.

The lifetime value of europium ion doped LaM and La2/3M (M=Nb and Sb) compounds display monoexponential behaviour which indicated homogenous environment for europium ion in all the samples (Fig. 5.5). In the case of the niobium, LaNb compound has slightly higher lifetime (2.67 ms) compared to La2/3Nb compound (2.31 ms). This is because of the fact that asymmetry around europium is more in La2/3Nb sample. There for Laporte’s rules for f-f transitions get relaxed; f-f transition will be faster and consequently lifetime will be less. Similarly, europium has higher luminescence lifetime for La2/3Sb sample (1.33 ms) compared to LaSb sample (1.58 ms). This is also justified by the same above argument.

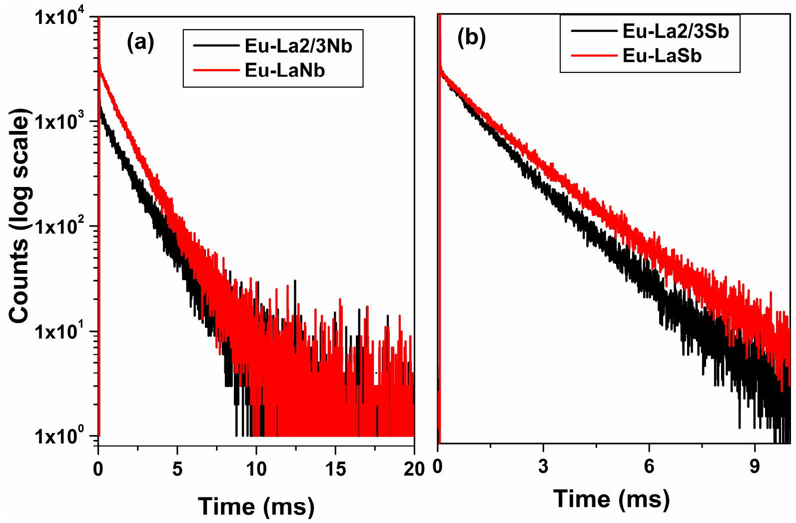

Figure 5.5 *Luminescence decay profile of Europium doped LaM and La2/3M compounds for (a) M= Nb* λ_{ex}*-287 nm and (b) Sb,* λ_{ex}*-260 nm under emission wavelength of 594 nm.*

It can be seen from the emission spectrum that in both the cases LaM compound has higher intensity compared to La2/3M com-pound which can be easily seen from the emission spectrum and the best one in terms of emission output is LaSb sample. This may be correlated to the fact there are more non-radiative pathways for de-excitation in LaNb / La2/3Nb compared to LaSb / La2/3Sb.

5.4.3.a Infrared Spectroscopy (IRS)

Fig. 5.6, shows the room temperature recorded IR spectra for La2/3M and LaM compounds. Fig. 5.6a compares the IR spectra for La2/3M compound in the frequency region 500 to 4000 cm^{-1}. It is observed that IR spectra match well with the IR spectra reported for the perovskites having Nb^{5+}, Sb^{5+} and Bi^{5+} [40-45]. Generally, for ABO_3 perovskite, the IR spectrum is dominated by vibrations corresponding to BO6 octahedra which give rise to absorption bands in the region 400 to 800cm^{-1}. These bands are assigned to the antisymmetric stretching and deformational modes of the octahedral BO6 octahedra [46]. However, in reality, the vibration spectra are much more complex and it has been shown that vibration modes correspond to coupled complex atomic vibrations and cannot be assigned only to a single type of BO6 vibration, like external, bending, or stretching modes [47-49]. Thus in the present compounds the major band corresponds to vibration modes of both the La/MO6 octahedra. From the inset of the Fig. 5.6a it is observed that the band is shifted to higher frequency in the Sb compounds. This observation is consistent with charge transfer peak in photo-excitation spectra and can be explained with the same reason of high electronegativity of Sb^{5+} as compared to Nb^{5+} and Bi^{5+}.

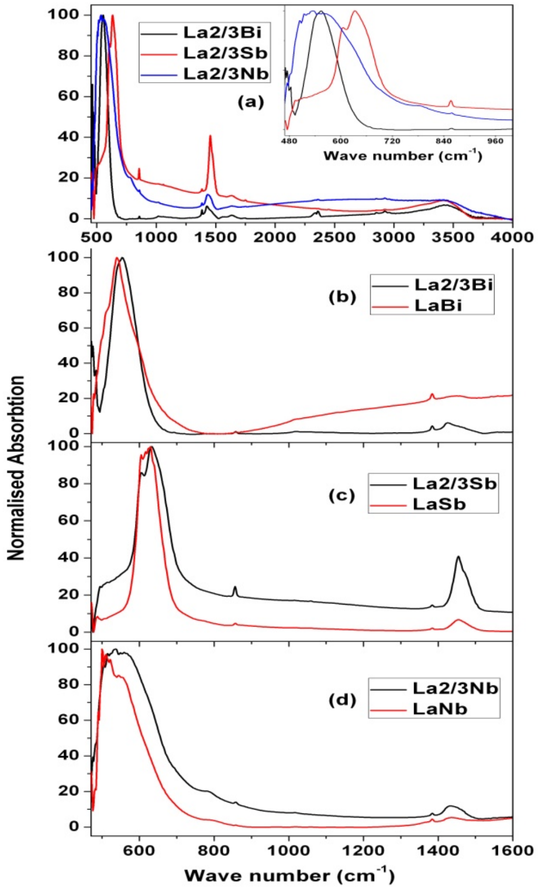

Figure 5.6 *(a) IR spectra for La2/3M compounds; inset shows the enlarged region from 470 to 1000 cm^{-1}. (b, c, d) shows comparison of IR spectra of LaM and La2/3M compounds for M=Bi, Sb, Nb respectively.*

From the Fig. 5.6 b, c, d it is clearly seen that bandwidth corresponding to La/MO6 vibration is large in La2/3M compounds than LaM compounds. This observation confirms that the local site symmetry of La/MO6 octahedra in La2/3M compounds is more distorted as compared to LaM compounds. Moreover, as reported by Wenjun Zheng et.al. [42], we observe weak band at ~ 855cm^{-1} in IR spectra of Sb samples. This weak band is assigned to υ1 mode of octahedral vibration which is IR inactive. The presence of this IR inactive band indicates the lowering of the site symmetry. Interestingly, the increase in the absorption of this mode for La2/3Sb compound as compared to LaSb compound (Fig. 5.6c) indicates more distorted site symmetry in La2/3Sb compound. This is in agreement with our previous conclusion drawn from PL study and once again unequivocally confirms that our crystal structure model for La2/3M compound is correct.

Section b: M= U^{5+}

5.4.1.b Crystal Structure

Top of Fig. 5.7 shows the room temperature XRD pattern for La2/3U compound. The pattern clearly indicates the rock-salt cation ordering at B-site. The XRD pattern was indexed using monoclinic system. The presence of reflections corresponding to in-phase tilting of octahedra (see inset of Fig. 5.7) confirms the $P2_1/n$ space group (with Glazer notation $a^+b^-b^-$) for La2/3U compound. Additionally, for La2/3U compound neutron diffraction (NPD) data was collected in the 2θ range 10-130°, using neutrons of wavelength λ=1.2443Å. Bottom pattern in Fig 5.7 shows the room temperature neutron diffraction pattern for La2/3U compound. The reflections due to in-phase tilting of the octahedral are comparatively strong in NPD as compared to the XRD and confirm the $P2_1/n$ space group.

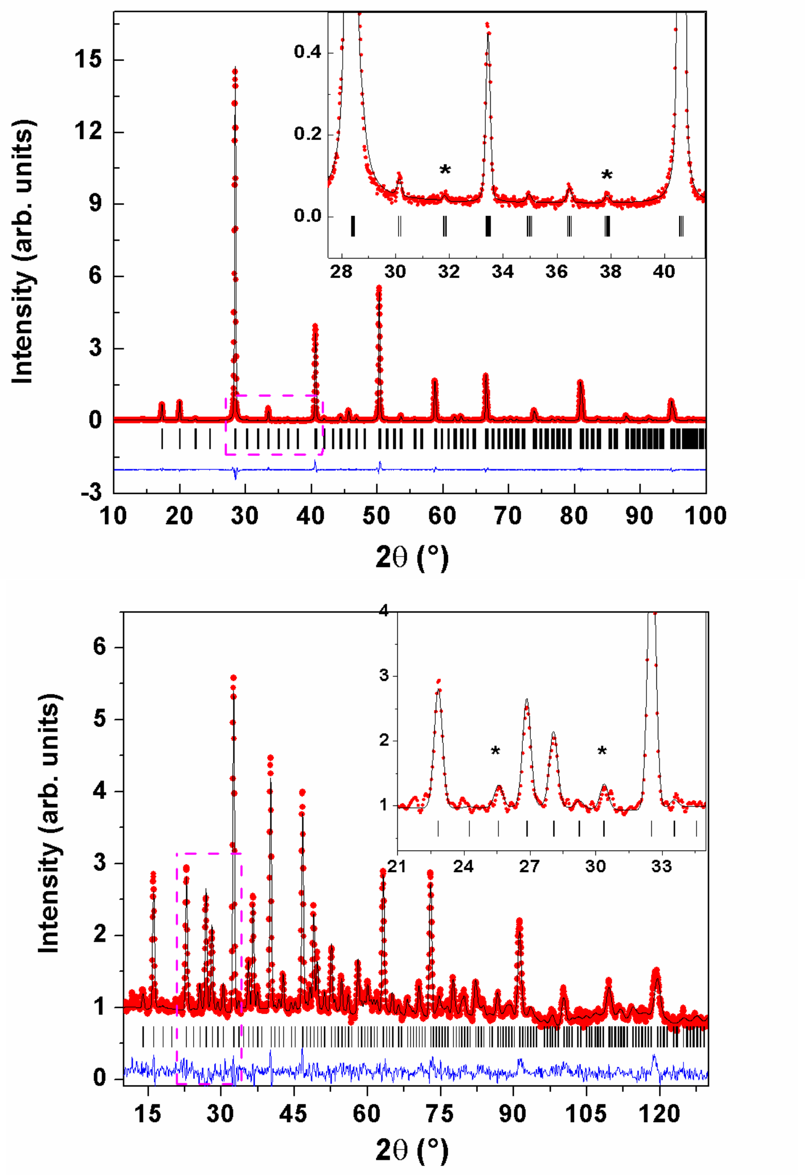

Figure 5.7 *X-ray diffraction (top) and Neutron diffraction (bottom) Rietveld refinement plot for La2/3U. Solid circles in red, continuous line in black and lower continuous line in blue show observed pattern and calculated pattern and difference plot, respectively. Vertical lines show Bragg reflections. The inset shows enlarged section of the pattern in the box where reflection marked by '*' sign indicates the presence of in-phase tilting of octahedra.*

Table 5.4 Refined crystallographic data for $Ba_2La_{2/3}UO_{5.5}$ compound.

$Ba_2La_{2/3}UO_{5.5}$ (La2/3U)

Crystal system: Monoclinic, space group: $P2_1/n$, Z=2

Lattice parameters (Å and °): a=6.2826(3), b=6.2863(2), c=8.8799(3), β=89.870(2),

Volume/formula (Å^3)=175.35(2)

Atom	**Site**	**x**	**y**	**z**	**Biso(Å^2)**	**Occupancy**
Ba	4e	0.4955(9)	0.5228(2)	0.2389(3)	0.34(5)	1
La/Ba/U	2c	0	1/2	0	0.10(4)	0.727/0.182/0.091
U	2d	1/2	0	0	0.21(4)	1
O1	4e	0.304(3)	0.286(4)	0.043(2)	0.51(7)	1
O2	4e	0.237(3)	0.790(5)	0.049(3)	0.51(7)	1
O3	4e	0.580(3)	-0.0208(2)	0.233(3)	0.51(7)	1

<Ba-O> = 3.17(6)Å

<La-O> = 2.41(4)Å

<U-O> = 2.15(4)Å

R_{wp}=9.5%, R_p=6.6%, R_B=3.9%, χ^2=1.3

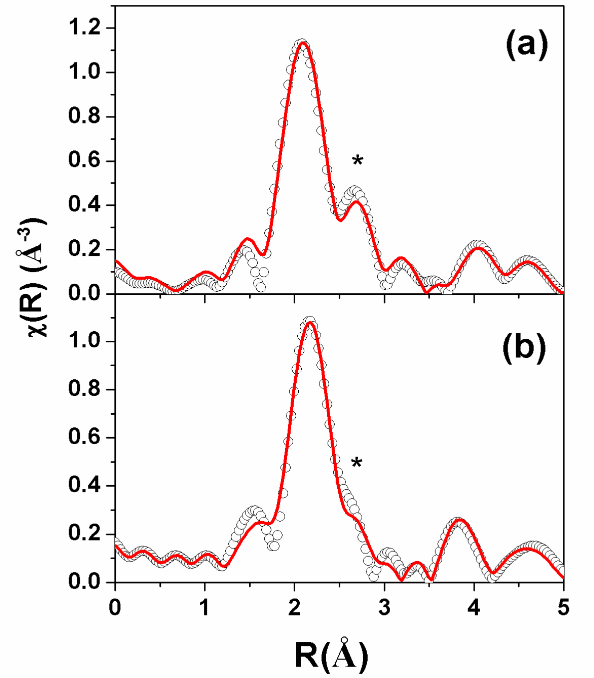

Figure 5.8 *Radial distribution function from the k^2-weighted EXAFS spectra (open circles) of a) $Ba_2La_{2/3}UO_{5.5}$ and b) Ba_2LaUO_6 and its simulated fit (solid line). The highest peak corresponds to U-O distance and peak marked with asterisk sign '*' indicates the U-La distance.*

Interestingly in the case of uranium, La2/3U compound shows very similar XRD and neutron diffraction patterns as compared to Ba_2LaUO_6 compound (discussed in the next chapter). Thus it can be interpreted that with starting stoichiometry of $Ba_2La_{2/3}UO_{5.5}$, it can form Ba_2LaUO_6 compound along with other impurities containing Ba and U according to the equation:

$$3 \text{ x } (2Ba + 2/3La + U) \rightarrow 2 \text{ x } (2Ba + La + U) + (2Ba + U)$$

But the XRD pattern shows absence of any impurity phase and thus the compound with starting stoichiometry $Ba_2La_{2/3}UO_{5.5}$ forms pure phase. Rietveld refinement analysis of XRD and NPD of La2/3U is not sufficient to correctly describe the structure model. It was observed that both the models with and without lanthanum and oxygen deficiency, could equally fit the XRD and NPD and thus other techniques are necessary to know the exact structure. Extended X-ray absorption fine structure (EXAFS) is a unique and very sensitive technique for studying the local structure around the probing atom. Here, in this study EXAFS measurements were performed on uranium L_3 edge. Fig. 5.8 (a) and (b) shows the radial distribution function obtained from k^2-weighted EXAFS spectra for $Ba_2La_{2/3}UO_{5.5}$ (La2/3U) and Ba_2LaUO_6 (LaU) compounds, respectively. The maximum peaks correspond to short U-O distance. The second peak marked with '*' correspond to longer U-O distance. As discussed in the next chapter, the compound LaU show B-cation ordering and thus majorly have only single U-O distance. In contrast, La2/3U compound have considerable amount of long distance U-O distance. This indicates that U is distributed over two sites. Considering the same structure model described in the 'section a' for other La2/3M phases, Rietveld refinement was carried out for La2/3U compound. Considering two different positions for uranium atom, anti-site disorder was incorporated leading to good fit for observed and calculated XRD and NPD patterns as shown in the Fig. 5.7. The refined structural parameters are given in the table 5.4. The partial occupancy of Ba and La ions at U site due to anti-site disorder causes increase of U-O distance as observed in the EXAFS study. Thus both the bulk and the local crystal structures are in complete agreement.

5.4.2.b Thermal study

Fig. 5.9 shows the thermogram of La2/3U compound recorded in air up to 1000°C. The weight gain is due to the oxidation of uranium. The observed percentage weight gain of 1.14% closely matches with the calculated weight gain of 1.15% for oxidation of U^{5+} to U^{6+} according to the equation:

$Ba_2La_{2/3}U^{5+}O_{5.5}$ (La2/3U) $\rightarrow$ $Ba_2La_{2/3}U^{6+}O_6$

The oxidized end product has bright orange color as compared to initial light brown color due to oxidation of U^{5+} to U^{6+}. The XRD pattern (see Fig. 5.10) shows presence of XRD peaks similar to the starting compound along with additional impurities. The XRD peaks similar to the starting compound shifted to the higher 2θ values, indicating the contraction of lattice due to oxidation of uranium. Additionally La2/3U compound was separately heated at low temperature of 300°C for longer duration of 50h in furnace. The XRD pattern for this resulted end product matches with that of oxidized end product in thermogravimetry experiment. Presence of impurities in oxidized end products shows that the phase $Ba_2La_{2/3}U^{6+}O_6$ is not pure and homogeneous.

Thermogravimetric analysis and XRD analysis of the La2/3U compound clearly indicates that La2/3U compound has stoichiometric formula $Ba_2(La_{0.727}Ba_{0.182}U_{0.091})UO_6$, where there is no cation or anion vacancies. This formula indicates that there is no additional space for the oxygen to be introduced in the lattice and thus during oxidation the parent phase decomposes. Thus the current study doubt about the purity of $A_2B_{2/3}B'O_6$ compounds reported by S. Kemmler-Sack and co-workers [18] and needs to be verified for other compounds with B’=Te^{6+}, W^{6+}.

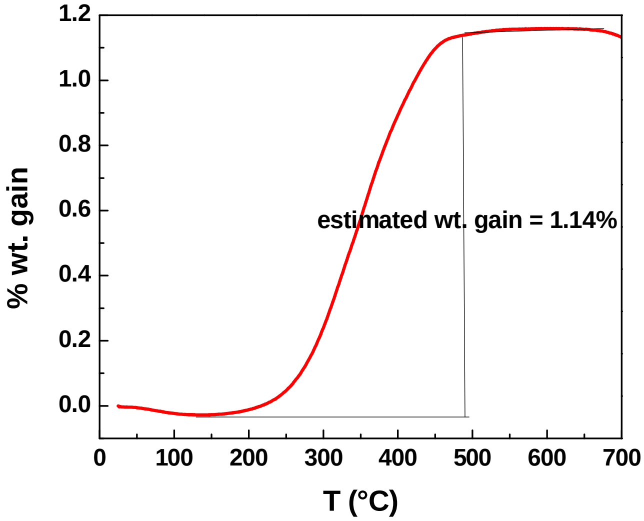

Figure 5.9 *Thermogram of* $Ba_2La_{2/3}UO_{5.5}$ *compound in air, showing percentage weight gain with temperature.*

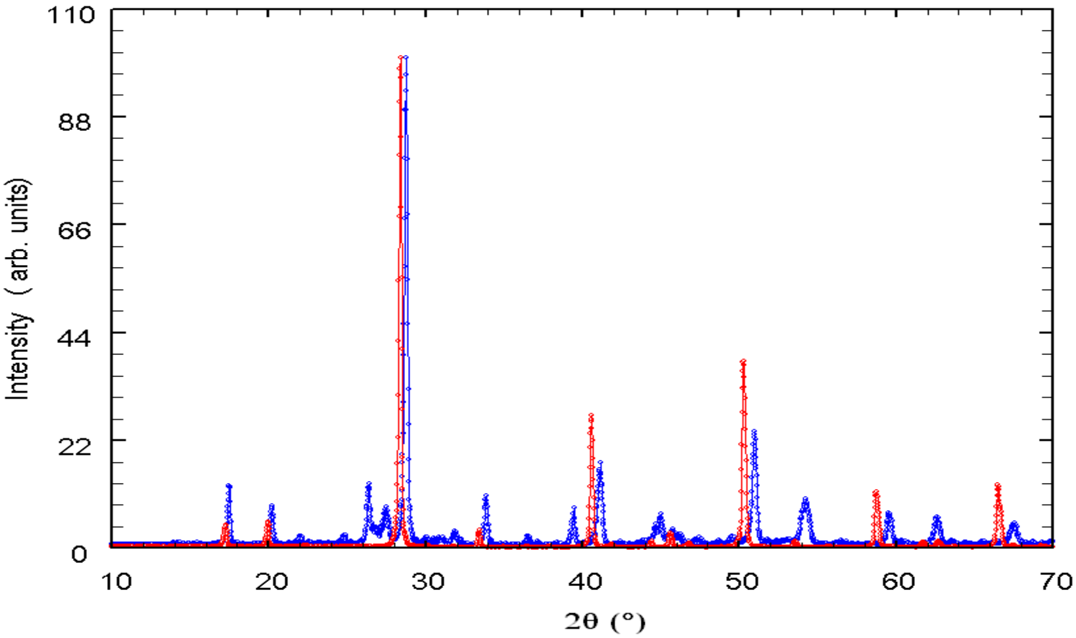

Figure 5.10 *XRD pattern of* $Ba_2La_{2/3}UO_{5.5}$ *(red) and oxidized end product (blue). The oxidized end product shows presence of additional impurities.*

5.5 Conclusions

In this chapter we have synthesized single phase double perovskites with the stoichiometry $Ba_2La_{2/3}M^{5+}O_{5.5}$ (M =Nb, Sb, Bi and U). The crystal structure model was proposed for these phases and was compared with the Ba_2LaMO_6 compounds. According to PALS analysis there is no change in the positron life-time for $Ba_2La_{2/3}M^{5+}O_{5.5}$ as compared to Ba_2LaMO_6 compounds indicating that there is no cation deficiency present in the unit cell. Considering this fact, model structure corresponding to the formula $Ba_2(La_{0.727}Ba_{0.182}M_{0.091})MO_6$ was considered for the refinement of the bulk structure using diffraction data. Other techniques like photoluminescence and IR-spectroscopy are shown to be in agreement with the crystal structure model. Similarly, crystal structure of $Ba_2La_{2/3}UO_{5.5}$ was solved using XRD, NPD and EXAFS studies. The therogravimetric analysis shows that $Ba_2La_{2/3}UO_6$ compound does not form and it confirms our proposed structure for these phases with the formula $Ba_2(La_{0.727}Ba_{0.182}M_{0.091})MO_6$ which does not have cation or oxygen vacancies.

5.6 References

[1] K.R. Kendall, C. Navas, J.K. Thomas, H.-C.z. Loye, Recent developments in perovskite-based oxide ion conductors, Solid State Ionics, **82,** (1995), p. 215.
[2] M. Backhaus-Ricoult, SOFC – A playground for solid state chemistry, Solid State Sciences, **10,** (2008), p. 670.
[3] S. Stolen, E. Bakken, C.E. Mohn, Oxygen-deficient perovskites: linking structure, energetics and ion transport, Physical Chemistry Chemical Physics, **8,** (2006), p. 429.
[4] E.V. Antipov, A.M. Abakumov, S.Y. Istomin, Target-Aimed Synthesis of Anion-Deficient Perovskites, Inorganic Chemistry, **47,** (2008), p. 8543.
[5] M.T. Anderson, J.T. Vaughey, K.R. Poeppelmeier, Structural similarities among oxygen-deficient perovskites, Chemistry of Materials, **5,** (1993), p. 151.
[6] M.A. Peña, J.L.G. Fierro, Chemical Structures and Performance of Perovskite Oxides, Chemical Reviews, **101,** (2001), p. 1981.
[7] T.V. Choudhary, S. Banerjee, V.R. Choudhary, Catalysts for combustion of methane and lower alkanes, Applied Catalysis A: General, **234,** (2002), p. 1.
[8] H.J. Rother, S. Kemmler-Sack, U. Treiber, W.R. Cyris, Über hexagonale Perowskite mit Kationenfehlstellen. XXI. Die Struktur von $Ba_4Nb_2W\text{ʎ}O_{12}$ und $Ba_3LaNb_3\text{ʎ}O_{12}$, Zeitschrift für anorganische und allgemeine Chemie, **466,** (1980), p. 131.

[9] D.J.W. Ijdo, R.B. Helmholdt, $Ba_2Ce_{3/4}SbO_6$, a Rietveld refinement of neutron powder diffraction data, Acta Crystallographica Section C, **49,** (1993), p. 652.

[10] B.J. Kennedy, C.J. Howard, Y. Kubota, K. Kato, Phase transition behaviour in the A-site deficient perovskite oxide $La_{1/3}NbO_3$, Journal of Solid State Chemistry, **177,** (2004), p. 4552.

[11] D.J.W. Ijdo, W.T. Fu, S. Akerboom, Crystal structure of $Ba_9La_2W_4O_{24}$ and $Sr_9Gd_2W_4O_{24}$: A new B-site vacancy ordered 4×4×4 cubic perovskite, Journal of Solid State Chemistry, **238,** (2016), p. 236.

[12] R.G.J. Ball, Computer simulation studies of ternary uranate phases with alkali and alkaline-earth metals. Part 1.-MUO_3, Journal of Materials Chemistry, **2,** (1992), p. 641.

[13] E.H.P. Cordfunke, A.S. Booij, V. Smit-Groen, P. van Vlaanderen, D.J.W. Ijdo, Structural and Thermodynamic Characterization of the Perovskite-Related $Ba_{1+y}UO_{3+x}$ and $(Ba, Sr)_{1+y}UO_{3+x}$ Phases, Journal of Solid State Chemistry, **131,** (1997), p. 341.

[14] K.P. Reis, A.J. Jacobson, J.M. Nicol, A Powder Neutron Diffraction Investigation of Structure and Cation Ordering in $Ba_{2+x}Bi_{2-x}O_{6-y}$, Journal of Solid State Chemistry, **107,** (1993), p. 428.

[15] R. Xu, Y. Xu, Modern Inorganic Synthetic Chemistry, Elsevier Science (2017).

[16] O.T. Soerensen, Nonstoichiometric Oxides, Elsevier Science (2012).

[17] S. Kemmler-Sack, I. Hofelich, Über Perowskitphasen in den Systemen $BaO–SE_2O_3–UO_{2+x}$ mit SE = Seltene Erden, La und Y. II. Verbindungen der Zusammensetzung $Ba_2(SE_{0.67}U_{0.33})UO_{6.17}$, Zeitschrift für anorganische und allgemeine Chemie, **388,** (1972), p. 29.

[18] S. Kemmler-Sack, Über Perowskitphasen in den Systemen $AO\text{-}SE_2O_3\text{-}UO_{2.x}$ mit A = Erdalkali und SE = Seltene Erden, La und Y. IV. Verbindungen der Zusammensetzung $Sr_2SE_{0,67}UO_{5,5}$ und $Sr_2SE_{0,67}UO_6$, Zeitschrift für anorganische und allgemeine Chemie, **402,** (1973), p. 232.

[19] S. Kemmler-Sack, Über Perowskitphasen in den Systemen $AO–SE_2O_3–UO_{2,x}$ mit A = Erdalkali und SE = Seltene Erden. La sowie Y. V. Über den Existenzbereich der Perowskitphasen $A_2SEU^VO_6$, Zeitschrift für anorganische und allgemeine Chemie, **402,** (1973), p. 255.

[20] H.J. Schittenhelm, S. Kemmler-Sack, Über Perowskitphasen des Systems $Ba_2Y_{0,67}U_{1−x}W_xO_6$, Zeitschrift für anorganische und allgemeine Chemie, **424,** (1976), p. 211.

[21] W. Wischert, H.J. Schittenhelm, S. Kemmler-Sack, Über Das System $Ba_2Gd_{2/3}\square_{1/3}U_{1−x}W_xO_6$ sowie hexagonale Perowskite vom 18-, Zeitschrift für anorganische und allgemeine Chemie, **439,** (1978), p. 250.

[22] G. Rauser, S. Kemmler-Sack, Über Geordnete Perowskite mit Kationenfehlstellen. II. Der Ersatz von UVI durch NbV in $Ba_2Gd_{0,67}\square_{0,33}UO_6$, Zeitschrift für anorganische und allgemeine Chemie, **439,** (1978), p. 237.

[23] G. Rauser, S. Kemmler-Sack, Über geordnete Perowskite mit Kationenfehlstellen. V. Verbindungen der Zusammensetzung $A_2^{2+}B^{3+}U^{6+56}\square_{16}O_6$, Journal of Solid State Chemistry, **33,** (1980), p. 135.

[24] S. Vasala, M. Karppinen, $A_2B'B''O_6$ perovskites: A review, Progress in Solid State Chemistry, **43,** (2015), p. 1.

[25] C.J. Howard, B.J. Kennedy, P.M. Woodward, Ordered double perovskites - a group-theoretical analysis, Acta Crystallographica Section B, **59,** (2003), p. 463.

[26] R.W. Siegel, Positron Annihilation Spectroscopy, Annual Review of Materials Science, **10,** (1980), p. 393.

[27] R. Krause-Rehberg, H.S. Leipner, Positron Annihilation in Semiconductors: Defect Studies, Springer (1999).

[28] D.J. Keeble, S. Singh, R.A. Mackie, M. Morozov, S. McGuire, D. Damjanovic, Cation vacancies in ferroelectric $PbTiO_3$ and $Pb(Zr,Ti)O_3$: A positron annihilation lifetime spectroscopy study, Physical Review B, **76,** (2007), p. 144109.

[29] R.A. Mackie, S. Singh, J. Laverock, S.B. Dugdale, D.J. Keeble, Vacancy defect positron lifetimes in strontium titanate, Physical Review B, **79,** (2009), p. 014102.

[30] R.A. Mackie, A. Peláiz-Barranco, D.J. Keeble, Vacancy defects in $PbTiO_3$ and lanthanide-ion-doped $PbTiO_3$: A study of positron lifetimes, Physical Review B, **82,** (2010), p. 024113.

[31] D.J. Keeble, S. Wicklein, R. Dittmann, L. Ravelli, R.A. MacKie, W. Egger, Identification of A- and B-site cation vacancy defects in perovskite oxide thin films, Physical Review Letters, **105,** (2010), p. 226102.

[32] S. Kemmler-Sack, I. Seemann, Über Perowskitphasen in den Systemen AO–SE_2O_3–$UO_{2,x}$ mit A = Erdalkali und SE = Seltene Erden, La sowie Y. VII. Die Systeme $Sr_2(SE_{1-3x}Sr_{2x}U^{v}\square x)\ U^{v}O_6$ und $Sr_{2,67-y}Ca_yU^{v}\square_{1,33}O_6$, Zeitschrift für anorganische und allgemeine Chemie, **409,** (1974), p. 23.

[33] E.H.P. Cordfunke, D.J.W. Ijdo, $Sr_2UO_{4.5}$: A New Perovskite-Type Strontium Uranate, Journal of Solid State Chemistry, **109,** (1994), p. 272.

[34] J. Holc, D. Kolar, The thermal stability of calcium uranates in a hydrogen atmosphere, Journal of Solid State Chemistry, **47,** (1983), p. 98.

[35] P.J. Saines, B.J. Kennedy, M.M. Elcombe, Structural phase transitions and crystal chemistry of the series $Ba_2LnB'O_6$ (Ln=lanthanide and B′=Nb^{5+} or Sb^{5+}), Journal of Solid State Chemistry, **180,** (2007), p. 401.

[36] R. Phatak, S.K. Gupta, K. Krishnan, S.K. Sali, S.V. Godbole, A. Das, Crystallographic site swapping of La^{3+} ion in BaA'LaTeO6 (A' = Na, K, Rb) double perovskite type compounds: diffraction and photoluminescence evidence for the site swapping, Dalton Transactions, **43,** (2014), p. 3306.

[37] B.R. Judd, Optical Absorption Intensities of Rare-Earth Ions, Physical Review, **127,** (1962), p. 750.

[38] G.S. Ofelt, Intensities of Crystal Spectra of Rare Earth Ions, The Journal of Chemical Physics, **37,** (1962), p. 511.

[39] R. Shukla, S.K. Gupta, V. Grover, V. Natarajan, A.K. Tyagi, The role of reaction conditions in the polymorphic control of Eu^{3+} doped $YInO_3$: structure and size sensitive luminescence, Dalton Transactions, **44,** (2015), p. 10628.

[40] A.E. Lavat, E.J. Baran, IR-spectroscopic characterization of $A_2BB'O_6$ perovskites, Vibrational Spectroscopy, **32,** (2003), p. 167.

[41] R. Mukherjee, B. Ghosh, S. Saha, C. Bharti, T.P. Sinha, Structural and electrical transport properties of a rare earth double perovskite oxide: Ba_2ErNbO_6, Journal of Rare Earths, **32,** (2014), p. 334.

[42] W. Zheng, W. Pang, G. Meng, Hydrothermal synthesis and characterization of perovskite-type Ba_2SbMO_6 (M=In, Y, Nd) oxides, Materials Letters, **37,** (1998), p. 276.

[43] C. Vijayakumar, H.P. Kumar, S. Solomon, J.K. Thomas, P.R.S. Wariar, A. John, FT-Raman and FT-IR vibrational spectroscopic studies of nanocrystalline Ba_2RESbO_6 (RE = Sm, Gd, Dy and Y) perovskites, Journal of Alloys and Compounds, **480,** (2009), p. 167.

[44] M.A. Subramanian, Ordered Perovskites Containing Pentavalent Bismuth: $Ba(Bi_{0.75}M_{0.25})O_3$ and $Ba(Bi_{0.67}M_{0.33})O_3$, Journal of Solid State Chemistry, **111,** (1994), p. 134.

[45] S. Feraru, A.I. Borhan, P. Samoila, G.G. Nedelcu, A.R. Iordan, M.N. Palamaru, Influence of A-site Cation on Structure and Dielectric Properties in A_2DyBiO_6 (A = Mg, Ca, Sr, Ba) Double Perovskites, Australian Journal of Chemistry, **67,** (2014), p. 250.

[46] S.D. Ross, Inorganic infrared and Raman spectra, McGraw-Hill (1972).

[47] R. Sopracase, G. Gruener, E. Olive, J.-C. Soret, Infrared study of the phonon modes in $PrMnO_3$ and $CaMnO_3$, Physica B: Condensed Matter, **405,** (2010), p. 45.

[48] R. Ratheesh, H. Sreemoolanadhan, M.T. Sebastian, Vibrational Analysis of $Ba_{5-x}Sr_xNb_4O_{15}$ Microwave Dielectric Ceramic Resonators, Journal of Solid State Chemistry, **131,** (1997), p. 2.

[49] V.M. Nair, R. Jose, G.M. Anil Kumar, M.M. Yusoff, P.R.S. Wariar, Nanocrystals of a new complex perovskite dielectric Ba_2TmSbO_6, Journal of Alloys and Compounds, **512,** (2012), p. 207.

Chapter 6.

Crystal structure and magnetic studies on pentavalent uranium double perovskite compounds.

6.1 Introduction

The solid state chemistry of the uranium oxide has been of great importance because globally uranium oxide is used as nuclear fuel in nuclear power industries [1]. Prior to its application as nuclear fuel, uranium oxide was used as colorant in glasses and ceramics since ancient times [2]. The solid state properties and the chemical characteristics of uranium oxides are focused on addressing a number of issues in the multiple steps involved in the nuclear fuel cycle, starting from extraction, fuel fabrication, irradiation in nuclear reactor, storage and disposal [1, 3]. Due to multiple oxidation states of uranium viz. $U^{4+/5+/6+}$ with varying ionic radii in different co-ordination makes it possible to form a large variety of complex uranium oxides. Perovskites phases of uranium are significant in the domain related to interaction of uranium oxide fuel with its fission products and clad materials. Barium and strontium are the important alkaline earth fission products and are usually found in the grey phase formed in the irradiated mixed oxide (MOX) fuels. This gray phase is multi-component complex oxides having perovskite structures with chemical composition (Ba, Sr)(U, Pu, Zr, Ln, Mo)O_3 [4, 5]. The property of perovskite structure to accommodate various cations with different valence and ionic-sizes makes it important to study their physical and chemical characteristics for better understanding of the irradiated fuel.

In addition, uranium is an easy choice for studying 5f electron systems due to the problems with availability and high radioactivity in trans-uranium elements. In 5f electron system various interactions like crystal field, spin-orbit coupling and electron-electron repulsion take part and have comparable magnitudes. This adds complexity to analysis and interpretation of the experimental data. It is interesting to study pentavalent uranium compounds as they have simplest 5f electron system i.e., $[Rn]5f^1$. A single electron in the f shell simplifies the theoretical treatment as electron-electron repulsion is excluded. But at the same time synthesizing pure pentavalent uranium compounds are experimentally challenging and thus there is a paucity of such pentavalent uranium compounds.

6.1.1 Perovskites containing pentavalent uranium

Many perovskite phases containing uranium have been reported in the literature. Single perovskite is not possible with hexavalent uranium but they easily form double perovskites with many cations and show good degree of cationic ordering at B-site because of large charge difference between other B-cation [6]. It is difficult to form pure single perovskite with tetravalent uranium. Cordfunke et. al. showed that continuous series of perovskite phases can be formed in $BaUO_3$–$Ba_{1-y}UO_{3-x}$–Ba_3UO_6, where uranium exists in tetravalent state in $BaUO_3$ and subsequently oxidizes to hexavalent state in Ba_3UO_6 [7]. It was also shown that preparation of pure $BaUO_3$ was unsuccessful and contains UO_2 as a secondary phase. Simple pentavalent uranium perovskites of the form AUO_3 (A=Li, Na, K, Rb) has been studied in the past and shown to have uranium in pentavalent oxidation state from magnetic and XPS studies [8-14]. Similar to AUO_3, pentavalent uranium can be expected in a double perovskite compounds ($A_2B'UO_6$), where oxidation states of A and B’ are chosen appropriately for charge neutrality. Such compounds with A=Sr, Ba and B’=trivalent transition or rare earth metals were first reported by A. W. Sleight et al. [15] and S. K. Awasthi et al. [16]. The compounds were characterized using XRD and shown to have distorted cubic structure with rock salt ordering but no detail crystal structure was reported.

Later Von S. Kemmler-Sack studied these compounds and stated that existence of exact stoichiometric Ba_2REUO_6 phase was difficult [17]. The compounds were characterized using X-ray diffraction and a detailed analysis of absorption spectroscopy was reported which was correlated with the $5f^1$ electron system in octahedral crystal field with spin-orbit coupling. Fig. 6.1 shows the splitting of the 5f1 energy level by octahedral crystal field and spin-orbit coupling. Here Γ_7 is the ground state Kramers doublet from where the electron can be excited to the higher energy levels. From the absorption spectroscopy the energy gaps between these levels can be estimated.

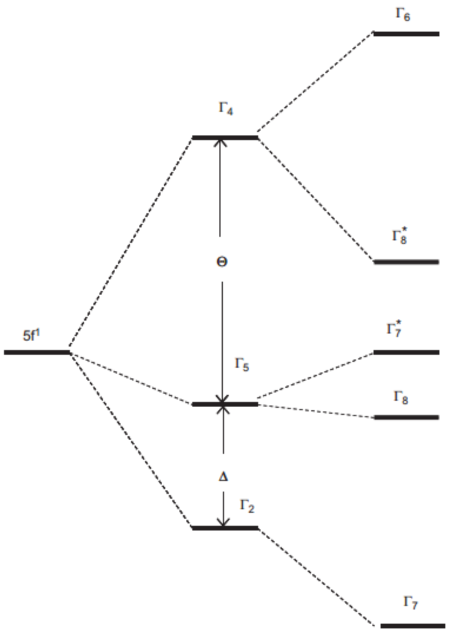

Figure 6.1 *Splitting of $5f^1$ orbital energy levels perturbed by octahedral crystal field and spin-orbit coupling [18].*

6.1.2 Magnetism and EPR studies on pentavalent uranium perovskites

Generally in the case of actinides, 5f orbital are more delocalized in nature as compared to the 4f orbital in the rare earth elements because 5f energies lie in close proximity to 6d and 7s orbital. In addition, the crystal-field interaction has more influence on the spin-orbit coupling interaction than that for the 4f compounds, which results in mixing of higher states with the ground state. This situation adds complexity for analyzing the magnetic properties of actinide compounds. Bickel M. et al. reported magnetic data for various $5f^0$ and $5f^1$ compounds [19], where it has been observed that even in the case of no f-electron ($5f^0$ compounds), it still exhibits temperature independent paramagnetism. It has been explained that this intrinsic property of 5f electron is due to crystal field effect and increased degree of covalency in An-O bonding. In the recent paper using Density Functional Theory (DFT) of MUO_3 (M=Na, K, Rb), it has been shown that U s, d and f orbitals are hybridized with O p orbital and thus indicating covalent bonding nature [20]. Crystal field effect and covalent nature in U-O bond causes temperature independent paramagnetism and lowered magnetic moment than expected according to Hund's rules.

Hexavalent uranium does not contain any unpaired electron and thus is diamagnetic in nature whereas, tetravalent uranium in octahedral environment show temperature independent paramagnetism as studied in $BaUO_{3.023}$ samples [21]. As discussed before, pentavalent uranium has $5f^1$ electron and thus making it simplest $5f^1$ electron system to be studied. All the AUO_3 (A=Li, Na, K, Rb) compounds show magnetic transition below 32K. In all these compounds, U-O-U super-exchange is said to be responsible for the magnetic transition. In general, a common trend in the variation of magnetic transition is observed in actinides compounds having a $5f^{2n+1}$ electron. The magnetic transition is observed when An-O-An is close enough for super-exchange to be effective [19]. In the case of U^{5+}, Y. Hinatsu empirically showed that long range magnetic ordering occurs if U-U distance is less than the critical distance of 4.6Å (see Fig. 6.2) [13]. This is the common feature observed in the 5f electron systems where the magnetic transition is observed when An-O-An is close enough for super-exchange to be effective [19].

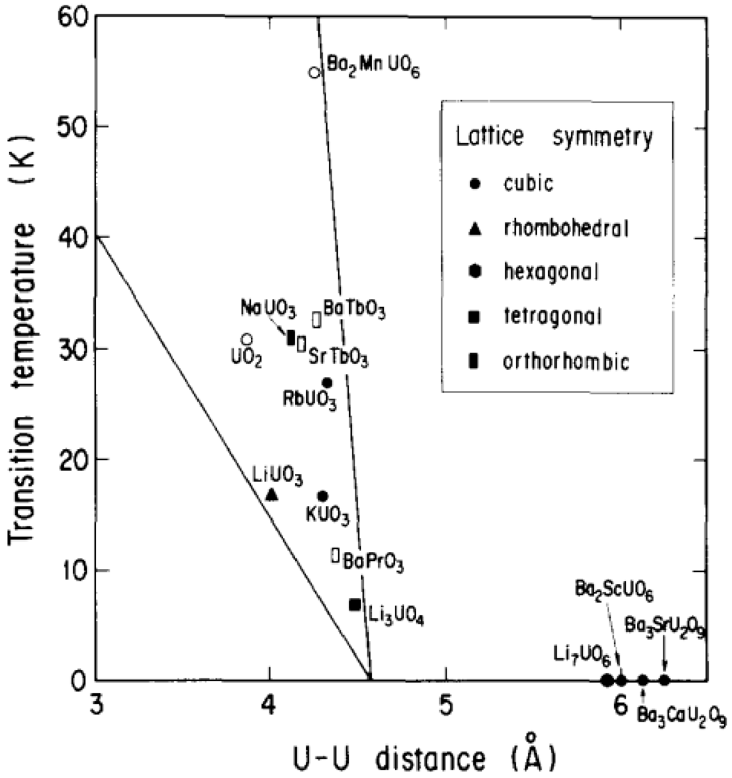

Figure 6.2 *Magnetic transition temperature vs. uranium-uranium bond distance for a number of uranium complex oxides [13].*

EPR studies on $5f^1$ electron compounds are rare. Moreover, there is inconsistency in EPR related literature for these types of compounds with no proper physical explanation. For EPR measurements on actinides, the paramagnetic ions are generally diluted by adding some non-magnetic ions so that the spin-spin and exchange interactions are reduced. Also, EPR measurements are carried out at liquid-helium temperatures for actinide ions in order to increase the spin-lattice relaxation time. But there are also few reports available on the EPR spectra of actinide ions at room temperature which are not magnetically diluted. In the literature, EPR signal for U^{5+} has been observed in the wide range from 0.7 to 4 [22]. However, in these reports, there are two types of examples. There are examples in which uranium has been doped in some non-magnetic matrix to dilute the U-U interaction or cases where U-U distance is large due crystal structure, where the spectra are observed at $g \approx 0.7$

[23-27]. But, in the doped cases, it has not been confirmed that the uranium truly exists in the pentavalent state. Second types of examples are where the U-U interaction is strong due to close proximity. Examples of such kind are observed in AUO_3, alkaline earth urinates, Li_3UO_4, $Ba_3SrU_2O_9$, $Ce_{0.1}U_{0.9}O_3$ where g was found to be greater than 2 [12, 22, 23, 28, 29].

6.2 Issue and plan of work

Previous studies on the pentavalent uranium double perovskite compounds do not report about the crystal structure and characterization of pentavalent oxidation state of uranium. Also as mentioned earlier the EPR results in such compounds are inconsistent. In this work pure phase Ba_2REUO_6 (RE= La, Nd, Sm) compounds have been synthesized and the detailed crystal structure analysis was done using x-ray powder diffraction (XRD), neutron powder diffraction (NPD) and high temperature XRD (HT-XRD) techniques. The local structure around the uranium atom was studied using extended x-ray absorption fine structure (EXAFS). Pentavalent oxidation state of uranium was characterized by various techniques like chemical analysis using modified Davies-Gray method, Bond valence sum (BVS) analysis, X-ray absorption near edge structure (XANES) and Thermogravimetry (TG). Magnetization was studied using temperature dependent magnetic susceptibility measurement. From our crystal structure results it is seen that U-U distance is far greater that critical distance of 4.6Å for existence of any magnetic interaction between uranium atoms. EPR studies for such cases are not reported in the literature and EPR study was carried out. Oxidation behaviour of these compounds was studied using TG and decomposition reaction was identified.

6.3 Synthesis

All the compounds were prepared by solid state reaction. $BaCO_3$ (99.9%), RE_2O_3 (RE=La, Nd, Sm) (99.9%), $UO_{2.00}$ (99.9%) and UO_3 (99.9%) were mixed in stoichiometric ratio as follows,

$2BaCO_3 + ½\ RE_2O_3 + ½\ UO_{2.00} + ½\ UO_3$

Reactants $BaCO_3$ and RE_2O_3 were pre-dried at 573K and 1073K respectively. $UO_{2.00}$ was freshly prepared by heating U_3O_8 in Ar- 8%H_2 atmosphere at 1073K. UO_3 was prepared by decomposing uranyl nitrate at 623K. This reaction mixture was initially heated at 1173K for 20 h and later heated at 1673K for 20 h in high purity Ar atmosphere (oxygen content ~ 6 ppm). Finally, the compounds were heated at 1672K for 45 h in Ar- 8%H_2 atmosphere with several intermittent grinding.

6.4 Results and Discussion

6.4.1 Crystal structure using XRD and NPD

Fig. 6.3a shows the room temperature XRD data for Ba_2REUO_6 compounds. All the compounds are iso-structural and adopt monoclinic structure. The reflection marked by arrow in the Fig 6.3a, indicates the super-lattice reflection arising due to the rock-salt type ordering of RE and U ions. The charge and size difference of between RE^{3+} and U^{5+} is adequate for all the samples to show high cation ordering. The lattice parameters for Ba_2LaUO_6 are a=6.2734(3) Å, b=6.2829(3) Å, c=8.8667(4) Å and β=89.844(4)°. The effective cubic lattice parameter calculated for Ba_2LaUO_6 (See footer of table 6.1 for calculation) is a_{La} = 8.8746 Å which is comparable to the previously reported cubic lattice parameter, a=8.90 Å by S. Kemmler-Sack [17]. A similar comparison for the other two compounds is given in table 1, which shows that our results match with the previously reported values. Fig. 6.3b shows the enlarged section of the XRD pattern for Ba_2LaUO_6 compound. The reflection marked by the '*' corresponds to the miller indices (odd-odd-even h k l) when indexed using cubic lattice parameter with a= 8.8746 Å. Similar observations were also noted in the Nd and Sm compounds. These reflections with a (hkl)=(odd odd even), correspond to M-point reflections and they are unambiguous indication of in-phase tilting of octahedral. These reflections purely arise due to the in-phase tilting of the octahedral i.e. due to particular arrangement of oxygen atoms, they are very weak in XRD but have moderate intensity in neutron diffraction pattern. Fig. 6.4 shows the NPD data for Ba_2LaUO_6, where M-point reflections are shown with '*' and have moderate intensity. Thus space group $P2_1/n$ (Glazer notation $a^+b^-b^-$) was chosen for the refinement of the crystal structure. The XRD patterns were refined using Rietveld method. SPuDS software was used to predict the initial crystal structure models for these compounds [30]. XRD data for these compounds (shown in the Fig. 6.1a) was used for the refinement of lattice parameters. The details of the refined crystal cell parameters are summarized in table 6.1. Fig. 6.3c shows the linear variation of unit cell volume with ionic radii of RE^{3+} ions in octahedral co-ordination and it is in agreement with the typical lanthanide contraction. As all the three compounds are iso-structural, the Ba_2LaUO_6 compound has been chosen as the prototype for this series and its detailed crystal structure analysis has been done using ND and EXAFS along with HT-XRD.

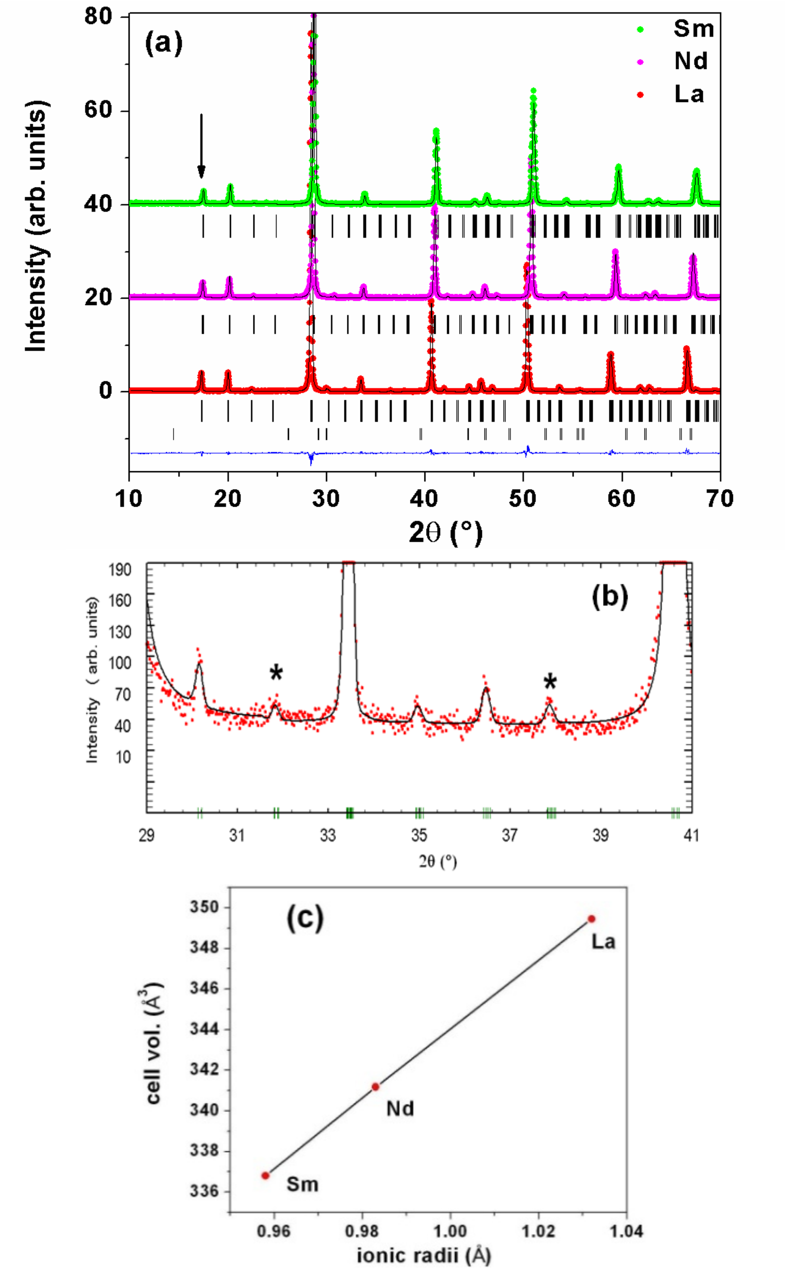

Figure 6.3 *a) X-ray diffraction Rietveld refinement plot for* Ba$_2$REUO$_6$ *(RE= La, Nd, Sm); showing observed, calculated, difference and peak positions markers. For La compound additional secondary phase reflection marker corresponds to* La$_2$O$_3$*.The arrow mark indicates prominent super-lattice reflection due to rock-salt ordering of RE and U ions. b) The weak reflections marked with '*', corresponds to the in-phase tilting (M-point reflection) of octahedra in* Ba$_2$LaUO$_6$*. c) Linear variation of cell volumes vs. ionic radii of* RE^{3+} *ions in octahedral co-ordination.*

Neutron coherent scattering length for La atom (b=8.24 fm) and U atom (b=8.42 fm) are very close and thus neutron diffraction cannot be used in this case for finding anti-site disorder at B site between RE and U. However, as discussed before atomic number difference between La and U is sufficient to find chemical ordering by XRD data alone. Neutron diffraction was used for refining lighter oxygen atoms in the presence of heavier atoms like Ba, U and RE. Fig. 6.4 shows the refined room temperature neutron diffraction data for the La compound. Low temperature neutron diffraction data recorded at 6K show no enhancement in the peak intensity or any additional reflections at lower angles indicating absence of phase transition at low temperature. The 6K NPD data was fitted with the same $P2_1/n$ space group.

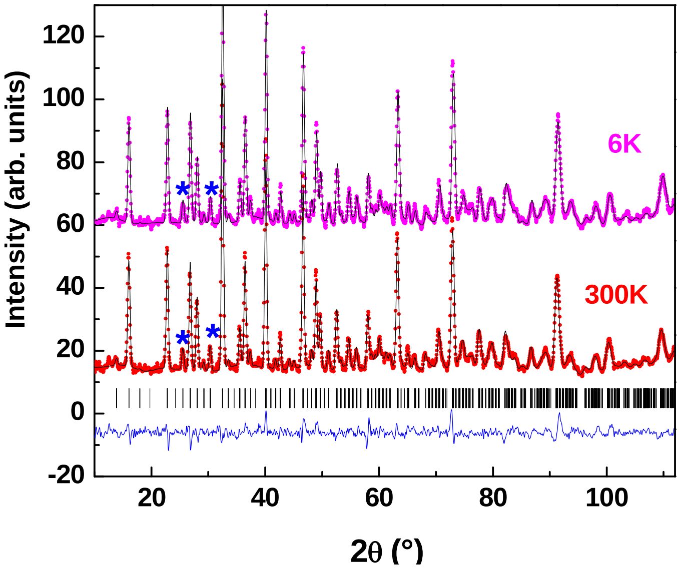

Figure 6.4 *Neutron diffraction Rietveld refinement plot for* Ba_2LaUO_6 *at 300K and 6K; showing observed, calculated, difference and peak positions markers. The reflections marked with '*' corresponds to in-phase tilting of octahedra in* Ba_2LaUO_6*. These reflections are weak in XRD as shown in Fig.6.3b.*

Table 1 and 2 gives the refined crystal structure parameters. Bond lengths for Ba_2LaUO_6 compound are given in table 2. The average <U-O> bond length is 2.175(9) Å for

La compound. Considering ionic radius of O^{2-} ion to be 1.4Å, we get the resultant ionic radius for U^{5+} ion to be 0.775 Å for La compound. This value is close to six co-ordinated U^{5+} ionic radius (r = 0.76Å) as reported by Shannon [31]. Fig. 6.5 shows the crystal structure of Ba_2LaUO_6 compound, showing rock salt ordering of La and U octahedra connected by corners. Ba atom resides in the cavity formed by an octahedral connection.

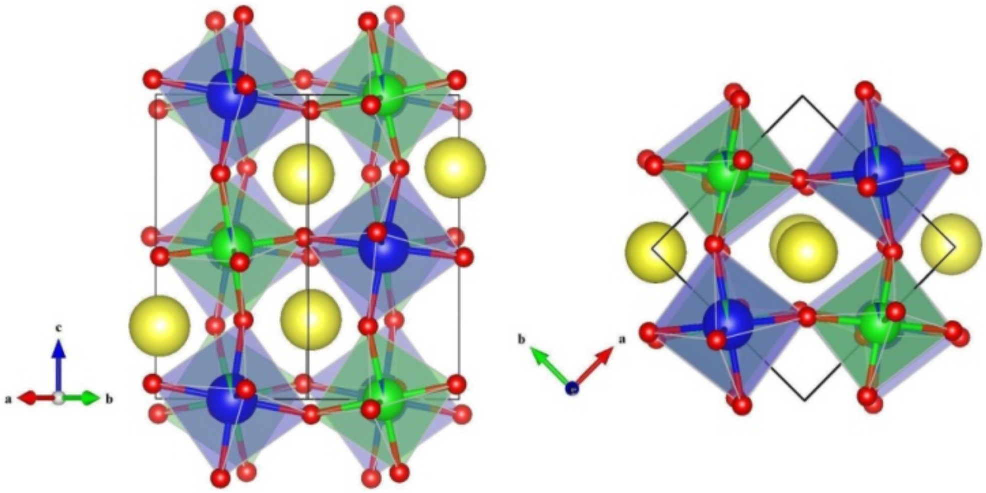

Fig. 6.5 *Crystal structure of Ba_2LaUO_6 showing tilting of La and U octahedra. (Atom colors: Yellow: Ba, Blue: La, Green: U, Red: O).*

Table 6.1 Refined crystallographic data for Ba_2REUO_6 (RE=La, Nd, Sm) compounds.

Compound	**Ba_2LaUO_6**	**Ba_2NdUO_6**	**Ba_2SmUO_6**
Formula Weight (g/mole)	747.59	752.92	759.04
Tolerance factor	0.927	0.937	0.957
System	Monoclinic	Monoclinic	Monoclinic
Space Group	$P2_1/n$ (14)	$P2_1/n$ (14)	$P2_1/n$ (14)
Z	2	2	2
Lattice Parameter	a = 6.2734(3)	a = 6.2263(4)	a = 6.2237(2)
(Å and °)	b = 6.2829(3)	b = 6.2188(4)	b = 6.1963(2)
	c = 8.8667(4)	c = 8.8149(3)	c = 8.7533(3)
	β = 89.844(4)	β = 89.888(4)	β = 89.892(5)
Volume ($Å^3$)	349.48(3)	341.32(4)	337.56(2)
Effective Cubic lattice parameters compared with reported	*a_{La} = 8.8746 Å	*a_{Nd} = 8.8050 Å	*a_{Sm} = 8.7726 Å
	reported values	reported values	reported values
	a=8.90 Å	a=8.82 Å	a=8.79 Å

* Generally, cation ordered monoclinic perovskite phases are indexed using lattice parameters $[\sqrt{2}a_p x \sqrt{2}a_p x 2a_p]$, where a_p is lattice parameter for primitive cubic perovskite. Similarly, cation ordered cubic perovskite phases are indexed with $[2a_p x 2a_p x 2a_p]$. Thus for comparing our monoclinic values with reported cation ordered cubic lattice parameter, we used $2x\text{Vol.}_{\text{monoclinic (present work)}} = \text{Vol.}_{\text{cubic (reported)}} = a_{RE}^3$

Table 6.2 Atomic parameters for Ba_2REUO_6 (RE=La, Nd, Sm) compounds refined using $P2_1/n$ space group.

Atom	Site	x	y	z	Biso(Å^2)	Occupancy
Ba_2LaUO_6						
Ba	4e	0.5004(1)	0.5249(3)	0.2599(4)	0.46(4)	1
La/U	2c	0	1/2	0	0.17(5)	0.978/0.022(1)
U/La	2d	1/2	0	0	0.14(2)	0.978/0.022(1)
O1	4e	0.281(2)	0.264(1)	0.044(1)	0.7(1)	1
O2	4e	0.212(2)	0.803(1)	0.036(1)	1.0(1)	1
O3	4e	0.593(1)	-0.022(1)	0.230(1)	0.9(1)	1

Bond lengths (Å): La-O = 2x2.336(7), 2x2.345(8), 2x2.469(5); U-O = 2x2.188(8), 2x2.213(9), 2x2.124(9); <Ba-O> = 2.99(7)
$^{\#}$For U-O octahedral: Octahedral distortion index=0.015; Bond angle variance=22.2 deg.^{2}
Rp(%)=7.38, Rwp(%)=13.1, Rf(%)=3.61, χ^2=1.10

Atom	Site	x	y	z	Biso(Å^2)	Occupancy
Ba_2NdUO_6						
Ba	4e	0.4892(6)	0.5187(3)	0.252(1)	0.62(4)	1
Nd/U	2c	0	1/2	0	0.18(4)	0.950/0.050(1)
U/Nd	2d	1/2	0	0	0.16(5)	0.950/0.050(1)
O1	4e	0.309(9)	0.284(8)	0.025(7)	0.7	1
O2	4e	0.262(9)	0.754(9)	-0.005(9)	1.0	1
O3	4e	0.620(6)	-0.023(4)	0.250(5)	0.9	1

Bond lengths (Å): Nd-O = 2x2.28(6), 2x2.33(4), 2x2.36(5); U-O = 2x2.13(6), 2x2.14(6), 2x2.33(4); <Ba-O> = 3.02(7)
#For U-O octahedral: Octahedral distortion index=0.04; Bond angle variance=122.2 deg.^{2}
Rp(%)=7.66, Rwp(%)=12.3, Rf(%)=3.99, χ^2=1.3

Atom	Site	x	y	z	Biso(Å^2)	Occupancy
Ba_2SmUO_6						
Ba	4e	0.498(1)	0.515(2)	0.248(6)	0.62(2)	1
Sm/U	2c	0	1/2	0	0.26(3)	0.960/0.040(2)
U/Sm	2d	1/2	0	0	0.12(2)	0.960/0.040(2)
O1	4e	0.280(5)	0.269(6)	0.044(8)	0.7	1
O2	4e	0.254(6)	0.764(6)	0.044(8)	1.0	1
O3	4e	0.576(5)	-0.019(3)	0.243(4)	0.9	1

Bond lengths (Å): Sm-O = 2x2.29(4), 2x2.30(3), 2x2.31(4); U-O = 2x2.15(3), 2x2.18(3), 2x2.19(4); <Ba-O> = 3.03(2)
#For U-O octahedral: Octahedral distortion index=0.007; Bond angle variance=5.8 deg.^{2}
Rp(%)=7.06, Rwp(%)=10.6, Rf(%)=3.76, χ^2=1.46

Note: All the atomic positions and thermal parameters for La compound are refined using both x-ray diffraction and neutron diffraction data. All the atomic positions for Nd and Sm compounds are refined using only x-ray diffraction data.

\# Octahedral distortion index $= \sum_{i=1}^{6}\left[\frac{d_i-\bar{d}}{\bar{d}}\right]^2$, where $\bar{d}$ is average bond distance. Bond angle variance $= \left(\frac{1}{11}\right)\sum_{i=1}^{12}(\varphi_i - \varphi_0)^2$, where φ_i are 12 bond angles and φ_0 = 90° is ideal bond angle of octahedra.

Fig. 6.6a shows the high temperature x-ray diffraction (HT-XRD) of Ba_2LaUO_6 recorded at various temperatures. After recording the XRD at a particular temperature, the sample was quenched to room temperature and XRD was re-recorded (QRT-XRD).

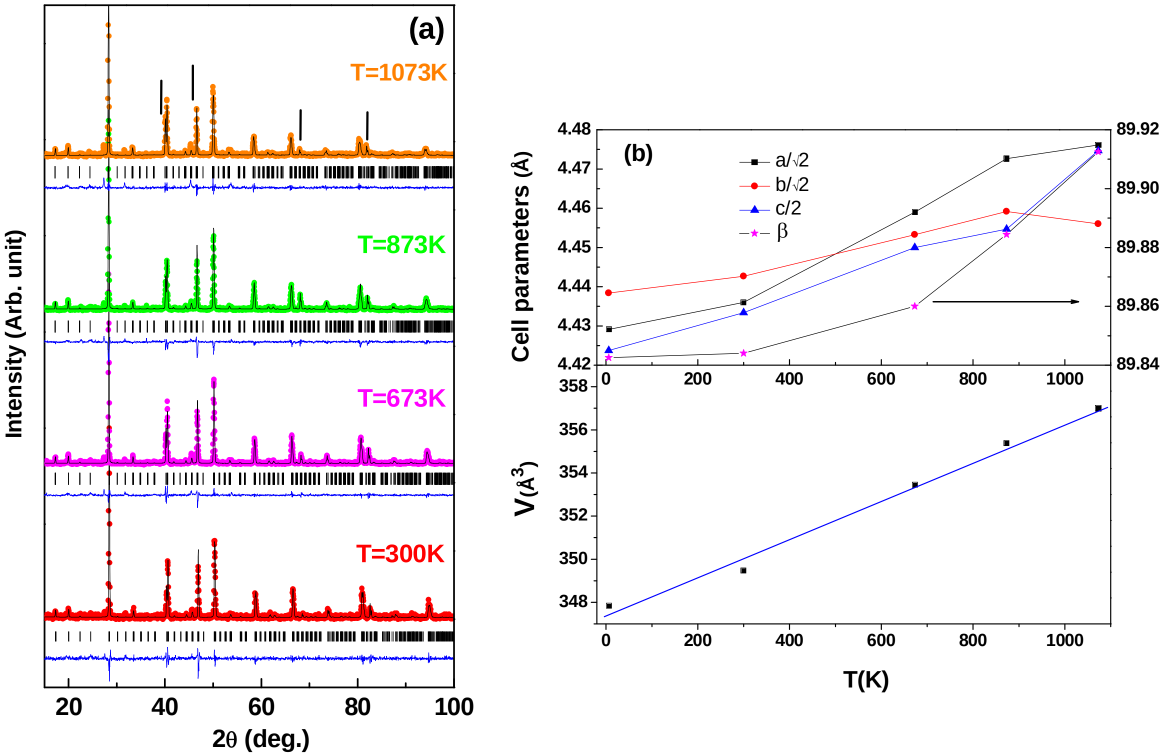

Figure 6.6 *a) High temperature x-ray diffraction Rietveld refined fit shown at various temperatures (The reflections marked with vertical lines on the top, corresponds to Pt-Rh heating stage used for loading sample while recording high temperature XRD) and b) Temperature variation of volume per unit cell for* Ba_2LaUO_6 *where blue line indicates linearity of volume with temperature.*

Comparison of QRT-XRD with as prepared room temperature XRD (RT-XRD) do not show any change in the patterns. From HT-XRD analysis, it is observed that, compound Ba_2LaUO_6 does not undergo any structural phase transition up to 1073K and retain monoclinic structure ($P2_1/n$ space group). The Fig. 6.6b shows the temperature variation of cell parameters. Thus from the 6K NPD and HT-XRD analysis it is observed that Ba_2LaUO_6 retains the monoclinic structure with $P2_1/n$ space-group from 6K to 1073K.

6.4.2 Local structure using EXAFS

The normalized EXAFS spectra at U L_3 edge of Ba_2LaUO_6 sample is shown in Fig. 6.7a. The $\chi(R)$ versus R spectra is obtained for Ba_2LaUO_6 using Fourier transform range of k = 3.0-11.0 $Å^{-1}$ and it is shown in Fig. 6.7b with open circles. The structural parameters (atomic coordination and lattice parameters) of Ba_2LaUO_6 obtained from the refinement of diffraction data were used for simulating the theoretical EXAFS spectra. The bond distances, co-ordination numbers and disorder (Debye-Waller) factors (σ^2), which give the mean square fluctuations in the distances, were used as fitting parameters. The solid line in Fig. 6.7b shows the best simulated fit of $\chi(R)$ versus R and match well with the experimental data.

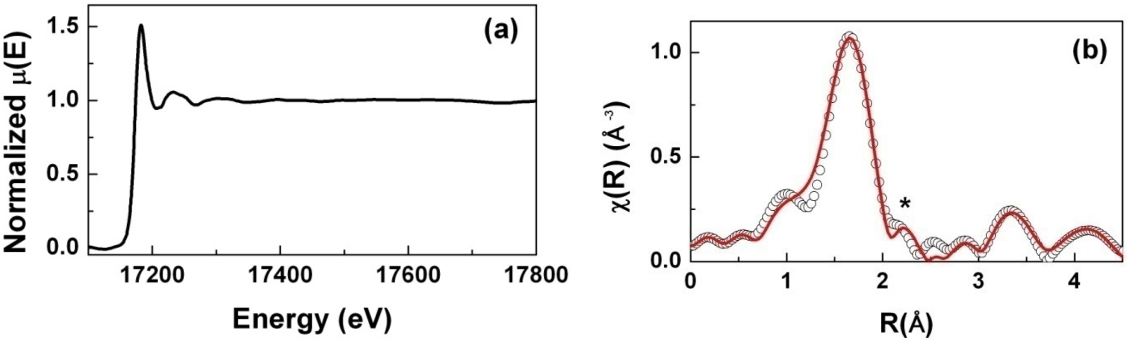

Figure 6.7 *a) Normalised EXAFS spectra of Ba_2LaUO_6 at U L_3-edge. b) Radial distribution function from the k_2-weighted EXAFS spectra of Ba_2LaUO_6 (open circles) and its simulated fit (solid line). Asterisk mark '*' indicates the increase bond distance due to weak anti-site disorder of U ion at La position.*

The best fit results are summarized in table 3. Initially, the theoretical EXAFS spectrum is calculated using a single site for uranium atom. Later scattering path for 3% of anti-site disorder was introduced to fit the shoulder peak (marked as '*' in Fig. 6.7b) of first coordination peak at 2.1 Å. The inclusion of this anti-site disorder for uranium atom improves the goodness of fit. The origin of this small peak is from the anti-site disorder is further confirmed by the fact that the peak gets significantly enhanced in case of an intentionally prepared La-deficient sample $BaLa_{2/3}U^{5+}O_{5.5}$ (spectrum not shown here) where 30% anti-site disorder has been required to obtain a good fit.

Table 6.3 EXAFS fitting results for Ba_2LaUO_6 at U L_3-edge.

Path	R (Å)	Coordination Number	σ^2 (Disorder factor) (Å^2)
U-O (98%)	2.14(1)	6.0(1)	0.0033(5)
U-O (2%)	2.33(3)	6.0(2)	0.0020(5)
U-Ba	3.72(5)	8.0(1)	0.0108(4)
U-La	4.36(8)	6.0(1)	0.0084(5)

The peak positions in χ(R) versus R spectra do not correspond to the real bond distances. Real bond distances are calculated by applying appropriate phase corrections. The first peak in Fourier transform spectra is the contribution of 6 oxygen atoms at a distance of 2.14(1) Å from U. The shoulder peak is the contribution of oxygen from La site with the bond length of 2.33(3) Å. These bond distances are close to the values obtained from diffraction experiments. The next coordination peak is the contribution of 8 Ba atoms at 3.72(5) Å. The third peak is the contribution of 6 lanthanum atoms at 4.36(8) Å as well as other multiple scattering paths. There is no U-U coordination present up to 4.7 Å. The EXAFS analysis shows that the local structure of Ba_2LaUO_6 match well with the bulk structure obtained using the diffraction data.

6.4.3 Confirming the pentavalent oxidation state of uranium using various methods.

First we use the bond length obtained from the crystal structure analysis to calculate the bond valence sum (BVS). The bond valence S_{ij} is defined as $S_{ij} = \exp((R_0-R_{ij})/b)$ and the $BVS=\sum S_{ij}$, where b and R_0 are the constants and depends on the bonding pair under consideration. R_{ij} are the observed bond lengths. The BVS value should match with the oxidation state of atom under consideration. Parameters used for BVS calculation are R_0 = 2.10 Å and b = 0.35, which are more specific to U(V)-O bonds as given in reference [32]. The calculated BVS values from U-O bond in La compound is 4.9 and is close to 5+ oxidation state. Similarly BVS values for other two compounds are given in table 6.4.

The average valence of uranium ion was determined by well-known Davies-Gray chemical titration method [33]. This method does not distinguish between 100%U(V) and 50%U(IV)+50%U(VI) mixture and gives us the average valency of uranium in the compound. Samples were dissolved in concentrated phosphoric acid. In the phosphoric acid medium the U(IV) and U(VI) oxidation states are retained as respective phosphate complex and if U(V) is present, it equally disproportionate to U(IV) and U(VI). Later this solution is titrated with potassium dichromate solution which acts as an oxidizing agent and U(IV) amount in the solution is estimated. For total uranium content, the solution is initially treated with a ferrous solution where all of the uranium is reduced to U(IV). Then the same procedure of titration using potassium dichromate as an oxidizing agent is used to calculate the total uranium content in the solution. Table 6.4 gives the amount of U(IV) and total uranium content in these compounds. These values show that in all compounds average uranium valency is close to 5.

Table 6.4 Uranium analysis results obtained from Davies-Gray titration method and Bond valence sum calculation.

Ba_2REUO_6	Total uranium content obs. (Wt. %)	Total uranium content calc. (Wt %)	U^{4+}/U^{6+} ratio obs.	BVS calculated for Uranium	Colour of the compound
La	31.57(2)%	31.84%	48.17% / 51.83%	4.9	Pale brown ●
Nd	31.32(4)%	31.61%	43.42% / 56.58%	4.7	Tan brown ●
Sm	30.14(1)%	31.36%	45.67% / 54.33%	4.9	Tan brown ●

We further use thermogravimetry (TG) to oxidize the compounds in air up to 1273K in thermobalance. Analysis of TG curve (see section 6.3.5) indicates that, all these compounds show the weight gain in the temperature range 473 to 973K due to the oxidation of uranium. The weight gained during the oxidation step match well with the expected weight gain for U^{5+} to convert to U^{6+}. The TG analysis values and further details regarding the oxidation and decomposition reaction can be seen in section 6.3.5.

The above methods only give the indirect proof of the average oxidation state of uranium in the compounds. Thus we use XANES analysis to confirm the existence of pentavalent uranium in Ba_2LaUO_6 compound. The normalized XANES spectra at U L_3 edge for Ba_2LaUO_6 compound is shown in Fig. 6.8 along with standards UO_2 and UO_3 with oxidation state 4+ and 6+, respectively. The edge position is obtained from the position of maxima of the first derivative of normalized XANES spectra. The edge position along with the white-line positions are given in table 6.5. It can be seen that uranium edge position for Ba_2LaUO_6 lies in between UO_2 and UO_3 which indicates uranium is present in either in 5+ oxidation state or mixture of 4+ and 6+ oxidation states. However, as reported by A. L. Smith et al. and A.V. Soldatov et. al. the weak shoulder denoted by A in Fig. 6.8 indicates the contribution of uranium unoccupied (6d) electronic states of the +5 oxidation state of uranium, indicating that uranium is present in +5 oxidation state in Ba_2LaUO_6 [34, 35].

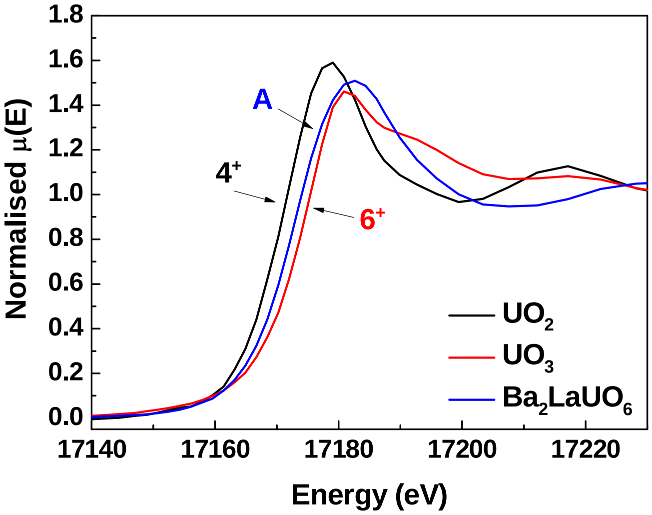

Figure 6.8 *Normalized XANES spectra of* Ba_2LaUO_6 *at U* L_3*-edge.*

Table 6.5 Edge position of U L_3-edge obtained from XANES spectra. Edge position is taken as maximum of first derivative.

Sample	Edge position	White line (eV)
$UO_{2.00}$	17171.5(5)	17179.0(5)
UO_3	17175.4(5)	17180.8(5)
Ba_2LaUO_6	17173.3(5)	17182.4(5)

6.4.4 Magnetization and electron paramagnetic studies

Fig. 6.9**a** shows the temperature dependence of magnetization for the three compounds. The value of the magnetic moment per gram increases from La to Sm to Nd, respectively as expected from the magnetic moments calculated for the RE^{3+} ground state using Hund's rules. None of the compound shows any magnetic transition down to 5K. Inset in Fig. 6.9a shows typical paramagnetic field dependent magnetization for the three compounds. As discussed before NPD data at 6K does not show any change in the intensity of reflections or presence of super-lattice reflections ruling out any long-range magnetic ordering or change in the crystal structure in this compound, on cooling.

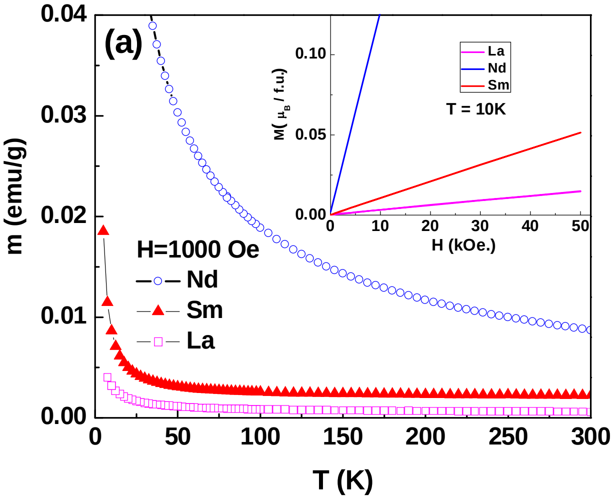

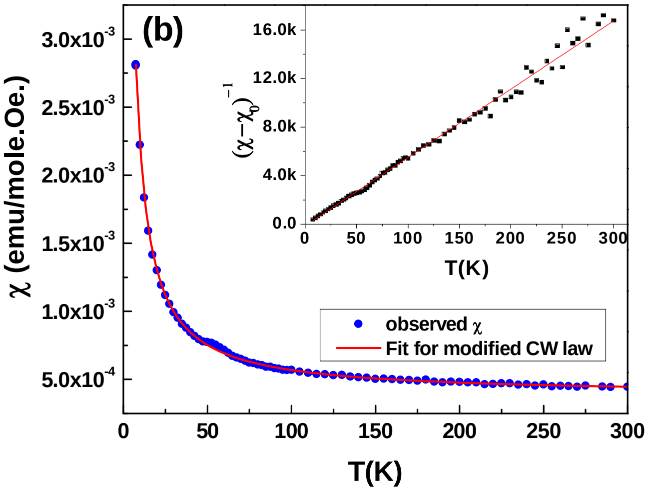

Figure 6.9 *a) Temperature dependence of magnetization for Ba_2REUO_6 (RE= La, Nd, Sm). Inset show field dependence of magnetization at 10K. b) Modified Curie-Weiss law fit for temperature dependence of susceptibility of Ba_2LaUO_6. Inset shows linear fit to $(\chi-\chi_0)^{-1}$ in whole temperature range. Anomaly at 55K is an artifact due to sample holder straw material.*

In all the three compounds the temperature variation of inverse susceptibility (H/M) could not be fit to the Curie-Weiss law even at a higher temperature. The fit results in very high and unphysical moment for these compounds. It has been previously shown in the similar pentavalent uranium compounds that a temperature independent susceptibility term is necessary for fitting the data [13]. So in our study, we have used the modified Curie-Weiss law as given below for fitting the temperature dependence of susceptibility

$$\chi = \chi_0 + \frac{C}{(T - \theta)}$$

where χ_0 is temperature independent susceptibility, C and θ are Curie constant and temperature, respectively. Fig. 6.9b shows the fit of modified Curie-Weiss law for Ba_2LaUO_6 compound in the temperature range of 5K to 300K. The value of the temperature independent parameter for La compound is; χ_0=385x10^{-6} emu/mole.Oe. This value is comparable with previously reported values (within the range 140x10^{-6} - 440x10^{-6} emu/mole.Oe.) having a similar oxidation state of uranium [13, 18, 19]. In La compound only U ion has magnetic contribution; the effective magnetic moment calculated for uranium ion is μ_{eff} = 0.4 μB and is smaller as compared to the previously reported values for pentavalent uranium ion [14]. The Curie-Weiss temperature is close to zero (θ = -0.1K) which show an absence of long range magnetic interaction. For complex uranium oxides, Y. Hinatsu empirically showed that long range magnetic ordering does not occur if U-U distance is more than the critical distance of 4.6Å [13]. In Ba_2LaUO_6 compound, due to rock salt ordering the U-U distance increases to 6.274Å and thus leading to absence of long range magnetic ordering in this compound.

In Sm and Nd compounds the effective magnetic moment is contributed by both uranium and (Sm^{3+}/Nd^{3+}) ion i.e. ($\mu^2_{eff} = \mu^2_{eff\,(U)} + \mu^2_{eff\,(RE)}$). The observed effective magnetic moments for Ba_2NdUO_6 is $\mu_{eff} = 3.6\mu_B$. As all the compounds are iso-structure and they do not have any strong magnetic interaction, we assume the magnetic moment of uranium ion remains same for all the three compounds. Thus the effective magnetic moments calculated for Nd ion is μ_{eff} = 3.58 μ_B. The moment of Nd^{3+} ion matches well with the theoretical value of 3.62 μB for ground state $^4I_{9/2}$ for $4f^3$ electron configuration. It is well known for the Sm^{3+} ion that, observed magnetic moment does not match with the expected magnetic moment corresponding to ground state $^6H_{5/2}$ for $4f^5$ electronic configurations. This discrepancy is because of the small energy difference between the higher energy levels and the ground state [36]. Contributions from the higher states of L-S multiplets is found to explain this discrepancy and approximate formulation for the Sm^{3+} ion is given by Van-Vleck [36]. In Sm compound, there are two non-interacting magnetic ions U^{5+} and Sm^{3+} (Curie-Weiss paramagnetic behaviour of U^{5+} and Van-Vleck paramagnetic behaviour of Sm^{3+}), because of which fitting magnetic susceptibility curve is not possible.

EPR spectra of the compounds were recorded at room temperature. In our measurements, EPR signals were observed in the region with $g \approx 0.73$ and 2.24 when the sample cavity was filled with air (see Fig. 6.10a). While when the cavity was flushed with inert Ar gas, the signal at $g = 0.73$ disappeared. Therefore we believe that the signal of $g = 0.73$ originates from paramagnetic molecular oxygen present in the air [37, 38]. Henceforth, in our present compounds, we will not consider $g = 0.73$ as signal due to the sample. Fig. 6.10b shows the EPR signal for the compounds and it is clearly seen from the graph that there are two distinct signals S1 and S2 corresponding to $g = 2.24$ and 2.31, respectively. As La^{3+} has no unpaired electron it is not EPR active. Though Nd^{3+} and Sm^{3+} have odd electron $4f^3$ and $4f^5$, respectively, it is well reported in the literature that they do not show EPR signal at room temperature because of a very fast spin–lattice relaxation. Generally, rare-earths ions show EPR signal only at lower temperatures [39, 40]. Thus, in the title compounds, U^{5+} ($5f^1$ electron state) is the only EPR active ion.

It is somewhat contradictory in the present case, as discussed above in the introduction $g > 2$ signal is observed in compounds where U-U magnetic interactions are dominant and g ≈ 0.7 signal is observed in diluted U^{5+} samples where U-U interactions are absent. Studies by Y. Hinatsu on such pentavalent uranium compounds shows that g > 2 cannot be explained due to U^{5+} in octahedral crystal field. It is proposed that signal for g > 2 corresponds to the magnetic interaction between U^{5+} ions and observed only when the U-U has close proximity [13, 23]. Interestingly in our compounds, U-U distance is larger than 6 Å, but we still observe EPR signal with g > 2.

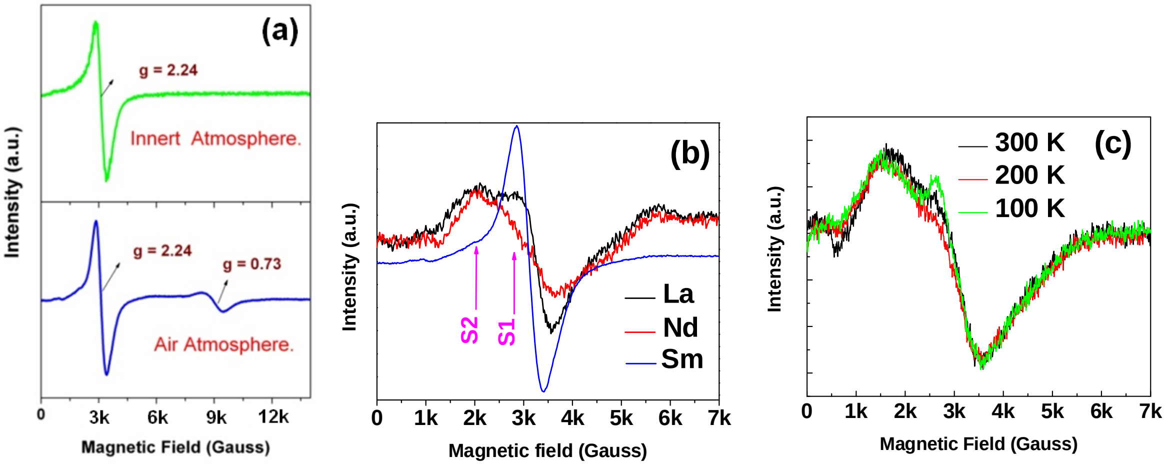

Figure 6.10 *a) EPR spectra of Ba_2SmUO_6 recorded at room temperature. b) EPR spectra for Ba_2REUO_6 (RE= La, Nd, Sm). S1 and S2 signal corresponds to g = 2.24 and 2.31, respectively. c) EPR spectra of Ba_2NdUO_6 measured at different temperature.*

For La and Nd compound both the signals at g = 2.24 and 2.31 are broad and of equal strength, whereas in Sm compound the signal for g = 2.31 is almost absent and signal for g = 2.24 is sharp and intense. As a typical example for showing split in the EPR spectra, Nd sample was chosen for the low temperature EPR measurements. The measurements show that there is no appreciable change in the signal intensity, line width and magnetic field of the two signals when the sample is cooled to 100K (see Fig. 6.10c). This confirms that the compound remains paramagnetic on cooling down to 100K and thus shows absence of any effect due to exchange interaction. Ideally, if the uranium octahedra were perfect then by its symmetry two components of g i:e g$\|$ and g$\perp$ should have been equal in magnitude. But as the octahedral distorts, g$\|$ and g$\perp$ will differ and will give convoluted signal for powder samples. It is interesting to observe that our measurements show the similar type of co-relation between EPR spectra and distortion of U^{5+} octahedral. Here we propose for the first time that the split in the EPR spectra at $g \approx 2.3$ for pentavalent double perovskites Ba_2REUO_6 compounds can be correlated to octahedral distortion around uranium ion. The distortion parameters calculated for UO6 octahedra in given in the table 6.6. It is observed that distortion parameters are comparatively larger for La and Nd compounds than for Sm compound. For Sm compound, it is expected that the distortion should be relaxed due to a decrease in the octahedral bond length at B site and thus increasing the tolerance factor. Thus reduction of signal S2 is EPR spectra of Sm compound is due to decrease in the U-O octahedral distortion. More such studies on similar compounds with pentavalent uranium in octahedral environment are needed to establish this fact.

Table 6.6 Octahedral distortion parameters for Ba_2REUO_6.

UO_6 octahedra	**La**	**Nd**	**Sm**
Octahedral distortion index	0.015	0.03	0.004
angle variance	22.2 $deg.^2$	117.4 $deg.^2$	13.6 $deg.^2$

6.4.5 Thermogravimetry and oxidation behavior

As mentioned in the section 6.4.3, thermogravimetry was used for inferring the oxidation state of the uranium. It was also used for studying oxidation behaviour of the compounds and to explore the possibility of formation of any new mixed valence compound during oxidation.

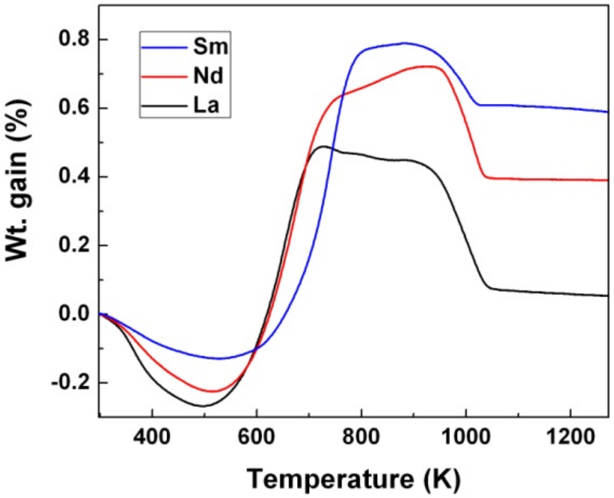

Figure 6.11 *Thermogram showing percent weight gain for oxidation of* Ba_2REUO_6 *(RE= La, Nd, Sm) in dry air.*

The oxidation behaviour of Ba_2REUO_6 (RE = La, Nd, and Sm) was studied by heating the sample up to 1273K in thermobalance. Fig. 6.11 shows TG curve as a function of temperature in dry air. Analysis of TG curve indicates that all these compounds show a weight loss of 0.13 to 0.27% in the temperature range 323 to 473K. This corresponds to the loss of loose moisture which the samples have picked up during storage at room temperature. Fig. 6.11 also shows that samples were oxidized in the temperature range 473 to 973K. Interestingly in all the three compounds, the weight loss occurs above 973K and finally stabilizes up to 1273K. The weight loss above 973K indicates that the hexavalent uranates formed are not stable at high temperature. Table 6.7 gives thermogravimetric data obtained during oxidation of Ba_2REUO_6 and 1273K oxidized products identified by XRD. It can be seen from the table that the difference between observed and expected weight gain could be due to the moisture pick up of the samples at room temperature. The reduced phases Ba_2REUO_6, synthesized by hydrogen reduction, are highly reactive compounds and they pick up moisture/oxygen during storage. It has been reported in the literature that alkaline earth uranates, AUO_{4-x} and $A_2U_3O_9$ (A= Ba, Sr, Ca), which were formed by hydrogen reduction of corresponding hexavalent uranates gradually took up oxygen into their lattice even at room temperature when exposed to air [41, 42].

Table 6.7 Thermogravimetric results and phases present in the oxidized end products identified using XRD.

Ba_2REUO_6	Expected Wt. gain (%)	Maximum Wt. gain (%)	End products identified by XRD	Colour of the end product
La	1.07%	0.76%	$Ba_2La_{1-x}U_{1-y}O_{6-z}$ + $(La,U)O_{2\pm\delta}$ + minor un-identified phase	Dark Orange 🟠
Nd	1.06%	0.95%	$Ba_2Nd_{1-x}U_{1-y}O_{6-z}$ + $(Nd,U)O_{2\pm\delta}$	Orange 🟠
Sm	1.05%	0.92%	$Ba_2Sm_{1-x}UO_{6-z}$ + $(Sm,U)O_{2\pm\delta}$	Yellowish orange 🟠

XRD and Davis-Gray chemical titration method (for finding out O/U and hence oxygen stoichiometry in the compound) was carried out on 1273K oxidised products obtained in thermogravimetric experiments. XRD data show final heated products contains main phase having peaks similar to that of parent phase with shifts in the line positions and additional phases which are given in table 6.7. Though there is weight loss after 973K, chemical titration of the final product gave 100% U(VI) in all the three compounds. This is possible only if re-oxidation of the final product (1273K heated) occur during cooling the samples in air. Similar behaviour was observed for the $(RE,U)O_{2\pm x}$ phases [43]. It has also been observed that uranium oxides doped with high concentration of lanthanides forms defect fluorite $(RE,U)O_{2-x}$ phases which are highly unstable on exposure to air and pick up oxygen, thereby oxidizing uranium to U^{6+} state [44, 45]. Thus, weight loss at higher temperature and phases identified in the oxidized products suggests that when U(V) oxidizes to U(VI), a part of the RE_2O_3 is expelled out along with or without uranium to form $(RE,U)O_{2\pm x}$ as secondary phases, respectively. The formation of $(RE,U)O_{2\pm x}$ phases depends upon the individual solid solubility limits. The general oxidation reaction may be given as

$Ba_2REUO_6 \rightarrow Ba_2RE_{1-x}U_{1-y}O_{6-z} + (RE_x,U_y)O_{2\pm\delta}$

6.5 Conclusions

Double perovskites compounds Ba_2REUO6 (RE=La, Nd, Sm) were prepared by solid state method and their crystal structure analysis was done using XRD, NPD and EXAFS. All the compounds show monoclinic structure with $P2_1/n$ space-group. The HT-XRD and NPD shows that crystal structure for La a compound retains monoclinic structure with $P2_1/n$ from 6K to 1073K. The oxidation state of uranium was probed by various techniques like Davis-Gray titration, BVS, TG and XANES which confirmed the pentavalent oxidation state of uranium in these compounds. The magnetic susceptibility measurement gives very weak moment of 0.4 μB per uranium ion. Here, for the first time we report the EPR results for pentavalent double perovskite compounds. In these compounds we do not observe EPR signal at $g\approx0.75$ which is commonly reported in the other pentavalent uranium oxides. We observe the EPR signal at $g>2$ and the split in the EPR signal could be correlated to the octahedral distortion around the uranium ion.

6.6 References

[1] I. Crossland, Nuclear Fuel Cycle Science and Engineering, Elsevier Science (2012).
[2] D. Strahan, Uranium in glass, glazes and enamels: history, identification and handling, Studies in Conservation, **46,** (2001), p. 181.
[3] A. Abdelouas, Uranium Mill Tailings: Geochemistry, Mineralogy, and Environmental Impact, Elements, **2,** (2007), p. 335.
[4] M.W.D. Cooper, S.C. Middleburgh, R.W. Grimes, Swelling due to the partition of soluble fission products between the grey phase and uranium dioxide, Progress in Nuclear Energy, **72,** (2014), p. 33.

[5] R.P.C. Schram, R.J.M. Konings, Chemical form of fission products in high burnup fuels, International Atomic Energy Agency (IAEA), **1998**, pp. 245.

[6] S. Vasala, M. Karppinen, $A_2B'B''O_6$ perovskites: A review, Progress in Solid State Chemistry, **43,** (2015), p. 1.

[7] E.H.P. Cordfunke, A.S. Booij, V. Smit-Groen, P. van Vlaanderen, D.J.W. Ijdo, Structural and Thermodynamic Characterization of the Perovskite-Related $Ba_{1+y}UO_{3+x}$ and $(Ba, Sr)_{1+y}UO_{3+x}$ Phases, Journal of Solid State Chemistry, **131,** (1997), p. 341.

[8] Y. Hinatsu, T. Fujino, N. Edelstein, Magnetic susceptibility of $LiUO_3$, Journal of Solid State Chemistry, **99,** (1992), p. 182.

[9] S. Kemmler-Sack, E. Stumpp, W. Rüdorff, H. Erfurth, Ternäre Oxide. IX. Magnetismus des U(V)-Ions in ternären Oxiden, Zeitschrift für anorganische und allgemeine Chemie, **354,** (1967), p. 287.

[10] S.F. Bartram, R.E. Fryxell, Preparation and crystal structure of $NaUO_3$ and $Na_{11}U_5O_{16}$, Journal of Inorganic and Nuclear Chemistry, **32,** (1970), p. 3701.

[11] A.B. Van Egmond, E.H.P. Cordfunke, Investigations on potassium and rubidium uranates, Journal of Inorganic and Nuclear Chemistry, **38,** (1976), p. 2245.

[12] C. Miyake, K. Fuji, S. Imoto, Electron spin resonance spectra and magnetic susceptibilities of mixed oxides, MUO_3 (M; Li, Na, K, and Rb), of pentavalent uranium, Chemical Physics Letters, **61,** (1979), p. 124.

[13] Y. Hinatsu, Magnetic studies on alkali metal uranates(V) MUO_3 with the perovskite structure, Journal of Alloys and Compounds, **203,** (1994), p. 251.

[14] S. Van den Berghe, A. Leenaers, C. Ritter, Antiferromagnetism in MUO_3 (M=Na,K,Rb) studied by neutron diffraction, Journal of Solid State Chemistry, **177,** (2004), p. 2231.

[15] A.W. Sleight, R. Ward, Compounds of Hexavalent and Pentavalent Uranium with the Ordered Perovskite Structure, Inorganic Chemistry, **1,** (1962), p. 790.

[16] S.K. Awasthi, D.M. Chackraburtty, V.K. Tondon, Tetravalent, pentavalent and hexavalent uranium compounds of the type $A_2BB'O_6$, Journal of Inorganic and Nuclear Chemistry, **29,** (1967), p. 1225.

[17] S. Kemmler-Sack, Über Perowskitphasen in den Systemen $AO–SE_2O_3–UO_{2,x}$ mit A = Erdalkali und SE = Seltene Erden. La sowie Y. V. Über den Existenzbereich der Perowskitphasen $A_2SEU^VO_6$, Zeitschrift für anorganische und allgemeine Chemie, **402,** (1973), p. 255.

[18] A. Nakamura, Y. Doi, Y. Hinatsu, Magnetic properties of barium uranate $Ba_2U_2O_7$, Journal of Solid State Chemistry, **184,** (2011), p. 531.

[19] M. Bickel, B. Kanellakopulos, Systematics in the Magnetic Properties of Ternary Actinoid Oxides, Journal of Solid State Chemistry, **107,** (1993), p. 273.

[20] S. Azam, A.H. Reshak, Theoretical calculations for MUO_3 (M = Na; K; Rb): DFT + U study, Journal of Organometallic Chemistry, **766,** (2014), p. 22.

[21] Y. Hinatsu, The Magnetic Susceptibility and Structure of $BaUO_3$, Journal of Solid State Chemistry, **102,** (1993), p. 566.

[22] G.C. Allen, A.J. Griffiths, C.W. Suckling, Electron spin resonance spectra of mixed oxides containing uranium and alkaline earth metals, Chemical Physics Letters, **53,** (1978), p. 309.

[23] C. Miyake, H. Takeuchi, H. Ohya-Nishiguchi, S. Imoto, Electron Spin Resonance and Magnetic Susceptibility of M-U-O Ternary Mixed Oxides. I. Anomalies of Electron Spin Resonance and Magnetic Susceptibility of $Li_{2n-5}UO_n$ (n = 3, 4, and 6), physica status solidi (a), **74,** (1982), p. 173.

[24] M.M. Abraham, L.A. Boatner, D.N. Olson, U.T. Höchli, EPR studies of some f^n and d^n electronic impurities in $KTaO_3$ single crystals, The Journal of Chemical Physics, **81,** (1984), p. 2528.

[25] W.B. Lewis, H.G. Hecht, M.P. Eastman, Electron paramagnetic resonance and optical studies of pentavalent uranium, Inorganic Chemistry, **12,** (1973), p. 1634.

[26] J. Selbin, H.J. Sherrill, Spectral studies of oxouranium(V) species, Inorganic Chemistry, **13,** (1974), p. 1235.

[27] Q.B. Nguyen, C.-L. Chen, Y.-W. Chiang, K.-H. Lii, $Cs_3UGe_7O_{18}$: A Pentavalent Uranium Germanate Containing Four- and Six-Coordinate Germanium, Inorganic Chemistry, **51,** (2012), p. 3879.

[28] Y. Hinatsu, Magnetic Properties of Ordered Perovskites $Ba_3CaU_2O_9$ and $Ba_3SrU_2O_9$, Journal of Solid State Chemistry, **108,** (1994), p. 356.

[29] Y. Hinatsu, T. Fujino, Study of electron paramagnetic resonance on $Ce_{0.1}U_{0.9}O_2$ solid solution, Chemical Physics Letters, **172,** (1990), p. 131.

[30] M.W. Lufaso, P.M. Woodward, Prediction of the crystal structures of perovskites using the software program SPuDS, Acta Crystallographica Section B, **57,** (2001), p. 725.

[31] R. Shannon, Revised effective ionic radii and systematic studies of interatomic distances in halides and chalcogenides, Acta Crystallographica Section A, **32,** (1976), p. 751.

[32] W.H. Zachariasen, Bond lengths in oxygen and halogen compounds of d and f elements, Journal of the Less Common Metals, **62,** (1978), p. 1.

[33] W. Davies, W. Gray, A rapid and specific titrimetric method for the precise determination of uranium using iron(II) sulphate as reductant, Talanta, **11,** (1964), p. 1203.

[34] A.L. Smith, P.E. Raison, L. Martel, T. Charpentier, I. Farnan, D. Prieur, C. Hennig, A.C. Scheinost, R.J.M. Konings, A.K. Cheetham, A 23Na Magic Angle Spinning Nuclear Magnetic Resonance, XANES, and High-Temperature X-ray Diffraction Study of $NaUO_3$, Na_4UO_5, and $Na_2U_2O_7$, Inorganic Chemistry, **53,** (2014), p. 375.

[35] A.V. Soldatov, D. Lamoen, M.J. Konstantinović, S. Van den Berghe, A.C. Scheinost, M. Verwerft, Local structure and oxidation state of uranium in some ternary oxides: X-ray absorption analysis, Journal of Solid State Chemistry, **180,** (2007), p. 54.

[36] J.H.V. Vleck, Theory of Electric and Magnetic Susceptibilities, Oxford University Press, London, (1931).

[37] H. Kon, Parmagnetic resonance of molecular oxygen in condensed phases, Journal of the American Chemical Society, **95,** (1973), p. 1045.

[38] R. Simoneau, J.S.M. Harvey, G.M. Graham, EPR of O_2 Impurity in Solid N_2, CO, Ar, and CD4 Prepared from the Vapor, The Journal of Chemical Physics, **54,** (1971), p. 4819.

[39] M.C.R. Symons, Electron Spin Resonance, Royal Society of Chemistry (1993).

[40] S. Cotton, Lanthanide and Actinide Chemistry, Wiley (2013).

[41] T. Yamashita, Study on the solid state chemistry of ternary uranium oxides, **March 1988**.

[42] S.K. Sali, S. Sampath, V. Venugopal, Thermal studies on alkaline earth uranates, Journal of Nuclear Materials, **277,** (2000), p. 106.

[43] H. Tagawa, T. Fujino, K. Ouchi, K. Watanabe, K. Saita, T. Morimoto, Oxidation-Reduction Properties of Mixed Oxides in Lanthanum-Uranium-Oxygen System, Journal of Nuclear Science and Technology, **20,** (1983), p. 467.

[44] Z. Talip, T. Wiss, P.E. Raison, J. Paillier, D. Manara, J. Somers, R.J.M. Konings, Raman and X-ray Studies of Uranium–Lanthanum-Mixed Oxides Before and After Air Oxidation, Journal of the American Ceramic Society, **98,** (2015), p. 2278.

[45] M. Keskar, S.K. Gupta, R. Phatak, S. Kannan, V. Natarajan, Optical properties of Eu^{3+} activated thorium molybdate and thorium tungstate: Structure, local symmetry and photophysical properties, Journal of Photochemistry and Photobiology A: Chemistry, **311,** (2015), p. 59.

Chapter 7.

Summary and future work

The present thesis mainly deals with the crystal structure analysis and its physical property measurements of new complex double perovskite (DP) oxide systems. On a general note, the effect of disorder, ionic size on crystal structure, magnetic and photoluminescence properties has been investigated.

The polycrystalline samples were prepared by solid state synthesis methods or gel combustion method. Crystal structure analysis was done using x-ray diffraction (XRD) and/or powder neutron diffraction (NPD) data. Rietveld refinement was used for crystal structure refinement. Extended x-ray absorption fine structure (EXAFS) and photoluminescence on Eu^{3+} ion doped samples were used as local structural probes. Dc/ac magnetization, neutron depolarization, resistivity, dielectric were used for studying electronic and magnetic properties of the compounds. X-ray absorption near edge structure (XANES) and Thermogravimetry (TG) were used for investigating oxidation state and oxidation behaviour of pentavalent uranium compounds.

The concise summary of each DP oxide systems studied is this thesis is given below:

Chapter 3: Three intermediate compounds in the series $Sr_2Co_{2-x}Ru_xO_6$ were studied. The compounds are disordered i.e. Co and Ru are randomly distributed over B-site. All the intermediate compounds exhibit spin glass nature with T_{SG}≈95K irrespective of Co/Ru ratio, in contrast to the end members $SrCoO_3$ and $SrRuO_3$ which show ferromagnetic ordering. The dominance of spin glass behaviour in the series $Sr_2Co_{2-x}Ru_xO_6$ is attributed to the random distribution of Co and Ru which creates competing nearest-neighbour (NN) and next-nearest-neighbour (NNN) magnetic interactions. Compound with 1:1 Co/Ru ratio; Sr_2CoRuO_6 exhibits semiconductor type resistivity with Mott-type variable range hopping model, which again is the outcome of the disorder. This compound also shows the relaxor type dielectric property at spin glass transition temperature, $T_{SG}\approx 95K$. The anomaly in the bond lengths at spin glass transition temperature indicates a correlation of spin glass and relaxor property and it needs further investigation using temperature dependent local structure probe like EXAFS which is the further scope of this work. In few cases of $AA'BB'O_6$ double perovskites, it has been observed that the appreciable difference in ionic size between A and A' creates strain in the lattice which induces B-cation ordering. This fact can be tested to design new compounds like $ALaCoRuO_6$ and $ALaFeRuO_6$ (A=Na, K) and check whether ordering between Co and Ru can be induced.

Chapter 4: New compounds of the type $BaLaBB'O_6$ where B'= Nb, Sb, Te and B = alkali metal or alkaline earth metals were investigated in this work. All the compounds in these series show rock-salt type B-cation ordering due to large ionic charge and relatively small size of B'-cations (Nb^{5+}, Sb^{5+}, Te^{6+}). The small difference in the ionic size and charge at A-site is not favorable for ordering at A-site and thus above studied compounds do not show any hints of A-cation ordering. The ionic size of the alkali metal or alkaline earth metals changes the crystal structure of these compounds. The crystal structure changes from cubic/rhombohedral to monoclinic as the size of the alkali metal or alkaline earth metal increases. In addition, for smaller size alkali metals or alkaline earth metals, La occupies A-site, while the position of the La changes to B-site for bigger size alkali metals or alkaline earth metals. As the position of the La atom can be controlled using different size of alkali metals or alkaline earth metals, thus this effect can be used for tuning color in rare earth based luminescence materials. Many other compounds with transition metal cations having d^0

electron which can undergo second-order Jahn-Teller distortion like Ti^{4+},Nb^{5+}, Ta^{5+}, Mo^{6+},W^{6+} can be explored which can show simultaneous A-cation ordering. Apart from basic crystal structure understanding these compounds can be studied for their photoluminescence and dielectric properties.

Chapter 5: La cation deficient compound derived from the Ba_2LaMO_6 having the chemical stoichiometry as $Ba_2La_{2/3}M^{5+}O_{5.5}$ (M =Nb, Sb, Bi, and U) were synthesized. The compounds form pure phase and have perovskite type structure similar to Ba_2LaMO_6 compounds. Positron annihilation lifetime spectroscopy shows no evidence of any cation vacancies indicating that $Ba_2La_{2/3}M^{5+}O_{5.5}$ compounds does not form non-stoichiometric compounds but have the normalized formula of $Ba_{2.182}La_{0.727}M_{1.091}O_6$ i.e. $[Ba_2(La_{0.727}Ba_{0.182}M_{0.091})(M)O_6]$ where, La deficiency is filled by 0.18 Ba and 0.09 M cations. This is one of the peculiar examples where the structure is stabilized and prefers to accommodate larger size Ba ion in the octahedral site rather than to form cation/anion vacancies. The occupation of larger Ba ion distorts the octahedral and this is evident from photoluminescence study on Eu^{3+} doped samples and IR-spectroscopic results. The thermogravimetric and XRD analysis of oxidized end product of $Ba_2La_{2/3}UO_{5.5}$ shows no existence of formation of $Ba_2La_{2/3}UO_6$ compound which was proposed earlier by Kemmler-Sack et.al, instead, the compound decomposes which supports our crystal structure model with the formula $[Ba_2(La_{0.727}Ba_{0.182}M_{0.091})(M)O_6]$. Similar to the above studied series of compounds, future work related to the crystal structure of other series of cation deficient DP having formulae $A_2B_{3/4}\square_{1/4}B'O_{6-\delta}$, $A_2B_{4/5}\square_{1/5}B'O_{6-\delta}$, $A_2B_{5/6}\square_{1/6}B'O_{6-\delta}$, $A_2B_{7/8}\square_{1/8}B'O_{6-\delta}$ etc. are of interest. Additionally, the simultaneous presence of cation and anion vacancies can be explored in such compounds by appropriately choosing the A, B and B’ cations.

Chapter 6: Pentavalent uranium complex DP oxides with the formula Ba_2REUO_6 (RE=La, Nd, Sm) were studied in this work. All the compounds exhibit monoclinic crystal structure with high ordering between U^{5+} and RE^{3+}. Uranium is present in the 5+ oxidation state and it was confirmed with various methods like XANES, chemical analysis, and thermogravimetry. U^{5+} shows very weak magnetic moment of 0.4 μ_B. None of the compound show long range magnetic ordering down to 5K in contrast to single AUO_3 perovskite. This is attributed to the absence of any direct magnetic interaction between the two uranium ions due to the complete rock salt ordering between RE and U. Here we report for the first time the EPR spectra for pentavalent DP and show the absence of the signal at $g\approx0.7$ which is commonly reported for pentavalent uranium in solid state compounds. In addition, these compounds show EPR signals in the range $g\approx2.2$ to 2.4 irrespective of U-U distance being larger than 6 Å. This result is in contrast to earlier literature, where it is proposed that EPR signals at $g>2$ correspond to U-U magnetic interaction. For the first time, we have shown that the split in the EPR signals is correlated to the octahedral distortion around the U^{5+} ion. In future other pentavalent DP compounds will be explored and studied for their magnetic. Similar to our recent findings related to EPR and magnetic measurements in pentavalent uranium in DP oxides, it is of interest to investigate other crystal structures like higher order perovskites, compounds having one dimensional octahedral chains, octahedral dimmers etc. In addition to explaining the origin of EPR signal at $g>2$ for $5f^1$ electron configuration, the validity of EPR signals at $g\approx0.7$ shall be thoroughly investigated.